Clock Synchronization with Single Photons

Universitätsdissertation
zur Erlangung des akademischen Grades

doctor rerum naturalium
(Dr. rer. nat.)

vorgelegt dem Rat der

Physikalisch-Astronomischen Fakultät der

Friedrich-Schiller-Universität Jena von

Christopher Spiess, M. Sc.
geboren am 4. April 1995 in Eisenhüttenstadt

Reviewers

Prof. Dr. Andreas Tünnermann
Fraunhofer Institute for Applied Optics and Precision Engineering
IOF, Friedrich Schiller University Jena

Prof. Dr. Martin Gärttner
Friedrich Schiller University Jena

Prof. Dr. Christoph Becher
Saarland University

Abstract

The synchronization of clocks is a key element in 5G technology, industrial automation, smart power grids and classical communication. Quantum communication is the secure counterpart to classical communication and allows for a secure transfer of data based on laws of physics, yet at the cost of an increasing demand for precise timing of events. This demand is served by using ultra-stable references or additional synchronization lasers in systems for quantum communication, which increases the resource overhead significantly. Alternatively, single photons that are already used in the communication network have also been proven to act reliably as timing carriers without any need for external timing references. Previous work focused on actively encoding patterns in the optical signal of the sender in terms of, e.g., the arrival time or polarization. Subsequently, these patterns are recognized as synchronization strings in the receiver. In contrast, this work develops a generalized post-processing protocol without any need of adding synchronization strings to the sender. The protocol naturally integrates into existing quantum communication scenarios without changes to the optical signal and concentrates on (but is not limited to) live operation. The live operation is often not the case, e.g., in a satellite-based quantum key distribution. Additionally, this work provides an in-depth performance analysis of the protocol, compares it with existing clock synchronization methods, describes limitations, and provides an outlook for further applications such as the active phase stabilization of interferometers. I show high-performance clock synchronization with synchronization timing jitters down to 3 ps (root mean squared), employing only commercially widely available, standard, and simple crystal oscillators. The timing stability is as low as 19 ps at an averaging time of 1 s. This stability is higher than having free-running atomic clocks and is even better than classical high-precision time transfer, e.g. the White Rabbit protocol, although the developed protocol uses significantly less signal (single-photon level). In addition to the application in the laboratory, the robustness of the protocol is demonstrated in scenarios of a turbulent free space link over 1.7 km and an intercity link over a distance of 70 km. In the latter, I show a timing stability that reaches the femtosecond level after averaging over only 1000 s. Thanks to its generalized nature, which means that it does not include synchronization strings, it applies not only to correlated photon pair sources but also to pulsed single-photon sources, e.g. weak coherent sources. Pulsing the single-photon source allows for particularly fast processing and synchronization in very low signal regimes, such as in long-distance links. The postprocessing approach compensates for substantial instabilities of the clock, applies to any single-photon source, and is robust to fluctuations in the transmission of the communication link. It does not require any modifications of the single-photon source

and can be easily integrated into a wide range of quantum communication networks. Moreover, it could advance the efforts made toward a secure time transfer and is a promising basis for the metrology of moving objects using single photons.

Zusammenfassung

Die Synchronisierung von Uhren ist ein Schlüsselelement der 5G-Technologie, der industriellen Automatisierung, intelligenter Stromnetze und der klassischen Kommunikation. Die Quantenkommunikation ist das sichere Gegenstück zur klassischen Kommunikation und ermöglicht eine sichere Übertragung von Daten auf der Grundlage physikalischer Gesetze, jedoch mit einem zunehmenden Bedarf an einer hohen Zeitauflösung. Dieser Bedarf kann durch ultrastabile Uhren oder zusätzliche Synchronisationslaser in Quantenkommunikationssystemen gedeckt werden, wodurch sich den Ressourcenaufwand erheblich erhöht. Alternativ dazu erweisen sich einzelne Photonen, die bereits in solchen Quantenkommunikationsystemen verwendet werden, als zuverlässige Zeitgeber, ohne dass externe Zeitreferenzen erforderlich sind. Hierzu konzentrierten sich bisherige Arbeiten auf die aktive Kodierung von Mustern im optischen Signal des Senders, z.B. unter Zuhilfenahme der Ankunftszeit oder der Polarisation. Anschließend werden diese Muster beim Empfänger als Synchronisationsnachricht erkannt. Im Gegensatz dazu wird in dieser Arbeit ein allgemeines Protokoll entwickelt, bei dem der Sender keine Synchronisationsnachrichten hinzufügen muss. Das Protokoll lässt sich ohne Änderungen am optischen Signal in bestehende Quantenkommunikationsszenarien integrieren und konzentriert sich auf den Live-Betrieb (ist aber nicht darauf beschränkt). Der Live-Betrieb ist z.B. bei der satellitengestützten Quantenschlüsselverteilung oft nicht der Fall. Darüber hinaus liefert diese Arbeit eine eingehende Leistungsanalyse des Protokolls, vergleicht es mit bestehenden Methoden zur Uhrensynchronisation, beschreibt Einschränkungen und gibt einen Ausblick auf weitere Anwendungen, wie die aktive Phasenstabilisierung von Interferometern. Ich zeige eine hochleistungsfähige Uhrensynchronisation mit einer niedrigen zeitlichen Synchronisationsungenauigkeit von 3 ps (Root Mean Squared) und Zeitstabilität von 19 ps für eine Integrationszeit von 1 s, wobei nur kommerziell breit verfügbare, standardmäßige, einfache Kristalloszillatoren verwendet werden. Dieses Ergebnis ist besser als die Synchronisationsungenauigkeit freilaufender Atomuhren basierend auf Rubidium. Die Performance ist sogar höher als mit klassischen, hochpräzisen Zeittransfer, z.B. dem White Rabbit Protokoll, obwohl deutlich niedrigeres optisches Signal verwendet wird (Einzelphotonenlevel). Zusätzlich zur Anwendung im Labor wird die Robustheit des entwickelten Protokolls in Szenarien einer turbulenten Freistrahlverbindung über 1.7 km und einer optischen Faserstrecke über eine Entfernung von 70 km zwischen Jena und Erfurt demonstriert. Auf dieser Faserstrecke zeige ich eine Zeitstabilität, welche die Grenze der Femtosekunden in einer Integrationszeit von nur 1000 s erreicht. Dank seines vielseitigen Charakters, d.h. ohne hinzugefügte Synchronisationsnachrichten, ist es nicht nur auf korrelierte Photonenpaarquellen, sondern auch auf gepulste Einzelphotonenquellen, z.B. schwache

kohärente Quellen, anwendbar. Das Pulsen der Einzelphotonenquelle ermöglicht eine besonders schnelle Verarbeitung und eine Synchronisation bei sehr schwachen optischen Signal, wie es bei Langstreckenverbindungen typisch ist. Der Nachbearbeitungsansatz kompensiert erhebliche Instabilitäten der Uhren, ist anwendbar unabhängig von der Einzelphotonenquelle und ist robust gegenüber Schwankungen der Signalqualität. Er erfordert keine Änderungen an der Einzelphotonenquelle und kann leicht in ein breites Spektrum von Quantenkommunikationsnetzen integriert werden. Außerdem könnte das Protokoll die Bemühungen um eine sichere Zeitübertragung voranbringen und bildet eine vielversprechende Grundlage für die Objekterkennung und -verfolgung mithilfe von Einzelphotonen.

Acknowledgments

Thank you a lot to everyone who joined me on my journey towards the Dr. rer. nat. degree (the German equivalent of a Ph.D.)!

First, I thank my supervisor Andreas Tünnermann and co-supervisor Fabian Steinlechner for the support and guidance, in particular near the end of my Ph.D. The same thanks goes out to all my reviewers, including Andrej Kržič, Meritxell Cabrejo-Ponce, Karin Burger, Carlos Andres Sevilla Gutierrez, Gregor Sauer and René Sondenheimer for the suggestions to improve the thesis and the constructive criticism!

Second, I want to thank my day-to-day supervisor Fabian Steinlechner who brought me through all the steps towards better writing. This was a bit of a challenge, as my ideas are sometimes wild and transitions might be missing. Although its still not great, my dear reader, I promise that I will do my best. It would be much worse without Fabian. Furthermore, thank you Fabian for all the amazing work in project acquisition and for backing us up!

In addition, I am extremely grateful for the amazing work environment (the colleagues!) in the quantum communication group in the Fraunhofer IOF. Thank you, my friends, for any means of support: for our workouts, the intensive scientific discussions, curious questions, lively lunches or for having your ears open for my worries at any time.

As one of the pioneering Ph.D. students to join the Max Planck School of Photonics graduate program, I have witnessed its remarkable evolution into an outstanding research network that provided invaluable support throughout my academic journey.

Furthermore, many thanks to you, Ines, Frank, and Sebastian - I could feel your support at any time. In particular, thank you for all the great support, my love Ina; our hearts have always been connected in the great and difficult times.

In case any of my friends from my Taekwondo club in Jena came to read this thesis: thank you as well! Practicing Taekwondo with you has given me substantial support since my childhood and still does.

Publications included in this thesis

[1] Christopher Spiess, Sebastian Töpfer, Andrej Krzic Sakshi Sharma, Thomas Grafenauer, Roland Lieger, Bernhard Ömer, Stefan Petscharnig, Michael Warum, Christoph Pacher, Gregor Sauer, Matthias Goy, Rene Berlich, Teresa Kopf, Thomas Peschel, Christoph Damm, Aoife Brady, Daniel Rieländer, and Fabian Steinlechner. **Qunet: Mobile Free-Space Quantum Communication System**. In: *QCrypt*. QCrypt, 2021, Poster Session 2. URL: https://2021.qcrypt.net/posters/QCrypt2021Poster211Spiess.pdf (see pages 9, 80).

[2] Christopher Spiess, Sebastian Töpfer, Sakshi Sharma, Andrej Krzic, Gregor Sauer, Daniel Rieländer, and Fabian Steinlechner. **Synchronization of quantum communication systems based on correlated photons**. In: *Conference on Lasers and Electro-Optics*. Optica Publishing Group, 2021, ATu1S.3. DOI: 10.1364/CLEO_AT.2021.ATu1S.3. URL: https://opg.optica.org/abstract.cfm?URI=CLEO_AT-2021-ATu1S.3 (see pages 9, 33, 48, 52, 54, 90).

[3] Christopher Spiess, Sebastian Töpfer, Daniel Rieländer, and Fabian Steinlechner. **One-way clock synchronization with single photons**. In: *Conference on Lasers and Electro-Optics*. Optica Publishing Group, 2022, AW5P.4. DOI: 10.1364/CLEO_AT.2022.AW5P.4. URL: https://opg.optica.org/abstract.cfm?URI=CLEO_AT-2022-AW5P.4 (see pages 9, 33, 61).

[4] Christopher Spiess, Luis Javier González Martin Del Campo, Nicolas Eduardo Tangarife Villamizar, and Fabian Steinlechner. **Stabilization of fiber-based interferometer with single photons**. In: *CLEO 2023*. Optica Publishing Group, 2023, FM1A.7. DOI: 10.1364/CLEO_FS.2023.FM1A.7. URL: https://opg.optica.org/abstract.cfm?URI=CLEO_FS-2023-FM1A.7 (see pages 9, 99, 100).

[5] Christopher Spiess, Sebastian Töpfer, Sakshi Sharma, Andrej Kr ži č, Meritxell Cabrejo-Ponce, Uday Chandrashekara, Nico Lennart Döll, Daniel Rieländer, and Fabian Steinlechner. **Clock Synchronization with Correlated Photons**. *Phys. Rev. Appl.* 19 (5 May 2023), 054082. DOI: 10.1103/PhysRevApplied.19.054082. URL: https://link.aps.org/doi/10.1103/PhysRevApplied.19.054082 (see pages 9, 31, 33, 42, 45, 48, 50–52, 54, 55, 59–61, 71, 79, 90, 94, 103).

[6] Christopher Spiess and Fabian Steinlechner. **Clock synchronization methods with single photon sources**. In: *Quantum 2.0 Conference and Exhibition*. Optica Publishing

Group, 2022, QTu3B.2. DOI: 10.1364/QUANTUM.2022.QTu3B.2. URL: https://opg.optica.org/abstract.cfm?URI=QUANTUM-2022-QTu3B.2 (see pages 9, 33, 55, 58, 61, 91, 92).

[7]   Christopher Spiess and Fabian Steinlechner. **Clock synchronization with pulsed single photon sources**. *Quantum Science and Technology* 9:1 (Dec. 2023), 015019. DOI: 10.1088/2058-9565/ad0ce0. URL: https://dx.doi.org/10.1088/2058-9565/ad0ce0 (see pages 9, 33, 50, 55, 59–61, 64, 69, 70, 72, 73, 90–92, 94).

Contents

1 Introduction

The synchronization of events lies at the very heart of information processing systems and distributed networks, from synchronously flashing fireflies and crickets that chirp in unison to electrically synchronous pacemaker cells [MS90]. The precise timing of events is also a central requirement in the modern information age, such as on the Internet [Bel95; van+95; van+99], cloud database services [Cor+13], financial networks [Ang14], or power grids [Pha+94]. Power grids could suffer from blackouts when there is no synchronization between demand and supply, or data on the Internet would be corrupted. Power grids and the Internet are two examples of critical infrastructure and are of great importance to society. This gives a reason for developing a secure means of data flow and, ideally, secure synchronization as well [NH18].

Quantum communication offers the unique proposition of delivering data whose confidentiality can be lower bound by the laws of physics [BB14; Eke91; GT07; NB14]. This clear bound is very attractive for secure information transfer. It motivates the establishment of a security backbone that has already grown to several hundred kilometers of fiber links and a ground space relay on more than 1000 kilometers [Che+21]. Quantum information transfer is also a great example of its tight timing budgets and the requirement for accurate synchronization of remote parties. This is similar to classical communication, where the network time protocol (millisecond precision) [Mil11] has been developed and upgraded with satellite-based clock synchronization through the Global Navigation Satellite System (GNSS) (nanosecond precision) [Ber+16] or the White Rabbit protocol (tens of picoseconds precision) [Die+16; SSR18; Wah+20]. This high precision of picoseconds or better is required for quantum communication networks with high bit rates [Tom+10] or other advanced protocols, for example quantum teleportation [Ren+17; Val+16] and entanglement swapping [Pan+98; Tsu+18]. In addition, correcting the timing offset is even necessary to ensure security [PDT22a].

In state-of-the-art experiments in quantum communication, synchronization is typically achieved by auxiliary pulsed lasers [Che+21; Lia+17; Sas+11; Wan+14; Wan+21b; Yin+20] or stable references [Wen+20], such as rubidium clocks [MLK06; Shi+20] or GNSS [Eck+21; Ste+17; Urs+07]. This resource overhead reduces the scalability [Dia+16] of quantum communication links and may even restrict its applicability in space, as there are strict limitations on power consumption and weight [Ker+18; Oi+17].

State-of-the art. Single photons themselves can be used to transfer time which follows in a reduction of the time deviations between different parties. Such quantum clock synchronization protocols have been proposed [Chu00; Gio+01; Joz+00] for multipartite network settings

[Kon+18; KP02] and with quantum enhancement beyond the possibilities of classical physics [GLM01]. In this context, the arrival times of correlated photon pairs have been used and implemented first in references [HLK09; VSS04]. Experimental setups with correlated photons have seen great advances in timing precision down to femtoseconds in different scenarios, but mostly in combination with high-precision oscillators [Hon+22; Hou+19; Lee+19; Lee+22; Lia+17; Liu+21; Qua+16; Qua+19; Qua+20; Qua+22; Wil+21; Xie+21], such as H-masers, rubidium clocks, or other means to achieve a similar clock frequency. Few approaches (including this thesis) have attempted to push this approach to its ultimate limit and derive synchronization from single-photon signals with neither additional synchronization lasers nor highly stable references [Cal+20; Cos+20; Dai+20; Fit+22; Wan+21a]. The major challenge is the time base given by unstable crystal oscillators. It reduces the signal-to-noise ratio and restricts the application scenarios to only regimes with a strong signal. A possible solution is to use a dedicated synchronization pattern [Cal+20; Sca+22; Wil+21]. This has already been successfully implemented by the references[Ave+21; Cos+20; Mar+22].

Limitations.   In the context of synchronization in quantum communication systems, we can broadly distinguish two approaches that have been used over the last years. The first approach uses fully classical synchronization systems with extreme timing precision independent of the quantum communication system. The second idea is to combine the intrinsic timing properties of the quantum optical signals at the single-photon level. In relation to the second and more recent line of research, there have been remarkable advances, in particular by [Ave+21; Cal+20; Cos+20; Fit+22; Lee+19; Lee+22; Mar+22; Qua+20; Qua+22; Wan+21a]. Despite these advances, the approaches to date still leave room for improvement, in particular with respect to the following aspects:

1. many require additional synchronization strings encoded on single photons,

2. they need highly stable (e.g., atomic) timing references or GPS receivers,

3. they include no live correction of the difference of the clock frequency.

Additionally, it would be desirable to have a better understanding of the limitations and benefits of the approach. To this end, it would be desirable to have:

4. a detailed discussion and simple formal expressions of the timing uncertainty under drifting references,

5. a rigorous analysis of the performance and limitations of the synchronization algorithms.

In the following, I will describe the five technology and knowledge gaps in more detail.

Including **additional synchronization strings (1.)** is a great method to increase the signal-to-noise ratio of the synchronization signal [Cal+20; Sca+22; Wil+21]. Such patterns have

been successfully implemented in scenarios with pulsed (clocked) single photon emission as a derivative of the BB84 quantum key distribution protocol [Ave+21; Cos+20; Mar+22]. However, since these patterns are part of the single-photon stream, this method requires modifications to the source with modulators. Although the modulators are already integrated and part of faint pulse sources [BB14], this is not the case in systems based on correlated photons [BBM92a], which would require this additional resource. Furthermore, adding separate synchronization strings reduces the effective data rate [Cal+20]. These are the reasons for developing a different scheme in this thesis without the need of synchronization strings.

Adding **stable references (2.)** substantially increases the timing precision and is widely used when receivers are separated by long distances. Such stable references could be combinations of atomic references (e.g., rubidium or hydrogen maser) [Hon+22; Lee+19; Lee+22; Qua+20; Qua+22] or GPS receivers [Eck+21; Ste+17; Urs+07]. They ensure that the frequency difference between the clocks is sufficiently small. This is also achieved by using the same frequency reference as provided by a master clock [Hou+19; Liu+21; Qua+16; Qua+19; VSS04; Wil+21], which could also be shared via a classical laser link [Lia+17]. Any of these methods increases the resource effort and thus reduces the scalability of quantum communication networks. Classical communication systems already reached such maturity without atomic references. A central overarching objective of this thesis work is to develop techniques that will advance the synchronization of quantum communication networks to a similar level.

In satellite-based communication scenarios, the data are recorded and then processed (**no live correction, 3.**) while the satellite is not in view of the ground station. After a few minutes of exchanging quantum bits of information, there is enough time to process the information until the satellite appears again. The careful processing of the timing makes a lot of sense in these settings. There is just not much data and all the computation resources should be spent on extracting as much secure data as possible. This also includes finding a method for an optimized state of synchronization [Dai+20; Lia+17; Wan+21a]. This becomes critical in scenarios with high data rates, as expected in communication links on the ground. Here, there is not much time to spend on processing. Furthermore, it might not be possible to store all the data over several days of communication and process it later, as large storage capacity is needed. This is why we should develop live synchronization algorithms that update the clock in real time [Ave+21; Cos+20; Fit+22; Mar+22]. This could also give a novel application scenario of measuring the distance, velocity, and acceleration of moving objects in real time - this is part of the outlook of this thesis.

One general gap that is missing is a detailed discussion of the **timing uncertainty (4.)** under drifting references. The timing uncertainty can be described by a sum of the standard variances from all noise sources, considering timing jitter from, e.g. detector, source, or analog-to-digital converter. However, this is no longer the case when we consider drifting time references. Random frequency noise introduces asymmetries in timing statistics. Such a model is still

missing, as well as a comprehensive connection between the difference of the clock frequency and the timing uncertainty, and will be addressed in this thesis.

Several publications show an algorithm for synchronizing clocks, but do not describe its **performance and limitations (5.)** in terms of synchronization timing jitters or timing stability and computational effort. Initial demonstrations of correlation-based clock synchronization methods did not indicate a complete analysis of the performance [HLK09; VSS04]. Recent publications [Cos+20] also describe an algorithm with synchronization strings in great detail and apply it to state-of-the-art systems successfully [Ave+21; Mar+22]. They show impressive quantum key distribution results, but a detailed analysis of the algorithm is missing as of today. In the publication [Fit+22], synchronization with single photons is applied, which allows a continuous quantum key distribution operation. However, the description of the synchronization algorithm is incomplete and suffers from a lack of understanding of its performance. These are two more aspects that are investigated in this thesis to provide a more complete picture on synchronization with single photons.

Challenges. This thesis extends on initial demonstrations of correlation-based clock synchronization [HLK09; VSS04], which require neither hardware (sender and receiver) nor software modifications of the single-photon source [Fit+22; Wan+21a]. My work broadens the view from publications [Fit+22; Wan+21a] by providing an extensive discussion of a single-photon clock synchronization protocol, a detailed study on the optimization of such protocols, and a comprehensive performance analysis.

In particular, the thesis addresses the following objectives:

1. enable synchronization in scenarios with very low signal to noise ratios, similar to long-distance free-space links [Eck+21]

2. use only unstable crystal oscillators with fluctuating frequencies; no addition synchronization laser, atomic references or other additional hardware,

3. enable robust operation under strong signal fluctuations and signal loss, as on turbulent free-space links, and to

4. ensure live operation of the algorithms.

Addressing these challenges results in the following research questions that guided the thesis work.

Approaches to address the challenges. In any of the application scenarios in the thesis, standard crystal oscillators have been used. They are challenging to work with, due to their low frequency accuracy that is up to 8 orders of magnitude higher than in atomic references [Bre97; TA19]. This results in strong temporal drifts and high timing uncertainties during

the initialization of the synchronization. When the signal is weak, this could even prevent successful synchronization. These weak signal scenarios are tested on realistic link scenarios. In such cases, my results will show that frequency sweeps can be used to establish a successful initialization of the synchronization [2; 5; Wan+21a]. During the synchronization session, the low stability of the crystal oscillators (orders of magnitude weaker than in atomic references) introduces frequency differences between the clocks that lead to a drastic increase in the timing error. Nevertheless, my work shows that very high synchronization performance can be achieved by utilizing the single-photon timing information. In summary, the following points help to address the challenges and are the main outputs:

1. The thesis provides a full description of the uncertainty of the arrival time for clocks with constant and varying frequency offset.

2. The thesis introduces frequency sweeps to compensate for the difference in clock frequency during the initialization of clock synchronization. This appeared first in my publication [2], and later in [5] (published on arXiv in year 2021). After this publication, the same method has been applied to compensate for the Doppler shift in satellites for quantum communication [Wan+21a] or to initialize quantum key distribution sessions [Fit+22].

3. The thesis develops a live tracking algorithm during the synchronization session (my publications [3; 7]). Other publications did not include algorithms [Fit+22] or methods for live synchronization are not developed [Dai+20; Lia+17; Wan+21a].

4. The thesis provides an optimized synchronization algorithm for clocked single-photon sources (my publication [6; 7]).

5. The thesis applies the synchronization protocol to a real 1.7 km turbulent free-space link in the QuNet framework [1] and a 70 km intercity link.

Note that in this thesis, I will repeatedly refer to content from my own publications [1; 2; 3; 4; 5; 6; 7]. For the sake of better clarity, I cite these in numerical style [1-7], and refer to the work of others using [Author + YY].

Structure of the thesis.

- Chapter 2 of the thesis provides an introductory summary of clocks, noise sources and how they affect synchronization performance.

- Chapter 3 introduces methods for time transfer to increase the performance of synchronization. This is critical in various applications, including advanced quantum communication protocols. Fortunately, this time transfer can be done by using the single photons that exist naturally in a quantum communication network.

- Chapter 4 describes all the methods for exploiting the single-photon timing information. Furthermore, it describes steps to increase the signal-to-noise ratio. The section focuses on the initialization of the synchronization procedure, which is a very critical point, due to its high risk of failure.

- Chapter 5 starts from the point of successful initialization and focuses on the next step, which is the live tracking session, where new timing data is continuously generated and processed. As time passes, the frequency of the crystal oscillators varies rapidly. Here, a frequency tracking and compensation mechanism is introduced. The highlight of the chapter is the implementation of the synchronization algorithms in a quantum key distribution scenario on a 1.7 km intracity free space and 70 km intercity fiber link between Jena and Erfurt.

- Chapter 6 discusses other applications that benefit from the described algorithms. In a broader sense, this thesis deals with use cases of low signal-to-noise ratios and hence also applies to strongly attenuated classical optical systems, e.g. long-distance ranging, synchronization, or metrology of surfaces and objects with weak reflectivity.

In summary, these main outcomes enable the application of the synchronization protocol in real deployed link experiments in fiber and free space to enable quantum key distribution with the smallest hardware overhead. I developed methods for both clocked and asynchronous single-photon sources. They are robust to any clock type (even crystal oscillators) and I confirm the feasibility at several application scenarios, such as low-signal regimes, turbulent free space, or long-distance fiber links. The methods are ready for implementation in any quantum communication network, where synchronization is a by-product of the data exchange without compromising the data rate. They represent important advances toward more secure transfer [Dai+20], single-photon metrology, high-performance synchronization at the interferometric level, and global precision time distribution [Tro+22].

2   Fundamentals

Clocks are the foundation of the modern information-based society. They provide a reliable time and frequency reference and ensure that time-critical events can be related to the same standard. Depending on the application, the type of clock significantly affects communication and time transfer might not even be required, as the clocks could already be stable enough. For example, classical communication relies on the network time protocol with 1 ms timing jitters [Mil11], which can be provided with low-performance standard crystal oscillators [TA19]. On the other hand, quantum communication networks require picosecond synchronization. This degree of performance is usually only attainable with atomic references and motivates us to look deeper into the clock stability.

The following chapter focuses on:

1. the synchronization in systems for quantum key distribution,

2. the derivation of the timing stability in clocks, following an analytical (Allan deviation) and numerical model (Gaussian white noise sources),

3. the noise sources and clock types with its corresponding impact on the timing stability.

The following sections are divided into a first part that is dedicated to motivating the need of synchronization with an example of quantum key distribution (Section 2.1), as one application of this thesis. The next section describes the derivation of time from oscillators (Section 2.2). Subsequently, I model the clock's time dependence under various noise sources (Section 2.3) and compare the time dependence of poor-performing crystal oscillators with high-performance atomic references (Section 2.4).

2.1 Synchronization in systems for quantum key distribution

Before we start to look into the fundamentals, I will motivate the need of synchronization with single photons by a concrete example: prepare and measure quantum key distribution [BB14; Cao+22; Gis+02] as a subgroup of quantum communication. Figure 2.1 depicts an exemplary system with all processing blocks that ultimately yields a secure key. As in classical communication, it is essential to reduce the impact of noise to a minimum. In classical communication, the bit is increasingly harder to detect when the noise becomes stronger. Classical systems have the advantage that they use high intensity laser light. This provides redundancy and increases

the probability of a successful transfer of bits without errors. This is very different in quantum communication. Every single photon that comes from background noise will contribute and immediately increase the errors. In other words, quantum communication systems are not as resistant to noise because every single photon matters and is processed.
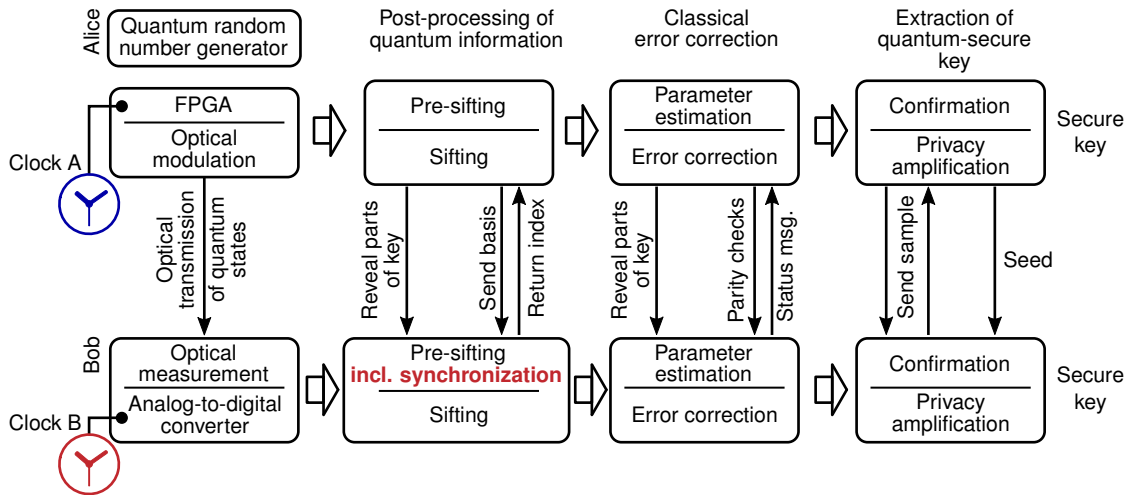

Figure 2.1 | Exemplary application scenario of the synchronization protocol: quantum key distribution. The example bases on a scheme where a quantum-secure key is prepared by a sender Alice and measured subsequently by the receiver Bob. The key is generated in a quantum random number generator and transferred to the optical domain via a field programmable gate array (FPGA) and optical modulators. The receiver measures the quantum states. It follows several processing blocks to extract a quantum-secure key from the transferred quantum states. Relevant for the thesis is the synchronization of the received states with the sender, which is the requirement for all other steps to follow.

One elegant way of reducing the noise in quantum communication is by implementing a temporal filter, as the arrival time of the signal photons is known with some detection uncertainty. On the contrary, the arrival time of the photons from a noise source is random. In practice, the temporal filter is on the order of 1-3 standard deviations of the detection uncertainty (smaller than 1 ns). The concrete value depends on the noise figure, i.e. narrow temporal filter reduce the signal, but makes sense when the noise is strong. This works very well in filtering out the noise.

The temporal filter is no longer reliable when the relative arrival time varies. Clocks that are not synchronized give rise to shifts in time and move the signal out of the temporal filter. As a consequence, the signal-to-noise ratio is reduced and the relative number of errors increases. Quantum key distribution systems require the synchronization of clocks and the reduction of arrival time fluctuations to values much smaller than 1 ns (depending on the uncertainty of detection).

In classical synchronization systems, the challenge is to synchronize the clocks themselves. It requires to isolate the fluctuations in transmission time on the optical link. After synchronizing the clocks, the time reference is used to provide time stamps for any event. In most quantum key distribution protocols, such as BB84 [BB14] or BBM92 [BBM92b], it is possible to skip

the first step and directly synchronize the events. These events are the arrival times of single photons, where synchronization can be achieved via simple post-processing as done in this thesis. Drifting clocks or fluctuating arrival times due to the optical link are compensated simultaneously by simply adding a correction value to the arrival times of the photons. Protocols based on optical interference, such as derivatives of measurement device-independent protocols [LCQ12], require an isolated analysis and additional physical compensation of the path length of the optical link. Here, synchronization could be achieved by a two-way time transfer [Gio+13] that provides a measure independent of the path length. Several publications have already shown its successful implementation with single photons [Hon+22; Hou+19; Qua+22; Xia+22].

Synchronization is essential in systems for quantum key distribution. It is the first step in the post-processing of quantum information and ensures that all other processing blocks can run smoothly with low error rates (Fig. 2.1). The system requires synchronization at the picosecond level that will likely become stricter with more advanced and high-speed protocols. As I will show in this thesis, such a level of synchronization can be achieved conveniently with the single photons themselves. They are naturally integrated in quantum key distribution systems, where I demonstrate reliable operation in the following chapters.

One important component when it comes to the clock synchronization is the performance of clocks, as this decides the precision and accuracy needed for the time transfer with single photons. I will go through the fundamentals of clocks in the next section.

2.2 The clock as an oscillator

Clocks can be represented as an oscillator with a frequency and a phase that vary over time. The actual time reading is derived from the phase evolution and is used to time-stamp incoming events. These time readings between clocks can be very different when there are large deviations of the frequency. This section describes this important parameter of the *frequency deviation* and its impact on the time reading.
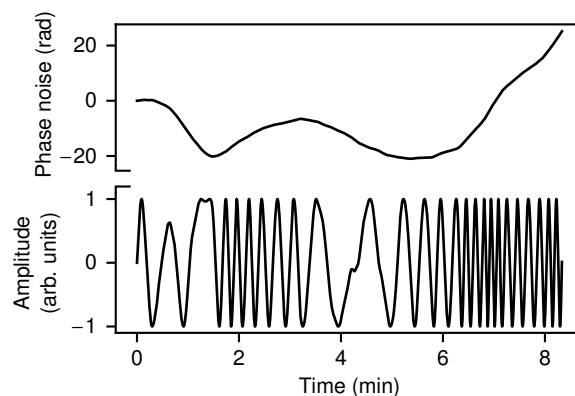

Figure 2.2 | Noise in oscillators. Phase noise introduces a variation of the frequency reference. The nominal frequency ν_0 is 0.04 Hz, step size 10 ms with the frequency noise standard deviation being $\sqrt{10^{-3}} \times 10$ ms.

Table 2.1 | Description of the parameters used to characterize the clock performance.

Parameter	Formula	Description
$\phi(t)$	-	Phase deviation of a real oscillator
$x(t)$	$\phi(t)/(2\pi v_0)$	**Time deviation** of a real oscillator
$h(t)$	$t + x(t)$	Time reading of a real oscillator
$y(t)$	$dx(t)/(dt)$	Normalized **frequency deviation** of a real oscillator
$v(t)$	$v_0 dh(t)/(dt)$	Frequency reading of a real oscillator

Noisy oscillators indicate deviations of their phase $\phi(t)$ with respect to an ideal reference. This can also be related to a time deviation $x(t)$ from an ideal oscillator. The real-time reading $h(t)$ is the time of an ideal oscillator t summed with its time deviation. The frequency deviation $y(t)$ is the time deviation derived with respect to time. The actual frequency reading $v(t)$ from the oscillator originates from the time reading $h(t)$. The time deviation $x(t)$ and frequency deviation $y(t)$ depend on the noise source and strength.

Any type of clock generates a sinusoidal output signal with amplitude U_0, nominal frequency v_0, phase deviation $\phi(t)$ and time reading $h(t)$ (Fig. 2.2),

$$u(t) = U_0 \sin(2\pi v_0 t + \phi(t)) = U_0 \sin(2\pi v_0 h(t)). \tag{2.1}$$

The model provides the basis for deriving the time and frequency and the corresponding time deviation and frequency deviation. These deviations relate the time and frequency reading to the values of an ideal oscillator. All parameters are summarized in Table 2.1. The time reading of the oscillator (including the phase deviation $\phi(t)$) can be described as

$$h(t) = \underbrace{t}_{\text{Ideal osc.}} + \underbrace{x(t)}_{\text{Time dev.}}, \tag{2.2}$$

with the time of an ideal oscillator (osc.) t and its time deviation $x(t)$ being,

$$x(t) = \frac{1}{2\pi v_0}\phi(t). \tag{2.3}$$

The reading of the instantaneous frequency is derived through the time reading $h(t)$,

$$v(t) = v_0\frac{dh(t)}{dt} = \underbrace{v_0}_{\text{Ideal osc.}} + \underbrace{v_0\frac{dx(t)}{dt}}_{\text{Frequency dev.}}, \tag{2.4}$$

and is a sum of the frequency of an ideal oscillator v_0 and its corresponding deviation. From the instantaneous frequency, one can derive a dimensionless parameter, called the normalized frequency deviation $y(t)$. It relates the deviation of the real clock to the frequency of an ideal reference with frequency v_0,

$$y(t) = \frac{v(t) - v_0}{v_0} = \frac{dx(t)}{dt}. \tag{2.5}$$

Table 2.2 | Performance of different oscillator types.			
Oscillator type	**Accuracy (ppm)**	**FWHM timing jitter**	**Costs (€)**
EXO	10-100	0.5 - 5 μs	≈ 1
TCXO	2-10	0.1 - 0.5 μs	≈ 5
Rubidium atomic	10^{-6}	50 fs	≈ 1000
Cesium beam	10^{-7}	5 fs	≈ 3000

The table describes the normalized frequency deviation (accuracy) and its created timing jitter of external crystal oscillators (EXO), temperature-controlled crystal oscillators (TCXO), rubidium atomic oscillators and cesium beam references [TA19]. The full-width at half-maximum (FWHM) timing uncertainty δ_{FWHM} is estimated via the normalized frequency deviation y and the integration time ΔT of 100 ms as $\delta_{\mathrm{FWHM}} \approx y\Delta T$

This normalized frequency deviation is widely used to characterize the clock performance. For example, external quartz crystal oscillators reach normalized frequency deviations of 10-100 ppm ($10^{-5} \ldots 10^{-4}$) and rubidium oscillators 10^{-6} ppm (10^{-12}) on average (see Table 2.2). This frequency offset describes the *accuracy* of clocks. It represents a convenient figure of merit as we proceed in the thesis because it provides an expected timing uncertainty of the synchronization protocol due to the frequency deviation of a clock.

2.3 Modelling the time dependence of clocks

The phase and frequency of the clock change continuously as time passes. This effect can be summarized by the *precision* of the clock. The precision is influenced by different kinds of noise sources that give rise to deviations of the absolute time with respect to an ideal clock. In this section, I introduce these noise sources and show how the time and frequency deviations are conveniently described in terms of the Allan deviation [WD08]. In contrast to the standard deviation, which is a single value, the Allan deviation provides a measure of the clock's stability over a range of averaging times from short-term to long-term. This is important because clocks may exhibit different levels of stability over different time scales, and it is often necessary to know the stability at different time scales for various applications. In particular, applications with low signal (such as satellite-to-ground communication) require long integration times. Here, frequency drifts play an important role. On the other hand, communication links with strong signal (such as short distance links) can choose small integration times and find a major impact from white noise.

The clock model. The time deviation $x(t)$ and the frequency deviation $y(t)$ depend on the phase deviation of the oscillator $\phi(t)$ as described in the last paragraph. Using these expressions (Equation 2.3 and 2.5), we can create the most general description of the time-dependent time

deviation by adding a generic noise source $w(t)$ [KMH12]:

$$x(t) = \int_0^t y(t')\mathrm{d}t' + w(t). \tag{2.6}$$

Note that the frequency deviation $y(t)$ is also time-dependent and includes noise sources that affect the frequency. For a constant frequency deviation, the model can be simplified to $x(t) = y_0 t + w(t)$, as described in Ref. [VBP04]. However, it is no longer considered in the following, as real clocks have time varying frequencies. The continuous model in Equation 2.6 can also be discretized to time-step sizes $\Delta T(i)$ for numerical calculation purposes,

$$x(n) = \sum_i^n y(i)\Delta T(i) + w(n). \tag{2.7}$$

We can decompose the generic noise source $w(n)$ into several components that each contribute differently to the final timing uncertainty. Even the frequency $y(i)$ itself changes due to its own noise source. The following three noise sources contribute to the measured time deviation between clocks,

1. Measurement noise w_M (variation of phase),

2. White frequency noise w_W (variation of velocity), and

3. Random walk frequency noise w_{RW} (variation of acceleration).

Each of these noise sources is described by Gaussian white noise, i.e., uncorrelated (random) processes. However, the final effect of these noise sources on the measured timing offset will differ significantly (Fig. 2.3**a**). The three noise sources can be visualized with the example of a location measurement of a moving object (runner, car, satellite, aircraft, etc.). The measurement itself represents some uncertainty (measurement noise, w_M). The object may also have some fluctuations of its speed (white-frequency noise w_W), caused by, e.g. sudden turbulences. The third cause of a change in the location of the object is its acceleration (random walk frequency noise w_{RW}), due to an applied force.

In the clock model, the change in frequency deviation $y(t)$ and timing offset $x(t)$ is described by independent sources of Gaussian white noise. If Gaussian white noise affects the frequency, then we see it in the final time deviation as random walk frequency modulation (RW FM) noise. On the other hand, if Gaussian white noise affects the timing offset, we see it as white FM noise in the final time deviation. I will elaborate more on this after we see how they are connected in the following recursive state equations. In accordance with the effect on the final time deviation, we call the source of Gaussian white noise applied to model the frequency deviation and time deviation w_{RW} and w_W, respectively. The recursive state equations are [GN11] (excludes measurement noise),
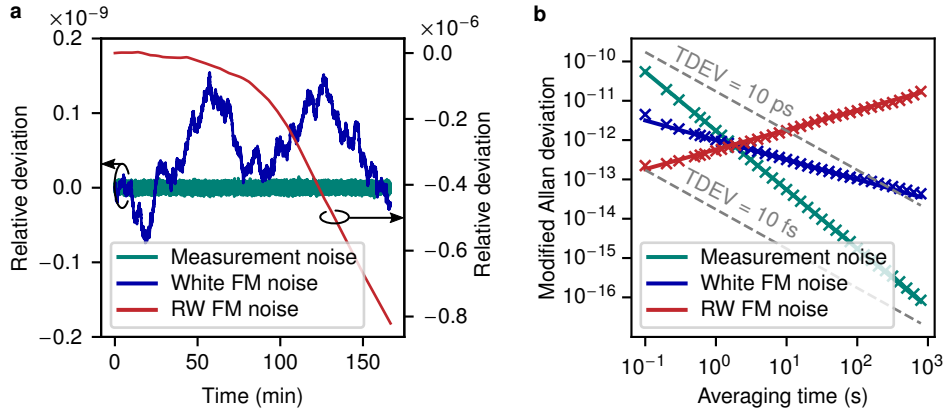
Figure 2.3 | Modelling the clock. The timing deviation of the clock is described by the consistent impact of white frequency modulation (FM) noise and random walk (RW) FM noise. **a**, The white FM and RW FM noise results in an accumulation of relative frequency deviations. On the other hand, the measurement noise has a mean value of zero. **b**, The modified Allan deviation (MDEV) for the different noise sources. The lines correspond to the analytical representation (Equation 2.13) and the data points represent the numerical model (Equations 2.8 and 2.9). The dotted gray lines show the MDEV for a given Allan time deviation (TDEV) at values of TDEV = 10 ps and 10 fs, for reference, with MDEV = TDEV/$(\sqrt{1/3}\tau)$ (Equation 2.11). Every noise source x has a standard variance $\sigma_x^2 = 10^{-24}$.

$$y(n) = y(n-1) + w_{\text{RW FM}}, \tag{2.8}$$

$$x(n) = x(n-1) + y(n)\Delta T(n) + w_{\text{white FM}}. \tag{2.9}$$

The Gaussian white noise for RW FM and white FM noise have standard deviations $\sigma_{\text{RW}}\sqrt{\Delta T}$ and $\sigma_{\text{W}}\sqrt{\Delta T}$, respectively.

Any Gaussian white noise source that affects the frequency $w_{\text{RW FM}}$ propagates to the final time deviation $x(n)$ in **two** accumulation processes: 1. accumulating the frequency deviation $y(n)$ (Equation 2.8) that is used to (2.) estimate the time deviation $x(n)$ that accumulates again (Equation 2.9). The final noise in the time deviation is called RW FM noise. Figure 2.4 gives a graphical representation of these two accumulation loops. Gaussian white noise sources that affect the time deviation $w_{\text{white FM}}$ propagate to the final time deviation in **one** accumulation process only. This process is represented by the accumulation of time deviation (Equation 2.9). The final noise in the time deviation is called the white FM noise. Note that the (Gaussian) measurement noise is not part of the clock model. It is outside of the recursive state equations, following in **no** accumulation process. The final noise in the (measured) time deviation is called the white PM noise. The noise sources are summarized in Table 2.3.

The recursive state equations provide the numerical model for emulating the time dependence of clocks in an experiment for given standard deviations of Gaussian white noise (Fig. 2.3**a**). In the following, I will use the derived noise model and show its impact on the Allan deviation that is measured in the experiment. This connection provides a powerful tool to find the types of noise in the system (RW FM, White FM, White PM) and indicates the corresponding strength.
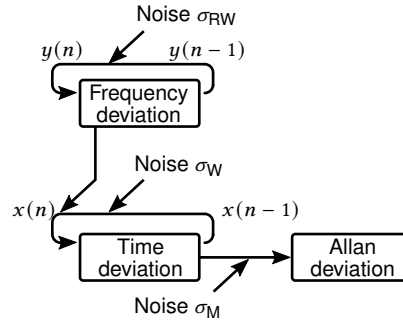
Figure 2.4 | Modelling the time deviation of clocks. The time deviation is modelled in a two stage process. First, a new value of the frequency deviation $y(n)$ is calculated. Second, the new frequency deviation is used to simulate the time deviation $x(n)$. Numerically, all noise sources represent Gaussian white noise with standard deviation σ_{RW}, σ_W, σ_M that represents random walk noise, white noise, and measurement noise in the final time deviation. Although all of them are implemented as white noise, their impact on the final time deviation is not the same (Fig. 2.3). The corresponding recursive state equations are the Equations 2.8 and 2.9.

The Allan deviation. The numerically modeled time dependence now is transferred to an analytical trend of the clock stability. The stability is characterized by the modified Allan deviation (MDEV) and Allan time deviation (TDEV). The MDEV is a figure of merit for the average standard deviation of the frequency uncertainty $y(t)$ and the TDEV refers to the uncertainty or the error of the time $x(t)$ between two clocks. The modified Allan deviation $\sigma_y(\tau)$ (modified Allan variance, MVAR, $\sigma_y^2(\tau)$) is described for different averaging times $\tau = m\Delta T$ at m sampling points from a set of N measurements as [WD08, p. 17],

$$\sigma_y^2(\tau) = \frac{1}{2m^2\tau^2(N-3m+1)} \sum_{j=1}^{N-3m+1} \left(\sum_{i=j}^{j+m-1} x\underbrace{(i+2m)}_{n_0} - 2x\underbrace{(i+m)}_{n_1} + x\underbrace{(i)}_{n_2} \right)^2, \qquad (2.10)$$

with the time Allan variance (TVAR) $\sigma_x^2(\tau)$ and time Allan deviation (TDEV) $\sigma_x(\tau)$ being,

$$\sigma_x^2(\tau) = \frac{\tau^2}{3}\sigma_y(\tau)^2 \qquad (2.11)$$
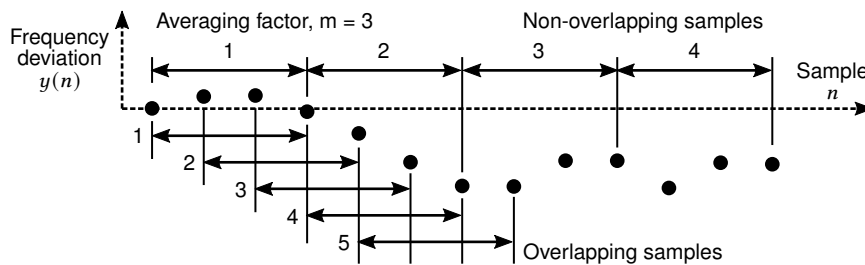

Figure 2.5 | Comparison of non-overlapping and overlapping sampling as in the modified Allan deviation. Sampling points of the time deviation $y(n)$ and calculation of the modified Allan deviation that is based on overlapping sampling. Here, the averaging time is $\tau = m\Delta T$ (m = 3). Modified figure from Ref. [WD08].

Table 2.3	Noise sources.		
Noise source	**Noise color**	**Allan deviation**	**PSD**
Frequ. drift (RR)	Black	$\propto \tau^1$	$\propto f^{-3}$
RW FM	Brown	$\propto \tau^{1/2}$	$\propto f^{-2}$
White FM	White	$\propto \tau^{-1/2}$	$\propto f^0$
White PM	Violet	$\propto \tau^{-3/2}$	$\propto f^2$

Allan time deviation σ_y for varying averaging times τ and power spectral densities (PSD) [WD08] for random run frequency modulation (RR FM), random walk frequency modulation (RW FM), white noise frequency modulation (White FM) and white noise phase modulation (White PM). The noise color refers to the noise spectrum. For example, white noise has a flat spectral density ($\propto f^0$). The measurement noise of the timing offset is represented by white PM noise and the clock frequency change by a white component (white FM, standard variance σ_W^2) and a random walk component (RW FM, standard variance σ_{RW}^2). The RW FM, White FM and White PM noise is derived by differentiating the frequency drift noise 1 times, 2 times or 3 times, respectively.

The equation sums up the frequency difference between two points in time by overlapping the sampling. An intuitive description of overlapping sampling is given in a figure from Ref. [WD08] (Fig. 2.5). The frequency deviation $y(n)$ is the derivative of the time deviation $x(n)$ with respect to time (here: time step $\Delta T(n)$),

$$y(n) = \frac{x(n) - x(n-1)}{\Delta T(n)}. \tag{2.12}$$

As the Allan deviation requires two frequencies, for example, $y(n)$ and $y(n-1)$, we need three values of the time deviation for their calculation, for example $x(n)$, $x(n-1)$, and $x(n-2)$. This can be generalized as the three points being $x(n_0)$, $x(n_1)$ and $x(n_2)$, as given in Equation 2.10 for overlapping sampling. The Allan deviation $\sigma_y(\tau)$ returns the average deviation of the frequency for a given averaging time that can also be considered as the integration time of a measurement. Essentially, this deviation is the measurement error and is equivalent to the standard deviation for a given integration time, which might be more known to the reader. Together with the state Equations 2.8 and 2.9, this represents a very simple analytical expression [ZT05] (excludes measurement noise),

$$\sigma_y^2(\tau) = \frac{\sigma_W^2}{\tau} + \frac{\sigma_{RW}^2 \tau}{3}. \tag{2.13}$$

The evolution of the time deviation with respect to the averaging time depends solely on the variances for white noise σ_W^2 and random walk noise σ_{RW}^2 (Fig. 2.3**b**). For a comparison of the noise sources, see Table 2.3. The measure of timing stability in terms of Allan deviation is of great importance later in the process of characterizing the synchronization stability. I will show that the time deviation reduces significantly by introducing algorithms for time-transfer based on single photons.

2.4 Clock types

The frequency deviation and frequency stability strongly depend on the type of clock. The most prominent examples are (quartz) crystal oscillators and atomic references, such as rubidium clocks. Atomic references intrinsically indicate a much higher stability, since the resonance frequency is based on single atoms. On the other hand, the resonance frequency in crystal oscillators is highly dependent on the manufacturing tolerances of the quartz crystal, which lowers their frequency accuracy.

2.4.1 Crystal oscillators

Crystal oscillators are low-cost, small in size, and have low power dissipation. The crystals are prepared and inserted into an electric circuit with a gain provided by an amplifier (Fig. 2.6**a**). Before powering up the circuit, there is only white frequency noise. This corresponds to having no bias toward any frequency, i.e. all frequencies have the same intensity. The white noise is caused by thermal fluctuations that influence, for example, resistors (Johnson noise [Joh28]). An alternative reason is intrinsic fluctuations of discrete charges (shot noise [Wal18]). As the electrical circuit represents an electrical resonator, the resonating frequency is amplified. In this way, the circuit provides a frequency that is stabilized by the crystal and returned to the user. The output frequency deviates for several reasons (Fig. 2.7), such as [Vig08],
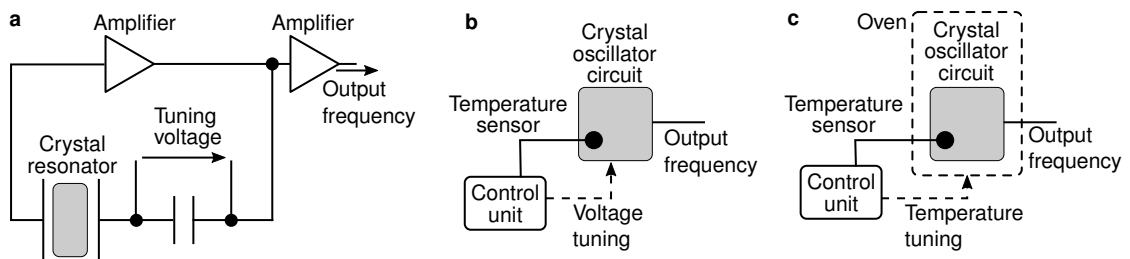

Figure 2.6 | Crystal oscillator clock types. a, Standard crystal oscillator circuit (XO). Starting from noise, the frequency that satisfies the constructive phase condition (multiple of 2π) for the oscillation is propagated around the loop with increasing amplitude. Environmental factors change the intrinsic crystal frequency and the resonator's output frequency, as a consequence. **b**, Temperature controlled crystal oscillator (TCXO) circuit. In a control circuit, the resonance frequency is modified by a tuning voltage to compensate for changes in temperature. The crystal itself is not affected. **c**, Oven-controlled crystal oscillator (OCXO) circuits provide the highest stability. The control circuit changes not only the tuning voltage but also a temperature-controlled oven that affects the crystal directly. Figures modified from Ref. [Vig08].

- time (change of system parameters over time),

- temperature (thermal expansion, refraction index change, mechanical stress of the crystal structure),

- acceleration (introduction of stress),

- ionizing radiation (damages to crystal structure), or

- other, like humidity, atmospheric pressure, power supply, etc.

The frequency deviations have their origin in the mere physics of a crystal oscillator. The resonance in quartz crystal oscillators is determined by the mechanical vibrations of the quartz crystal itself. However, the environment can introduce minute changes in the crystal's dimensions, altering its resonance frequency and cause the oscillator to deviate from its ideal frequency over time. This is much different in atomic clocks (e.g. rubidium) that rely on the atomic property of hyperfine transitions. They remain relatively unaffected by external factors such as temperature variations and mechanical stress.

In practice, the frequency deviations caused can be reduced by feedback loops in the electrical circuit. In particular, feedback loops to compensate for the effect of temperature are straightforward to implement. The simplest implementation is temperature-controlled oscillators (TCXO, Fig. 2.6**b**), where a temperature sensor provides feedback to a tuning voltage in the electric circuit that counteracts the impact of a change in temperature. The technical complexity increases when an oven is added to control the temperature of the crystal itself (OCXO, Fig. 2.6**c**). This significantly improves the stability of the frequency (Fig. 2.9). In our experimental setup, we have crystal oscillators with a datasheet accuracy of ±20 ppm, aging ±3 ppm/ first year, ±1 ppm/year and temperature dependence ±0.125 ppm (25°C ... 85°C). This is consistent with external crystal oscillators without any temperature-controlled feedback mechanism [TA19] and highlights their very poor stability in contrast to atomic references that can easily achieve 10^{-6} ppm.
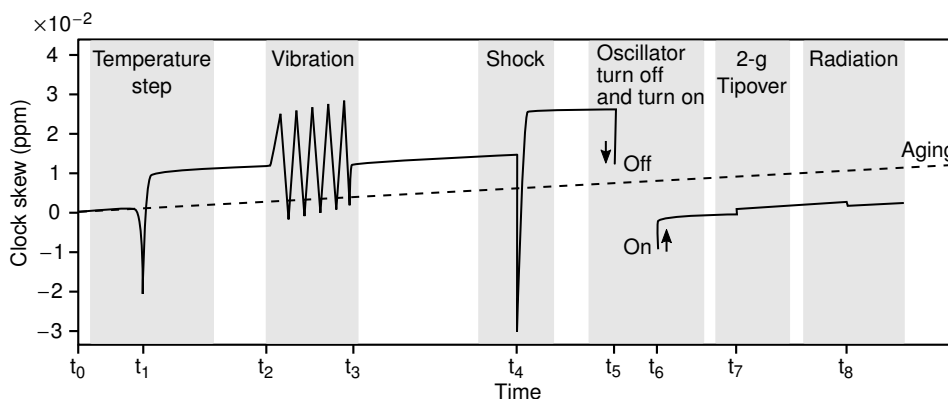
Figure 2.7 | Influences on the clock frequency. Temperature, vibration, shock, gravitational forces (g = gravitational constant), radiation or the mere fact of turning the oscillator off and on will impact the clock frequency. Figure modified from Ref. [Vig08].

2.4.2 Atomic oscillators

Atomic oscillators, such as rubidium atomic references, lock their frequency to hyperfine transitions of atoms in an electrical feedback loop (Fig. 2.8**a**). In the case of rubidium atomic

clocks, the output light from a rubidium cell is detected and the intensity tracked in an electro-optical circuit. When the microwave circuit matches the resonance frequency of the rubidium atoms, the detected light intensity is the smallest. In this way, the frequency of a quartz oscillator is adjusted and disciplined to the frequency of the rubidium transition. In the last step, the signal from the disciplined quartz oscillator is amplified and provided to the user. The source of the oscillation depends on the atomic characteristics, whereas the quartz crystal clocks depend on the precision of the manufacturing process used to create the quartz crystal. The atomic characteristics provide great benefits in terms of timing precision. For example, in the experimental setup discussed in the following, we use rubidium clocks with accuracy $\pm 10^{-4}$ ppm (ambient temperature 0℃ . . . 40℃), aging $< 5 \times 10^{-5}$ ppm/month and a stability of 10^{-5} ppm over 1 s.
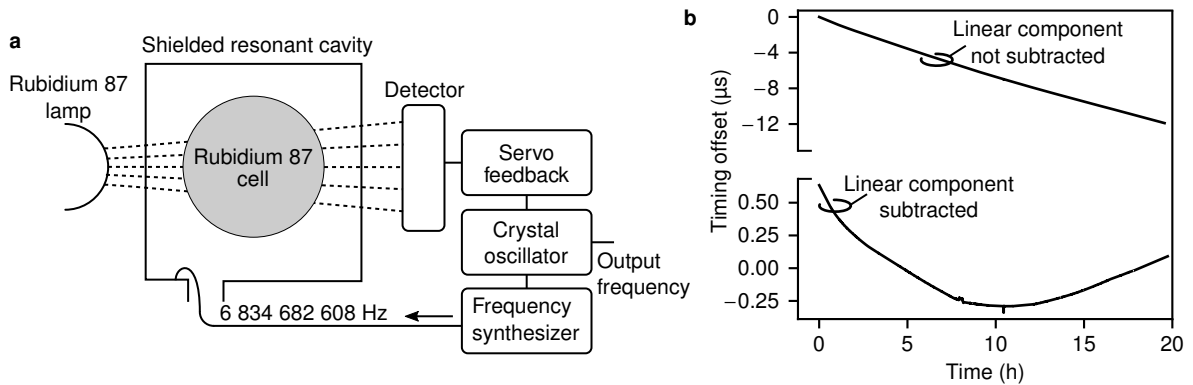

Figure 2.8 | Operating principle of rubidium oscillators and corresponding change in timing offset. a, The crystal oscillator is disciplined to the rubidium hyperfine transition at 6 834 682 808 Hz. At the resonance frequency, i.e. the rubidium transition, the detected intensity is smallest. This acts as a feedback signal. Simplified figure from Ref. [CD15]. **b**, The drift in time of our rubidium clocks amounts to approximately 440 ps/s. When subtracting this constant frequency difference after a fit, there is a residual variation of timing offset, due to the instability of the clock frequency.

Another type of atomic oscillators are hydrogen masers that indicate at least one order of magnitude better stability. This comes from the fact that there is much less number of atoms, which reduces the probability of atomic collisions. In addition, the atoms have a smaller thermal velocity (small Doppler broadening) that both give rise to a narrow resonance width. Their narrow resonance widths allow for a high coherence time, following a more precise and stable frequency and timing reference. [Lom03]

Atomic references at every receiver in a network give rise to a small frequency deviation. Furthermore, the setup does not depend on the optical link quality, as no synchronization signal is transferred. The change in timing offset with our free-running rubidium atomic references amounts to 1.6 μs/h (440 ps/s, Fig. 2.8**b**). This residual timing offset requires compensation by means of time transfer for a successful communication session (see Chapter 3). The timing offset introduced corresponds to FWHM timing jitters of approximately 440 ps at 1 s integration times. At integration times of 100 ms, the timing jitter is, with approximately 44 ps, very small and close to state-of-the-art nanowire single-photon detectors with 25 ps [QUA22; Qua22]. The only

downside of using rubidium clocks is their scalability. It is very resource-intensive to deploy them at every receiver in a communication network. This is the reason why several orders of magnitude more quartz oscillators are sold in the frequency control market (3×10^9 quartz crystal oscillators per year and 5×10^4 rubidium oscillators per year [Vig08]). Future quantum communication networks are likely to follow a similar trend. They demand resource-saving equipment but with the same or higher clock synchronization performance as rubidium clocks. Here, high-performance time-transfer techniques are introduced to compensate for the poor stability of crystal oscillators.

2.4.3 Conclusions

The type of clock used in a quantum communication system has a major impact on the performance of the synchronization. Atomic clocks, such as rubidium oscillators, indicate the highest frequency stability and are excellent time-frequency references. Their high stability facilitates a reliable communication session. This is not the case with low-cost crystal oscillators. In general, they show significant frequency fluctuations that are greatly influenced by environmental changes. There is ongoing research on isolating the oscillator circuit from the environmental impact by, e.g., oven-controlled crystal oscillators (Fig. 2.9). However, their performance is still worse than that of rubidium atomic standards, in particular at long averaging times. As a consequence, plain-crystal oscillators alone are not suited for quantum communication scenarios that have a strong demand for low timing uncertainties.
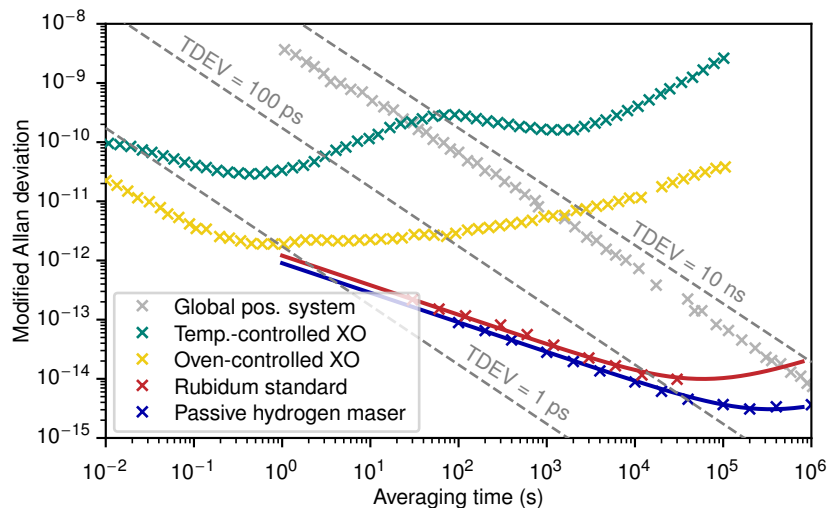
Figure 2.9 | Comparison of the timing stability of different references. Timing stability for the global positioning system [Inc20], temperature controlled crystal oscillators (XO) [Inc20] and oven-controlled XOs [Inc20]. See Fig. 2.6 for its structure. The atomic standard of rubidium [RDW21] (see Fig. 2.8**a** for its structure) and passive hydrogen masers [RDW21] reach much smaller timing deviations. The lines in the plot are a fit to the data with the analytical expression of Equation 2.13 with $\sigma_W = 1.21 \times 10^{-12}$, $\sigma_{RW} = 3.54 \times 10^{-17}$ for the rubidium standard and $\sigma_W = 9.00 \times 10^{-13}$, $\sigma_{RW} = 4.51 \times 10^{-18}$ for the passive hydrogen maser.

Crystal oscillators have some potential when introducing time-transfer technologies (Chapter

3). This can be done by using an external laser to carry the frequency reference to a remote receiver. Alternatively, single-photons can be exploited as well. They are already available in any quantum communication network at no additional cost. Using the timing of single photons, I will show that the synchronization performance increases drastically in the following. This enables the use of standard crystal oscillators in a quantum communication system, which was previously impossible.

Time-transfer techniques reduce the relative time deviation by locking slave oscillators to a common master clock in the communication network. Classical methods to transfer time with high performance could be to use external lasers [Che+21; Lia+17; Sas+11; Wan+14; Wan+21b; Yin+20] or to employ a dedicated protocol over the link for classical communication that allows high-precision time transfer, e.g. the White Rabbit Protocol [Die+16]. Alternatively, the arrival time of single photons serves as a carrier of time as well and naturally comes with a system for quantum communication. This has been shown to work very well with entangled photons in numerous publications, like [HLK09; Qua+16; VSS04] - just to name a few. Synchronization with single photons can also be achieved by using classical laser pulses that are attenuated to the single-photon level, as described in numerous other publications, e.g. [Cal+20; Cos+20; Wan+21a].

The following chapter focuses on:

1. the concept of using classical strong laser pulses for time transfer with experimental results, and

2. the motivation of using single photons to transfer time

The sections are divided first into a general part that describes the concept of time transfer (Section 3.1). In the following sections, I will motivate the use of single photons for time transfer. I will show this by comparing it to time transfer with strong classical laser pulses, including experimental results (Section 3.2). Classical laser pulses are much more resource-saving than, e.g., frequency combs, which require a complex laser and detection unit. Subsequently, I will describe the potential of time transfer with single photons (Section 3.3).

3.1 Concept

To transfer the time, we just follow three steps (Fig. 3.1**a**):

1. Derive a time signal at the sender and receiver,

2. compare the target time with actual time and return a feedback signal, and

3. use the feedback to optimize a time compensation unit.

Given the timing requirements in a general communication scenario, the performance of the method for time transfer has to be adapted to the stability of the clocks in the network.
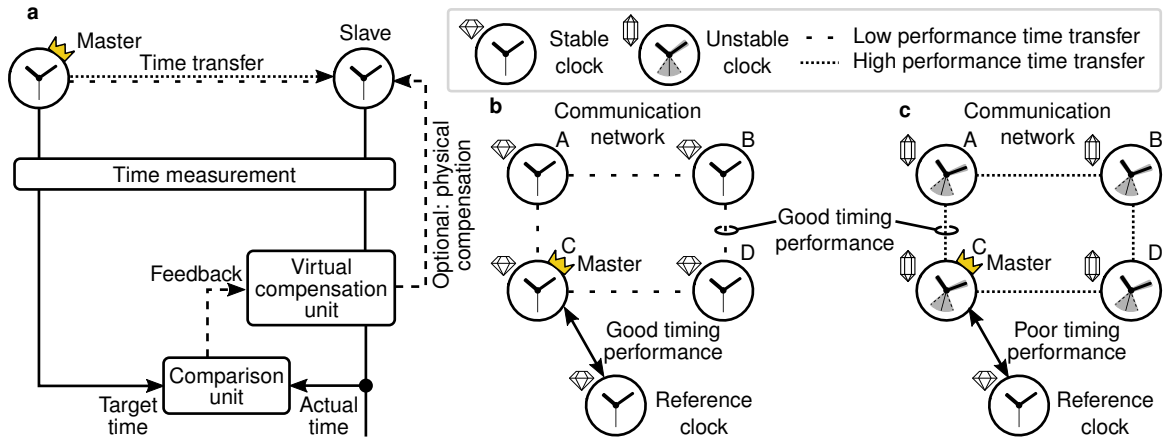
Figure 3.1 | Transfer of time in a communication network. a, The steps for time transfer consist of 1. measuring the time, 2. the comparison of the actual time from the slave oscillator with the target time from the master oscillator and 3. to compensate for the time of the slave oscillator. Note that the compensation can be performed by simply correcting the time values provided by the slave oscillator or by physically adjusting the actual oscillator (optional). **b**, Networks that incorporate highly stable and precise clocks simply require occasional time transfer through the timing of single photons. The frequency of the clocks matches closely and only the timing offset is adjusted to a common master oscillator (C). The time of the master oscillator (C) indicates small deviations with respect to an external reference clock. **c**, Crystal oscillators have a poor stability. The time deviations between the clocks are reduced by introducing time transfer with tight feedback loop times. The frequency and timing offset is adjusted to a common master oscillator (C). As the master oscillator (C) is still a quartz oscillator, the network indicates a poor *absolute* timing performance compared to an external reference clock. However, a common reference time and frequency within the network is sufficient in many cases.

When the participating parties in the network employ atomic oscillators, the frequency of the clocks is almost identical. The residual frequency difference leads to small changes in the timing offset between clocks. Any timing offset between the parties is very critical. Even 100 ps timing offsets could reduce the secure key rate to 0 bit/s in a quantum key distribution system, considering detection timing jitters of ≈100 ps. As the change in timing offset is very small with atomic references, only low-performance time transfer is required to occasionally adjust the time at the receiver (Fig. 3.1**b**). Crystal oscillators do not have an accurate frequency and change it rapidly. This behavior requires high-performance time transfer to lock the quartz oscillator frequency *and* timing offset to a common master oscillator (Fig. 3.1**c**). The master clock can also be an unstable crystal oscillator. In consequence, the time deviation within the communication network is low, but the absolute time can be far away from an external reference of high precision.

3.2 Time transfer with laser pulses

The transfer of time by pulsed laser light is straightforward and well established in the literature [Che+21; Lia+17; Sas+11; Wan+14; Wan+21b; Yin+20]. Although this section addresses only classical methods for transferring time, there are some interesting parallels to the quantum

world. The connection comes from the fact that classical laser pulses can be attenuated to the single-photon level to use them for quantum key distribution [BB14; Boa+18; LMC05; Ma+05]. In this context, particularly gain-switched laser diodes are of strong interest, as they provide a random phase [Sep+20] that ensures security [KTO14; LP07]. This motivates the following brief study of laser diodes for classical clock synchronization, as we learn about the optimization process required when they are used for quantum key distribution.

The repetition rate of the pulse train is a derivative of the clock cycle and can be transferred to a receiver. Here, this signal is used to lock the remote slave clock in an electric phase-locked loop (a PLL system). This feedback loop tunes the remote frequency to the received signal and returns the maximum gain when the master clock of the sender and the slave clock of the receiver are synchronized. Note that there is no absolute time transferred. Instead, only a frequency reference is given. Consequently, the clocks will tick with the same speed, but may have some timing offset between them. This missing absolute timing offset is detected by the communication protocol used. Moreover, it is not necessary that the frequency reference is accurate with respect to the true time. The main requirement is that the parties communicating use the same reference.

In an experimental implementation, I take simple laser diodes and pulse them by modulating the input current. The modulation is provided by a function generator with its internal clock acting as a master oscillator. The output signal from the function generator is split and electronically shared with the sender's clock. At the same time, the clock is transferred to the receiver clock through an optical channel and measured with a classical detector with 150 MHz bandwidth. A sufficient bandwidth is required to resolve the rising edge of the optical pulse. Even higher detector bandwidths do not affect the quality of the synchronization. This originates in the PLL of the slave system. It behaves as a low-pass filter for the reference input [Bes07], which is a signal with a periodicity of only 10 MHz. The optical output intensity of the laser diode can be quite complex with intensity overshooting or ripples on the intensity pattern. This influences the PLL locking system. The corresponding simulations of the optimum working point with the laser rate equations are described in the Appendix Section A.1.

The performance of this clock synchronization method is evaluated in a test bed that is required to trigger both analog-to-digital converters at the same time. In a simple setup this could be achieved by a pulse train from a function generator that is split and sent to both analog-to-digital converter. In this way, the analog-to-digital converters obtain time-correlated signals. Here, we do it a bit differently by using an analogous source of time-correlation in the quantum world: time-correlated photon pairs. This setup is significantly more complex than a function generator with a subsequent signal splitter, but it already gives the reader a taste of the application, as it is already a lab-based demonstrator for the synchronization in a quantum key distribution system.

The two time-correlated photons are generated at the same time, and the arrival time is measured at the sender (Alice) and receiver (Bob) according to the internal local clock of an
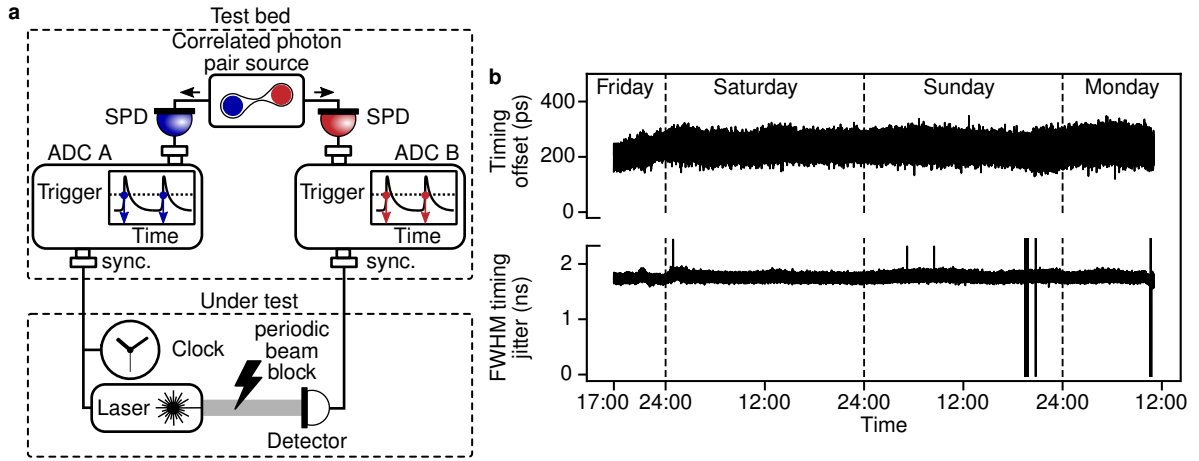
Figure 3.2 | Clock synchronization with a pulsed laser diode. a, The experimental setup to measure the synchronization performance relies on a correlated photon pair source. It is a great tool to measure the timing due to the natural timing correlations of the photon pairs. Furthermore, the setup consists of single-photon detectors (SPD) and analog-to-digital converters (ADC) that generate time tags of the arriving single photons. They have a reference channel input (sync.). The stability under a periodic beam block is evaluated in a follow-up experiment (Fig. 3.3). **b**, The synchronization performance is tested by measuring the arrival time difference between correlated photons detected with two separate clocks. The timing offset and the total timing jitter between the two clocks have been constant for several days. The full-width at half-maximum (FWHM) timing jitter is caused by the timing uncertainty of the single-photon detectors. The few drops and spikes in the timing jitter are caused by a poor processing algorithm.

analog-to-digital converter. It should be noted that the setup requires the sole measurement of the timing of the clocks, which can be complicated when using long optical fibers. Temperature fluctuations quickly lead to timing errors. This is the reason why the test bed makes sure that the use of optical fiber is reduced to a minimum. The arrival time difference of the photon pairs is recorded and processed in a histogram. The width of the histogram corresponds to the timing jitter (uncertainty of the arrival time due to the measuring devices). Furthermore, it is possible to measure the mean arrival time difference, the timing offset. The arrival-time histogram is static and will show a constant time difference between the arriving photons at Alice and Bob when the two clocks have the same frequency. However, the mean arrival time difference can change due to varying clock frequencies. In the experiment, there should be almost no frequency difference between the clocks. The reason is that both clocks at Alice and Bob are locked to the same master oscillator given by the internal clock of the function generator. At Alice, the crystal oscillator of the analog-to-digital converter is disciplined to the master oscillator of the function generator via a direct electrical connection. At Bob, the crystal oscillator is locked indirectly via an optical link. This hypothesis is confirmed in measurements over several days (Fig. 3.2). The residual timing offset change is smaller than 100 ps/hour (28 fs/s) and indicates extremely small differences in the clock frequency. In terms of timing jitter, it corresponds to 28 fs (full width at half maximum, FWHM) in 1-second integration times. This value is much lower than the timing jitters introduced by the standard 800-nm

single-photon detectors that are in the nanosecond range (here the total timing jitter is almost 2 ns). This clock synchronization method of time transfer by standard laser diodes does not contribute to the total system timing jitter and opens the application for use in state-of-the-art quantum communication systems.
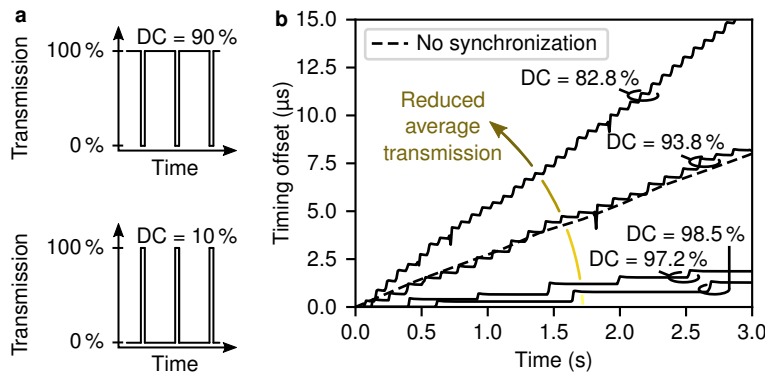

Figure 3.3 | Synchronization performance with periodic interruption of the clock signal in an emulated free-space link scenario. The timing offset of the clock is under test with the setup described in Fig. 3.2. **a**, Interpretation of the duty cycle of the beam shutter. Large duty cycles (DC), e.g. DC = 90 % refer to a large average transmission. Small duty cycles, e.g. DC = 10 % correspond to a small average transmission. **b**, When reaching a duty cycle of 6.2 %, the change in timing offset is as large as without any synchronization input (dotted line). When the clock reference is lost, the clocks start to slip and cause even higher timing offset changes than if there was no synchronization input.

Things become challenging when the optical link transmission drops to zero and no light reaches the classical detector. This could be on a free-space link (e.g. ground-to-ground, ground-to-air, ground-to-satellite) with so strong turbulence that the coupling efficiency is zero. Consequently, the external reference is lost and the slave clock starts to drift extremely with respect to the master clock. When the clocks of the analog-to-digital converters are not locked to the same external reference, the relative frequency deviation amounts to 40 ppm (datasheet). This corresponds to timing offset changes of up to 40 µs/s. With such strong changes in the timing offset, quantum communication is not possible. This originates in the low signal-to-noise ratio, which results in high error rates. In the experiment, I checked the timing offset change between the two clocks by including a beam shutter with different on/off duty cycles (Fig. 3.3**a**). As expected, the timing offset increases drastically when the light is blocked for a longer time (higher duty cycle of the shutter; see Fig. 3.3**b**). Even worse, when we reach a duty cycle ≥ 6.2 %, the timing offset change is greater than that of the quartz oscillators without external reference (here: 2.7 µs/s, which is in the range of the datasheet accuracy of 40 µs/s). At duty cycles of 19 %, the timing offset change averages out at 4.6 µs/s, being almost two times higher than if the two quartz oscillators had no external reference. This is caused by timing slips of the frequency lock to the external reference that is part of the phase-locked loop in the analog-to-digital converter (vertical steps in Figure 3.3**b**). In conclusion, the signal quality has a great impact on the synchronization performance when it is used to lock the frequencies.

The frequency lock (i.e., the 10 MHz synchronization input) of the analog-to-digital converter should not be used when strong and frequent signal fading is expected. This avoids time slips of the slave clock, as it would occur when trying to lock to the external reference. Alternatively, low-frequency (kilohertz) trigger signals could be used to periodically reset the timing offset of clocks. For example, when there is a large frequency difference of 2.7 ppm, as in our setup, the time drift after just 10 µs (clock reset trigger of 100 kHz) is only 27 ps. This means that the clock frequencies would still have a large frequency difference (here: 2.7 ppm), but the uncertainty of time does not accumulate when integrating the data, as the clock timing offset is reset periodically. I recommend such a reset mechanism instead of frequency locks for application scenarios with long-distance free-space optical links that are characterized by strong turbulences and result in large transmission fluctuations.

The described classical transfer of time requires optical powers from µW to mW and standard detectors with sufficient bandwidth to recognize optical pulses. Alternatively to such classical methods for time transfer, single-photons can be exploited as well. This is relevant in long-distance links or in scenarios where the power consumption is limited and no strong lasers can be built in. One concrete example is a down link from a microsatellites: the electrical power and space are limited, and the attenuation to the ground state is large. In such cases, it is still possible to extract valuable (timing) information and process it by using single-photon detectors.

3.3 Time transfer with single photons

The goal of single-photon time transfer is to increase the timing stability of existing clock infrastructure that otherwise would give rise to large timing jitters. Single photons can carry the master clock directly to the receiver optically and are naturally integrated into any quantum communication system. For saving resources, single-photon time transfer is of great interest.

In contrast to classical time transfer, it is necessary to work with substantially reduced optical signal, as single-photon detectors are used. One of the major challenges is the need to deal with the statistical uncertainty that depends on the number of photons used, i.e. the signal-to-noise ratio. In addition, the detectors can have several hundred picosecond timing uncertainty, which reduces the timing precision. To compare the synchronization performance to laser diode time transfer and rubidium-based synchronization, two terms play a key role here, the *accuracy* and *precision* of clocks.

Let us observe how clock synchronization works in the frequency and time domains. In the frequency domain, all we care about is the difference in frequency between clocks. The difference of the clock frequency can be described on two time scales:

1. Short time scales (seconds): there is a continuous and random change in frequency
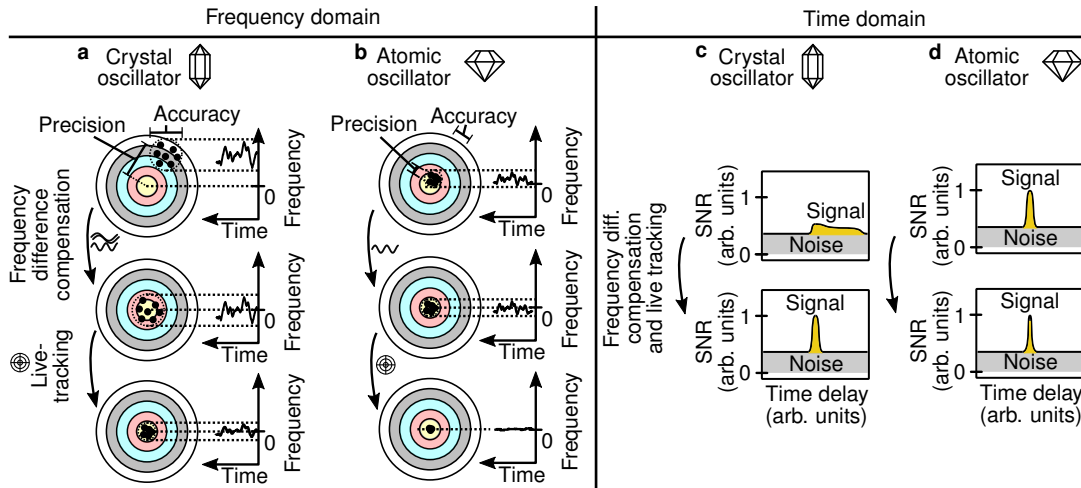
Figure 3.4 | Clock performance impacts. a,b, The frequency of imperfect real clocks differs from a nominal value and varies over time. The effect is much stronger for general oscillators (e.g. quartz oscillators, **a**) than for precise and stable references (e.g. rubidium clocks, **b**). The reduction of the frequency difference of clocks increases the accuracy, and further enhancements to the precision are made through live tracking of the clock drift (i.e., time-varying clock frequencies). **c,d**, The correlation peak with signal-to-noise ratio (SNR) in the time domain shows significant timing jitter and may even be asymmetric, because of strong frequency variation over time in crystal oscillators (**c**). The compensation of the difference in clock frequency and live tracking of the master clock frequency can reduce additional timing jitter from poor-performing clocks to a minimum. The figure is modified from my publication [5].

because of its poor stability. When picturing an archer, he hits the target with some scatter. This scatter is a signature of the *accuracy* of clocks.

2. Long time scales (days): the frequency is at a constant offset from an ideal clock. The archer hits the target off-center. This constant deviation is representative for the *precision* of clocks.

The clock synchronization protocol tackles these two time scales in a two-stage process (Fig. 3.4). First, the *precision* is increased as part of the initialization of the synchronization protocol. Second, the scatter is reduced by continuous live tracking of the difference of the clock frequency and its corresponding compensation in short intervals. This increases the *accuracy*.

By convention of the International Telecommunication Union (ITU), timing variations are split into two categories called jitter and wander. Jitter refers to rapid variations with a threshold of 10 Hz, while wander refers to slow variations less than 10 Hz [ITU00]. Consequently, the distribution of the arrival time for the 100 ms integration time (used throughout this thesis) can be considered as timing jitter. Note that any difference in clock frequency gives rise to a deterministic change of the timing that is different from the timing uncertainty of white noise. In consequence, it may be considered as wander that is present at any finite integration time. However, since this wander results in a measurable change of the timing uncertainty, I will describe its effect as an increase in the timing jitter.

Any low precision of the clocks results in a constant, but large, timing jitter. Low accuracy results in large fluctuations in timing jitter while recording several data points. This concept applies to both atomic references and crystal oscillators. The difference is that the accuracy and precision are much worse in crystal oscillators. Atomic references provide much higher intrinsic stability. The relative precision and accuracy of two such reference clocks can be further improved by the addition of single-photon or classical time-transfer methods. This increase in performance is why crystal oscillators can reach the stability of rubidium oscillators with time-transfer methods in place (Fig. 3.5). However, when time-transfer methods apply to both types of clocks, atomic references will always outperform crystal oscillators.
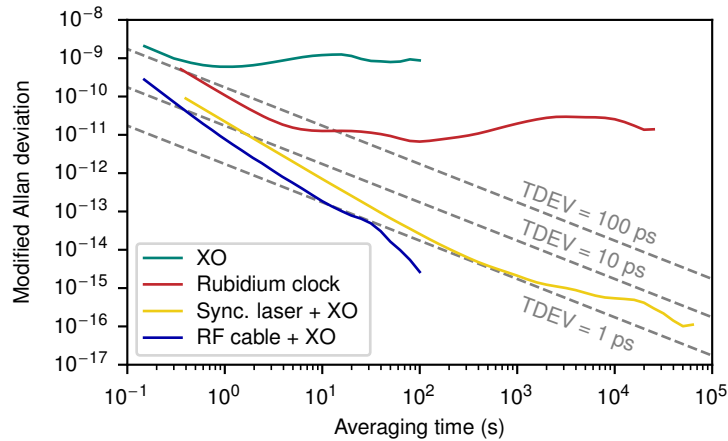

Figure 3.5 | Stability after application of various clock synchronization methods. Two independent oscillators, such as crystal oscillators (XO) or rubidium clocks, always have a worse stability than when time-transfer algorithms are in place. The transfer of time ensures that all references have a similar frequency. Such a time-transfer increases the stability and could be realized by, e.g., a synchronization laser (sync. laser) or microwave transfer (RF cable).

3.4 Conclusions

Classical time transfer techniques are built on a 10 MHz frequency carrier that allows extremely fast update times. The time transfer with single photons aims for such fast update times as well. However, the detectors already saturate at single-photon rates of a few tens of millions per second, which is the upper limit on the update time. Additionally, it is required to accumulate a sufficient number of photons to achieve a reliable and accurate measurement. These statistical uncertainties give even more restrictions. It makes an integration time necessary, which is sufficiently large and significantly reduces the update time, as I will show in this thesis.

The goal of single-photon time transfer is to increase the clock synchronization performance with standard crystal oscillators to achieve measures comparable to those of rubidium atomic references. The benefit of such crystal oscillators is that they are cost-effective and thus more scaleable; many commercial devices come with such references out of the box. I will show that it is possible to achieve similar performance by using single photons for the time transfer.

4   The synchronization protocol

The transfer of time with single photons can either enhance the synchronization performance of atomic references or enable the use of low-performance crystal oscillators, even for high-bandwidth quantum key distribution that requires timing precision in the picosecond range. The arrival time of photons greatly works for transferring time. In quantum communication networks, this is of particular benefit, as the single photons are already there to carry bits of information. This naturally leads to the main application scenario of the synchronization methods in this thesis. This chapter covers the initialization of the synchronization. The following live tracking is part of the Chapter 5. The present chapter includes several results that advance the state of the art and that are partially covered in my own publications [2; 3; 5; 6; 7]. Specifically, this chapter

1. provides a full description of the timing uncertainty for clocks with constant and varying frequency offset (Section 4.3.1),

2. discusses numerical optimizations to enhance the signal-to-noise ratio (Section 4.3.3),

3. shows how sweeps of the clock frequency enable synchronization feasibility with crystal oscillators in low-signal environments [2; 5] (Section 4.4),

4. elaborates the limitations of using asynchronous photon pair sources for clock synchronization that are driven by a continuous-wave pump [5] (Section 4.4.3), and

5. develops an optimized synchronization algorithm for pulsed (clocked) single-photon sources that leads to simple synchronization in low-signal scenarios [6] (Section 4.6).

Section 4.1 provides an overview of the single-photon synchronization workflow, while Section 4.2 describes the experimental setup used to send and detect single photons. After registering the arrival time of a single photon, it follows the initial numerical processing steps (Section 4.3). The same processing steps are also used in the subsequent algorithm for frequency search (Section 4.4), where a comparison with the relevant literature is provided. Finally, in Section 4.6, synchronization methods with clocked single-photon sources are discussed, compared to asynchronous sources, and placed in the context of the literature. (Section 4.6).

4.1 Overview

The synchronization workflow with single photons starts by processing the high-resolution arrival times of the photons by sorting them into time bins (Fig. 4.1). Subsequently, the arrival

times of the two parties are cross-correlated to find the timing offset between the two parties. This timing offset of the clocks is identified by a strong a significant signal peak in the cross-correlation function. In other words, the quantum signal allows us to take a measurement of the clock status between two parties in the network. The next step includes the application of the cross-correlation algorithms to match the clock frequency first (increases the precision) and then to find the timing offset between the clocks subsequently. At this point, the initialization of the synchronization is complete, and the live communication session begins. During the communication session, the algorithms track the frequency difference and correct the time of one party to match it with the other. When following these steps, high timing stability and low synchronization timing jitters will be achieved. This ensures high data rates during a potential quantum communication session or high-precision measurements in metrology.
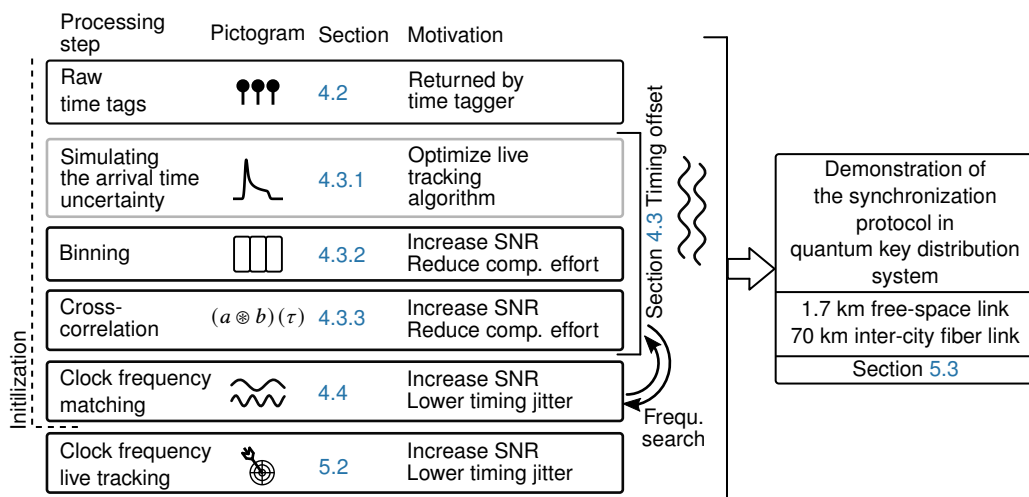

Figure 4.1 | Clock synchronization work flow. First, the algorithm processes the time tags from the analog-to-digital converter (Section 4.2) by binning them (Section 4.3.2). This section also includes simulations of the arrival time uncertainty (Section 4.3.1) that is not included in the synchronization work flow (greyed out). Cross-correlations allow matching of the clock frequencies (Section 4.3.3). As soon as the clock frequencies match (Section 4.4), the uncertainty of timing is reduced. This provides a correct timing offset between the clocks as the last step during the initialization of the synchronization. The following tracking method compensates for any frequency difference between unstable oscillators that arises during a communication (Section 5.2). The last step is to test the robustness in real link scenarios and deployed links (Section 5.3).

4.2 Experimental setup

Every component in the experimental setup has its own timing uncertainty and affects the final synchronization performance to some extent. In general terms, there are four main contributions of the total timing error. These are (Fig. 4.2):
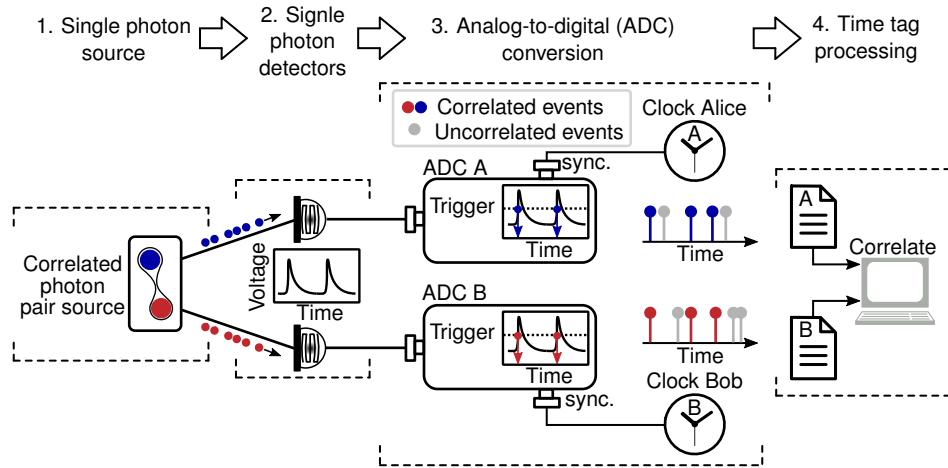
Figure 4.2 | Experimental setup for single-photon detection and processing. Pairs of time-correlated single photons are generated from a source first. Subsequently, single-photon detectors generate voltage spikes that trigger an analog-to-digital converter (ADC) when reaching a voltage threshold. The ADCs provide time tags according to its internal clock. They are stored in files and processed (correlated) on a computer.

1. the *single-photon source* (uncertainty in the emission of the single photon),

2. the *single-photon detectors* (uncertainty between the single-photon arrival time and the generation of an electrical signal),

3. the *analog-to-digital converters* (uncertainty between the generation of a time stamp and the arriving electrical signal) and

4. the time stamp *processing unit* (introduces timing uncertainty due to poor synchronization).

The sender is responsible for the first contribution, while the remaining is part of the receiver.

The sender The *single-photon source* of the sender can be either an entangled photon pair source or a faint pulse source. An entangled photon source generates photon pairs, for example via the non-linear process of parametric downconversion. When the optical power of the laser driving the process is low enough, non-classical bi-photon states are created. On the other hand, *approximations of single photons* in faint pulse sources are generated by attenuating macroscopic (and strong) laser pulses to the single-photon level. Generally speaking, light is a coherent state with a Poissonian photon number distribution [FF+06a]. That means that there is always some probability to find multiple photons for any given integration time. However, throughout this thesis, I will still call this type of sources "single-photon source" under the assumption of a low mean photon number that gives multiple photons with only low probability. One significant property is that the emission of single photons is only possible in a time window that is bound by the envelope of the classical laser pulse (that is attenuated). On the other hand, entangled photon sources that are driven by continuous-wave lasers have a random emission

time of the photons. In the special case of a pulsed drive, this changes to a more deterministic timing behavior. Such deterministic timing behavior by using pulses is particularly useful for clock synchronization and leads to higher noise resistance during the initialization of the synchronization, as I will show later (Section 4.6).
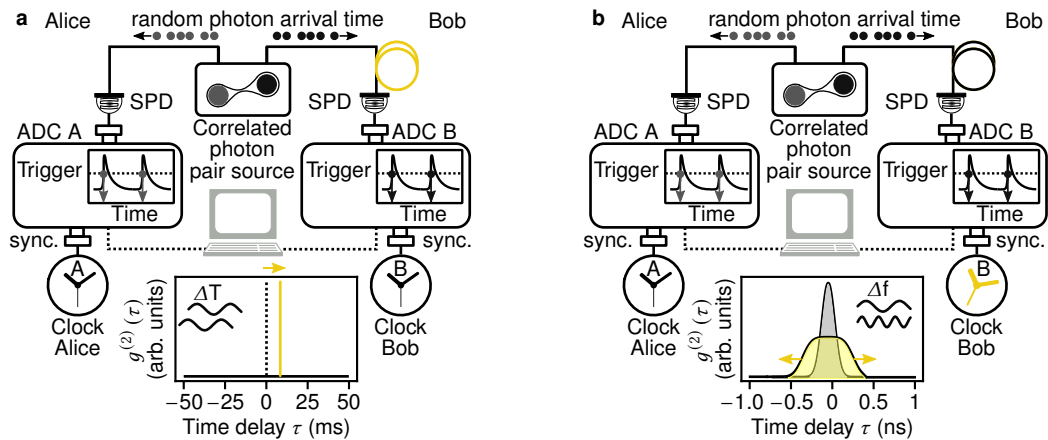

Figure 4.3 | Impact on the arrival time histogram for a frequency or timing offset difference. a, Length differences in radio frequency (RF) cables or additional optical fiber result in a asymmetry of the path length of the two transmitted photons. This gives rise to a timing offset and the histogram is shifted in time. **b**, The frequency difference of the clocks is observed by an increased uncertainty of the arrival time difference of the measured photons. The histogram of the arrival time differences is increased in width.

The receiver   The generated single photons are routed to the receiver, where they are detected by *single-photon detectors* (SPD). On arrival, they create sharp voltage spikes in an avalanche effect in standard SPDs [Had09]. Alternatively, single photons break the superconductivity in superconducting nanowire single photon detectors (SNSPD), and the resulting current is amplified by electronics [Qua22]. The detectors show a timing jitter between the creation of the voltage pulse and incident single photons. Subsequently, the voltage pulses are guided to *analog-to-digital converters* (time taggers), which provide time stamps according to their internal clock [Bec05]. A computer reads the time tags and stores them in files. The next step is to process the time tags in a *processing unit* by calculating the time difference between the two received photons (entangled photon source) or the time that a photon has been sent and received (faint pulse source). Time differences accumulate over an integration time and are displayed in a histogram. Two things can be observed in the histogram (Fig. 4.3):

1. a constant timing offset that comes from the run-time difference, for example, additional fiber or length differences of the radio frequency (RF) cables between the detectors and the analog-to-digital converters.

2. an increased timing jitter that originates from the clocks showing a frequency difference.

For successful clock synchronization, both timing offset and frequency must be compensated for. This will be covered in the following sections.

4.3 Detecting the timing offset

The timing offset and the clock frequency have interdependencies that increase the effort to find both. The difference in clock frequency y leads to an increasing offset ΔT between the two clocks after time t,

$$\Delta T = yt. \tag{4.1}$$

Tracking the offset over time is one option to determine the frequency difference y. However, when the frequency difference is large, the resulting timing uncertainty can be substantial, particularly after long integration times. Crystal oscillators are a great example and exhibit a frequency offset of more than 2 ppm (as shown in Table 2.2). The concrete timing statistics are derived in the next Section 4.3.1. Moreover, when the correlation peak is spread over time, it leads to a decrease in the peak signal-to-noise ratio. This makes it difficult or even impossible to accurately identify the true timing offset. As a result, it is also not possible to derive the clock frequency. This is a typical chicken-or-egg problem that I solve by varying the frequency of one clock and each time performing a cross-correlation. When the frequency is close to the other clock, a significant correlation peak will appear. The method of varying the frequency is covered in the next Section 4.4. In this section, I describe the timing statistics and optimization of the cross-correlation algorithms that are later used to match the clock frequencies.

In all the following sections, I will focus on the general case of an asynchronous source. Clocked sources require a slight modification of the approach. The specific differences between clocked and asynchronous approaches will be discussed in the last Section 4.6 of this chapter.

4.3.1 Modelling the timing statistics

To gain a better understanding of the challenges involved in determining the offset, I will present a simple model that takes into account various experimental noise sources. By studying the impact of noise on the arrival-time histogram, I will quantify its effect on the experimental timing uncertainty. While single-photon sources, single-photon detectors, or time-to-digital converters introduce Gaussian random white noise, poor clock synchronization introduces non-Gaussian noise. The difference in arrival time between 2 photons is described by Gaussian functions with the root mean square (RMS) timing jitter σ_0. The timing jitter of Gaussian white noise adds up to

$$\sigma_0^2 = 2\sigma_{\text{SPD}}^2 + 2\sigma_{\text{ADC}}^2 + \sigma_{\text{SPS}}^2, \tag{4.2}$$

with the timing jitter from the two single-photon detectors σ_{SPD}, two time-to-digital converters σ_{ADC} and the single-photon source σ_{SPS}. The total timing uncertainty under poor clock synchronization is not described that easily. When there is a difference in clock frequency, total

timing statistics can be derived as a sum of Gaussian functions that are maximally shifted by an offset ΔT. This is the result of the difference in the clock frequency y and the integration time t (Equation 4.1). The probability density distribution $\left(\int_{-\infty}^{\infty} g^{(2)}(\tau)d\tau = 1\right)$ for a constant difference in clock frequency $g_{\text{const.}}^{(2)}$ is (Fig. 4.4(a)),

$$g_{\text{const.}}^{(2)}(\tau, \Delta T) = \frac{1}{N}\sum_{i=0}^{N}\frac{1}{\sqrt{2\pi\sigma_0^2}}\exp\left[\frac{-(\tau - i/N \times \Delta T + \Delta T/2)^2}{2\sigma_0}\right], \tag{4.3}$$

whereby $g^{(2)}(\tau)$ (τ is the time delay or the time difference) corresponds to the distribution of the difference in arrival time between 2 photons. This sum can be described analytically through the error function

$$\text{erf}(z) = \frac{2}{\sqrt{\pi}}\int_0^z e^{-x^2}dx, \tag{4.4}$$

$$g_{\text{const.}}^{(2)}(\tau, \Delta T) = \frac{1}{2\Delta T}\left[\text{erf}\left(\frac{\tau + \Delta T/2}{\sqrt{2}\sigma_0}\right) - \text{erf}\left(\frac{\tau - \Delta T/2}{\sqrt{2}\sigma_0}\right)\right]. \tag{4.5}$$

This outcome can also be generalized to an arbitrary change in timing offset as in clocks with varying frequencies. As an example, let us assume an accelerating clock with acceleration a that introduces a timing offset ΔT,

$$\Delta T(t) = \frac{a}{2}t^2. \tag{4.6}$$

Physically, clock acceleration refers to a continuous increase or decrease in clock frequency (RW FM noise or white FM in the noise model in Section 2.3). In particular, the RW FM noise becomes more apparent for longer integration times and results in clear asymmetries experimentally. The numerical representation of it is a sum of probability density functions with a constant difference in clock frequency $g_{\text{const.}}^{(2)}$, but with varied timing offsets ΔT,

$$g_{\text{acc.}}^{(2)}(\tau, a, t) = \frac{1}{N}\sum_{i=0}^{N}g_{\text{const.}}^{(2)}\left[\tau - \frac{a}{2}t_i^2, \frac{a}{2}\left(t_i^2 - t_{i-1}^2\right)\right]. \tag{4.7}$$

The function indicates a clear asymmetric behavior (Fig. 4.4**b**), as the introduced timing offset increases over time (Equation 4.6).

The FWHM timing jitter δ_{FWHM} for a constant frequency difference is found at half the maximum of Equation 4.5. After normalization, this gives,

$$\frac{1}{2} = \frac{1}{\text{erf}\left(\frac{\Delta T/2}{\sqrt{2}\sigma_0}\right)}\left[\text{erf}\left(\frac{\delta_{\text{FWHM}}/2 + \Delta T/2}{\sqrt{2}\sigma_0}\right) - \text{erf}\left(\frac{\delta_{\text{FWHM}}/2 - \Delta T/2}{\sqrt{2}\sigma_0}\right)\right]. \tag{4.8}$$

Note that the root mean square timing jitter with the variable σ is not suitable, as the timing distribution is no longer Gaussian. Instead, I introduce the full width at half-maximum that will reserve the variable "δ_{FWHM}" as a clear distinction to the RMS-width. The total timing
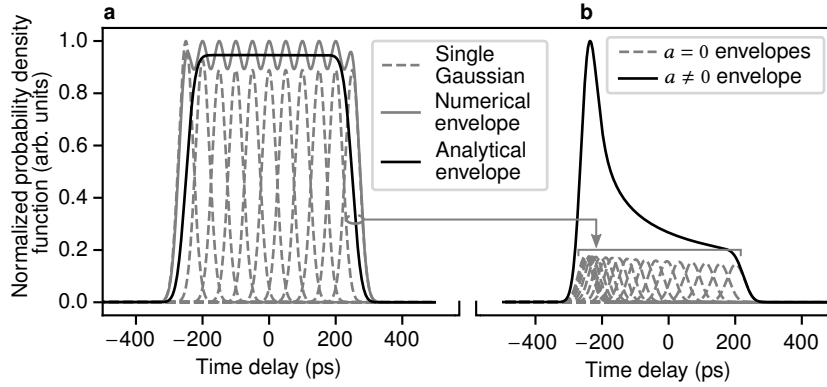
Figure 4.4 | Statistical distribution of the measured arrival time of photons for clocks indicating constant and varying frequency differences. a, Distribution for $N = 10$ Gaussian functions with each timing jitter being $\delta_{\mathrm{FWHM}} = 50\,\mathrm{ps}$. For illustration purposes, I selected a (too) small number of N for a clear distinction between the numerical model (with ripples, Equation 4.3) and the analytical model (without ripples, Equation 4.5). The total shift due to the difference in clock frequency is set to $\Delta T = 500\,\mathrm{ps}$. **b**, Simulation of an accelerated clock with acceleration $a = 1000\,\mathrm{ps/s^2}$ (a few hundred of $\mathrm{ps/s^2}$ are typical for crystal oscillators). Note that real clocks do not have a constant acceleration, as assumed here. The total integration time t is $1\,\mathrm{s}$ with 20 time steps (20 Gaussian functions corresponding to Equation 4.5) with the timing offset caused by the clock acceleration, $\Delta T = a/2 \times t^2$. Note how the peak value of every individual Gaussian becomes smaller as it stretches more.

jitter δ_{FWHM} can be easily estimated in a region $\Delta T/2 \gg \sqrt{2\log(2)}\sigma_0$ (Fig. 4.5**a**),

$$\delta^2_{\mathrm{FWHM}, \Delta T/2 \gg \sqrt{2\log(2)}\sigma_0} = (2\sqrt{2\log(2)}\sigma_0)^2 + \Delta T^2, \tag{4.9}$$

Intuitively, this can be simplified to $\delta_{\mathrm{FWHM}} \approx \Delta T$. However, the trend is quite complex for $\Delta T/2 \gtrapprox \sqrt{2\log(2)}\sigma_0$ (Fig. 4.5**b**). The total timing distribution is a mixture of the original Gaussian function with a linear stretch. Anyway, there is another simple expression for the region $\Delta T/2 < \sqrt{2\log(2)}\sigma_0$ (Fig. 4.5**c**),

$$\delta^2_{\mathrm{FWHM}, /2 < \sqrt{2\log(2)}\sigma_0} = (2\sqrt{2\log(2)}\sigma_0)^2 + \Delta T^2/2, \tag{4.10}$$

with the FWHM timing jitter due to the clock instability (the synchronization timing jitter) being,

$$\delta^2_{\mathrm{FWHM,\ clock}} = \Delta T^2/2. \tag{4.11}$$

Sometimes it is hard to find the exact timing distribution in an experiment, especially when it is deformed and there are just few photons that could describe the statistics. In such cases, a simple Gaussian fit with its root mean squared jitter σ_{RMS} may be applied. Note, however, that this means that a standard Gaussian is fitted to a super-Gaussian timing distribution for large differences in clock frequency $\Delta T/2 \gg \sqrt{2\log(2)}\sigma_0$. Another side note: the distribution is only super-Gaussian (symmetrical) in the case of a constant frequency difference. When the frequency varies, the distribution is asymmetric and no longer fits into the super-Gaussian group. Such a Gaussian fit to (here) a super-Gaussian function has the consequence that the fit
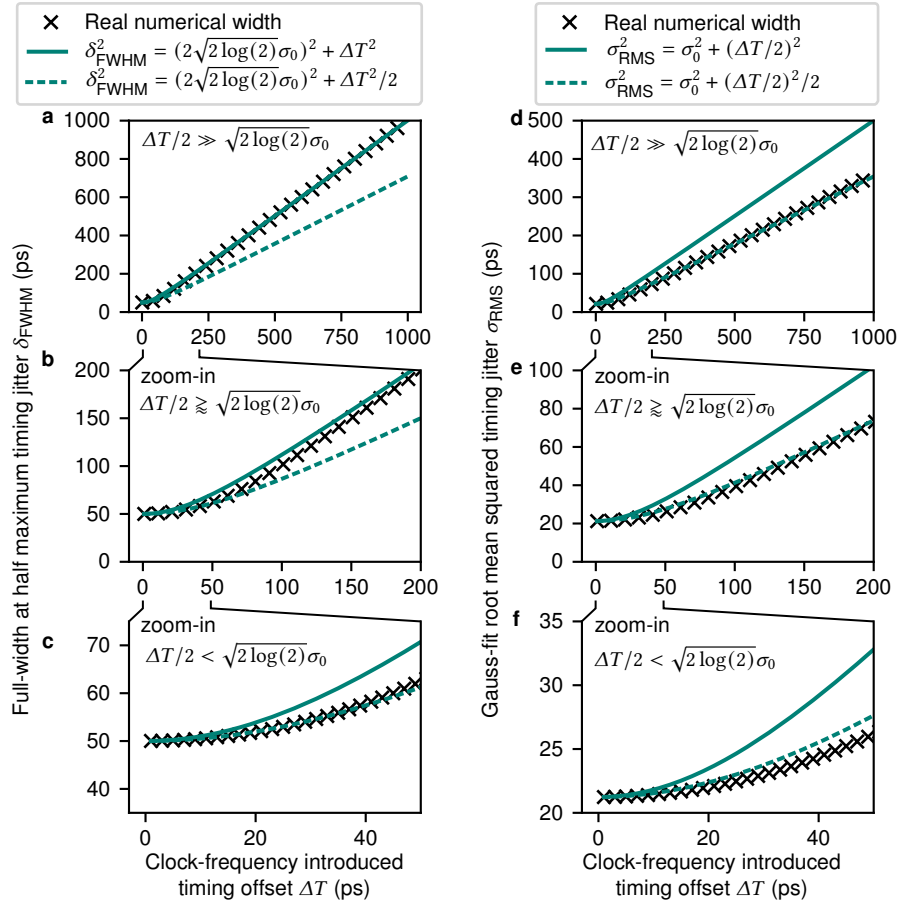
Figure 4.5 | Total timing jitters for varying timing offsets ΔT that have been introduced by a given clock frequency deviation (Equation 4.1). The real trend is calculated from Equation 4.5. **a-c**, Full-width at half maximum timing jitter of the real timing distribution. **d-f**, Root-mean squared (RMS) timing jitter of a Gaussian fit to the real timing distribution. **a**, When the clock-introduced timing offset ΔT is much larger than the original RMS timing jitter σ_0 ($\Delta T/2 \gg \sqrt{2\log(2)}\sigma_0$), then the total timing jitter follows the trend $\delta_{\text{FWHM}}^2 = (\sqrt{2\log(2)}\sigma_0)^2 + \Delta T^2$. **b**, There is not a very good matching trend for the intermediate region of timing offsets ΔT. **c**, When $\Delta T/2 < \sqrt{2\log(2)}\sigma_0$, then the total timing jitter is $\delta_{\text{FWHM}}^2 = (\sqrt{2\log(2)}\sigma_0)^2 + \Delta T^2/2$. **d-f**, For all ranges of ΔT, the analytical trend $\sigma_{\text{RMS}}^2 = (\sigma_0)^2 + (\Delta T/2)^2/2$ corresponds well to the real evolution, except for small ΔT (**f**).

has a smaller width than the actual timing distribution. To be more precise, the impact on the total RMS jitter σ_{RMS} from the clock frequency is reduced by a factor $1/\sqrt{2}$ (Fig. 4.5**d-f**),

$$\sigma_{\text{RMS}}^2 = (\sigma_0)^2 + (\Delta T/2)^2/2, \tag{4.12}$$

with the RMS timing jitter due to the clock instability (the synchronization timing jitter) being

$$\sigma_{\text{RMS,clock}}^2 = (\Delta T/2)^2/2. \tag{4.13}$$

An increase in timing jitter reduces the maximum value of the statistical distribution. This reduces the signal-to-noise ratio. The area of the timing distribution A is the sum of the area of several Gaussian functions, each with an area of $\sqrt{2\pi\sigma_0}$,

$$A = \sqrt{2\pi\left(\sigma_0^2 + k\Delta T^2\right)}, \qquad (4.14)$$

with $k = 1$, if the timing distribution was estimated as the real super-Gaussian and $k = 1/2$, if the timing distribution was estimated and fit by a Gaussian. The initial Gaussian peak P_0 with area $A_0 = \sqrt{2\pi\sigma_0^2}$ reduces to P as the synchronization jitter increases,

$$P = P_0 \frac{1}{\sqrt{1 + \dfrac{k\Delta T^2}{2\pi\sigma_0^2}}}. \qquad (4.15)$$

I use this timing jitter model for all future experimental investigations. In particular, I describe the experimentally introduced timing jitter from the change of the timing offset. This gives a clear performance parameter, the synchronization timing jitter, which can be differentiated from the other Gaussian white noise timing jitters that come from single-photon sources, single-photon detectors, and analog-to-digital converters.

With these theoretical descriptions at hand, I return to obtaining the *experimental* timing distribution. I obtain it after a few processing steps of the single-photon arrival time - this starts with the binning of the arrival times in the next Subsection 4.3.2.

4.3.2 Binning of the single-photon arrival information

The first step after reading the photon arrival times from the analog-to-digital converter is to sort them into time slots (binning) to increase the efficiency of the following processing steps (Fig. 4.6**a,b**). The digital resolution of the photon arrival times is given by the analog-to-digital converter (here it is 1 ps). This is different from the actual RMS timing resolution, which is around 2.0 to 2.4 ps in state-of-the-art systems [Gmb22; Ins22]. The main concept is to select a width of the time bin that matches the total timing jitter of the systems to maximize the signal-to-noise ratio (Fig. 4.6**c**).

Note that we also must be careful with the computation time, which increases with smaller bin widths. Let us take the example of collecting time tags over 100 ms with a digital resolution of 1 ps. Without further notice, the default integration time is 100 ms in this thesis, as it will allow fast update times and sufficiently good statistics. The array size is 1E+11 before binning. On the other hand, when introducing bins of width 10 ns, the array size is only 10^7, significantly reducing the computation time. Selecting the correct bin width might be a nice theoretical idea and makes sense for known timing jitters, such as those from the time taggers or the single-photon detectors. However, the clock frequency changes continuously and is often unknown. Therefore, it is impossible to know the real timing jitter in the first place. Therefore, the signal-to-noise ratio in real life will always be smaller than theoretically given. More on this follows in the next section, where the time stamps between the two parties are correlated.
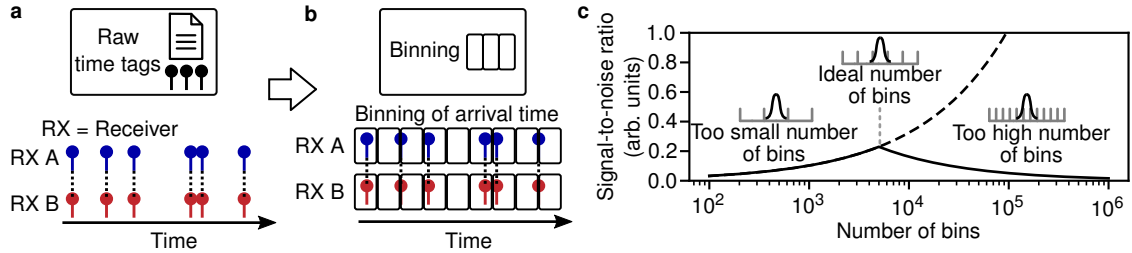
The protocol for time transfer with single photons

Figure 4.6 | From the time stamps to the bins and the increase of the signal-to-noise ratio by selecting the right bin width. a, The analog-to-digital converter provides raw time stamps from receivers A and B with digital resolution 1 ps. **b**, Bins are introduced to reduce the size of the array to minimize computation time. At an integration time of 100 ms, the array size for the digital resolution of 1 ps is 10^{11}. When introducing bins of width 10 ns, the size of the array is only 10^7. This reduces the computation time substantially. **c**, The figure represents the number of bins N for a given time window. The time window is equal to the integration time t, which is 100 ms. When selecting a bin width $\delta t = t/N$ equal to the total timing jitter, the signal-to-noise ratio is maximized. Smaller or larger bin widths reduce the signal-to-noise ratio. The figure is taken from my publication [5].

4.3.3 Cross-correlating the timing information

The synchronization protocol uses a two-stage process to find the timing offset. The first step is a coarse search of the timing offset (Fig. 4.7). This phase is particularly critical for clocks with large frequency differences and links with low signal, leading to a high probability of failure. The second step continues with fine-tuning the timing offset by a modified algorithm. Let us start with the coarse search for the timing offset. To this end, the communicating parties group their time stamps in bins, resulting in an array of size N at each party. After cross-correlating the two arrays, it provides an average time difference between the photon arrival times. Each time bin that is filled with a photon arrival time can be represented by a delta function. It is very unlikely that several photons fall into the same bin. This is easy to derive when considering a photon count rate of 10^6 counts/s that can be close to the saturation level of nanowire single-photon detectors [Qua22]. Given a typical array size of 10^7 and the integration time of 100 ms, the array is only filled up to 1 %. If the unlikely event of two photons in the same bin nevertheless occurs, it is still treated as one photon, and the delta comb is left unaffected. Consequently, receiver A may represent the arrival times t_i with a delta comb $a(t)$,

$$a(t) = \sum_i \delta(t - t_i), \tag{4.16}$$

and the receiver B represents the arrival times of photons t_j with delta comb $b(t)$,

$$b(t) = \sum_j \delta(t - t_j). \tag{4.17}$$

The delta combs are created for an integration time of 100 ms (by default in this thesis). When the two combs are cross-correlated, a correlation peak appears for a specific time delay $\tau = [0, 100\,\text{ms}]$ between the arrays,
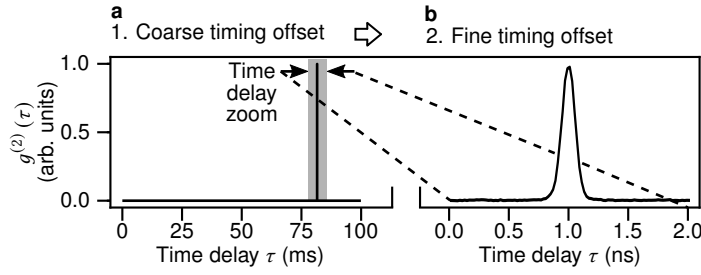
Figure 4.7 | Two-stage process to find the timing offset. a, First, the algorithm selects a large bin size to search over a large window (integration time is 100 ms here) for the correlation feature with Fourier-based cross-correlations (Equation 4.19). This search is particularly challenging during the initialization of the synchronization, as the peak may disappear for significant differences in clock frequency. In such cases, the clock frequency search algorithm is required. **b**, After finding the correlation peak within the integration time, the exact timing offset is derived over a smaller observation window (here: 2 ns). The start-stop cross-correlation algorithm is applied here to reduce computational effort.

$$g^{(2)}(\tau) = \int_0^{100\,\text{ms}} a(t)b(t-\tau)dt. \tag{4.18}$$

The same can be represented by Fourier transformations $\mathcal{F}$ (and inverse Fourier transformations $\mathcal{F}^{-1}$) which have much better performance for array sizes $\geq 10^5$ in the Python function NumPy [Har+20],

$$g^{(2)}(\tau) = \mathcal{F}^{-1}\left[\mathcal{F}(a(t))^*\mathcal{F}(b(t))\right]. \tag{4.19}$$

The frequency spectrum of the time tag stream $\mathcal{F}(a, b(t))$ is flat, interestingly, and similar to a frequency spectrum of white noise with equal intensity at all frequencies. This comes from the fact that the creation time of the photons is random and originates from a spontaneous process. On the one hand, this feature has some valuable application in, e.g., quantum key distribution, where randomness is used to extract more information from a single photon [Zho+15].

The parameter for characterizing the signal-to-noise ratio of the correlation peak is called significance. It is used in the search for the coarse timing offset. It represents the relationship between the peak value and the standard deviation of the background (see Fig. 4.8). If the significance is 2, then the peak is the true correlation peak with a confidence of 95 %. For a significance of 3, the confidence of the peak increases to 99.7 %. Finding the correlation peak under a noisy background is particularly challenging during the initialization of the synchronization session. Therefore, the significance parameter serves as a useful indicator of the reliability with which the peak position can be identified. The threshold for identifying the correlation peak is set to 7, as introduced in the literature [HLK09]. Although the selection of higher thresholds gives even higher confidence, this can be a drawback in scenarios with low signal-to-noise ratios, as synchronization would not be possible. The significance of 7 (or maybe even a bit lower) is a compromise between some probability of a failure of the
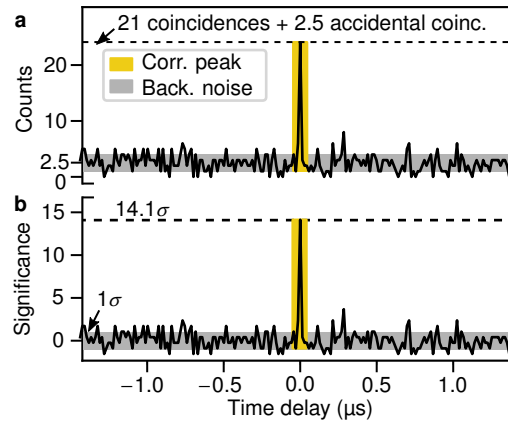
Figure 4.8 | Significance of correlation features. a, After cross-correlation, there is a correlation peak with 21 counts (coincidences) and background noise with a mean value of 2.5 counts (accidental coincidences). The background noise has a standard deviation of 1σ (gray shaded region). **b**, The significance refers to normalization to the standard deviation of the background. Therefore, the correlation peak is represented by 14.1 standard deviations of the background. The small amplitude of the background may lead to the false conclusion that the noise *maxima* (they are what is relevant) are small. However, the figure only shows a small time window of $3\,\mu s$, although the actual window is as large as the integration time (100 ms). In reality, there is some statistical probability that the noise will reach a significance of 5 or even higher; it is just unlikely.

synchronization and the establishment of synchronization under low signal-to-noise ratios. In such lossy scenarios, it is useful to select smaller thresholds to still have the opportunity to initialize the protocol. However, this also means that the probability of failure increases and that the protocol may have to restart when the actual correlation peak from the signal is not found.

When the timing offset between clocks is sufficiently small, a start-stop method [All+04; Bru+99; Mar+16] can be applied instead of a Fourier-based approach. This is much faster, as *only* neighboring time tags are considered, and none further apart (Fig. 4.9). In the Fourier-based method, every time of the Nth received photon at Alice is compared with all M^{th} received photons at Bob. When the shorter array is zero-padded, the array size is $n = \max(N, M)$. This gives rise to a computational complexity of $O(n^2)$ for a standard Fourier transformation and $O(n \log_2 n)$ for the fast Fourier transformation [CLW67]. On the other hand, the start-stop algorithm reduces the complexity to only the size of the array n with computational cost $O(n)$. This comes from the fact that only n time differences are calculated, which is just a $O(1)$ operation.

Time tags are considered as neighbors from time perspective after listing the arrival times of photons from receiver A and B in the same array ascendingly. This method applies when the coarse timing offset is found. As only neighboring time tags are considered, this method does not work when the timing offset is not calculated with high enough precision. To be more concrete: the precision of the timing offset must be higher than average time between photon counts. If this is not the case, the start-stop method would no longer correlate the photons
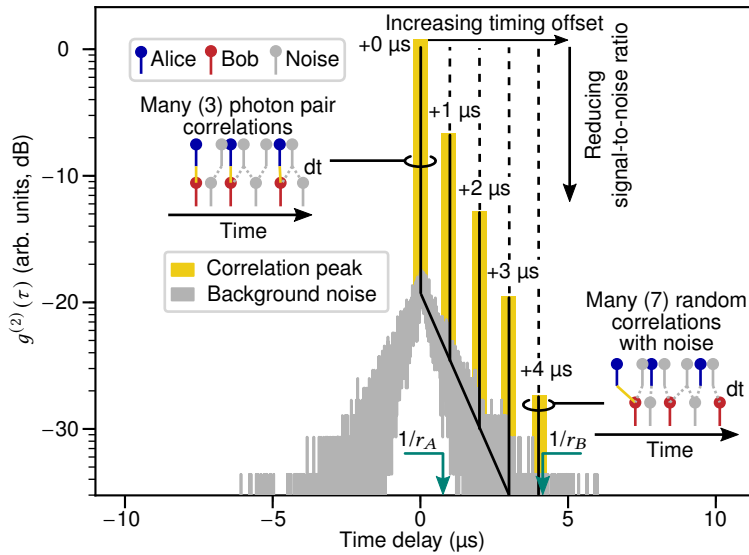
Figure 4.9 | Creating start-stop cross-correlations. When the timing offset is determined with high precision $\leq 1\,\mu s$, there are many photon pair correlations (correct correlations indicated by yellow colored lines in the inset with the time tags) detected and the signal-to-noise ratio of the correlation peak $g^{(2)}(\tau)$ is maximum. On the other hand, when the timing offset is detected with a larger uncertainty (here: $1\,\mu s$, $2\,\mu s$, $3\,\mu s$, $4\,\mu s$), the signal-to-noise ratio is reduced because there are many accidental correlations with noise (gray lines in the inset with the time tags). This becomes worse the closer the uncertainty is to the inverse single-photon detection rate from Alice and Bob $r_{A,B}$. The number of (measured) deterministic correlations from the photon pair decreases as the probability increases to find correlations with noise that comes from the single events. This reduced signal-to-noise ratio is the reason Fourier-based cross-correlations are required to find the initial (coarse) timing offset. They do not show the effect of a smaller signal-to-noise ratio for large timing offsets, as all time tags are correlated with each other, and not just the timely neighbors. The figure is modified from my publication [5].

with their actual true neighbor (the other correlated photon at receiver B). Instead, larger uncertainties of the timing offset continuously increase the number of correlations with noise. This drastically reduces the signal-to-noise ratio. As an example, if there is an average count rate of 10^6 counts/s, then the average time difference of the detection events is $1\,\mu s$. Therefore, it is also necessary to determine the (coarse) timing offset with resolution $\leq 1\,\mu s$. When transferring this requirement to the binning for the Fourier-based cross-correlations, the bin size, i.e. the precision, should be $\leq 1\,\mu s$. Generally speaking, the higher the single-photon rate, the higher the timing precision. This fact has a substantial consequence on the computation effort, as higher precision necessarily comes with longer computation time. Taking the example of quantum key distribution, high single-photon rates are desired, as this increases the secure key rate. Likewise, it drastically increases the requirements on the synchronization chain at the cost of the computation time, from the first network ping over the Fourier-based cross-correlation to the start-stop method. With the basics of cross-correlations at hand, we can optimize its performance next.

Characterization and optimization of the performance

The goal of the initialization procedure is to locate the peak of the correlation function, i.e. the timing offset between the detection of photons in the presence of noise. By that, it is possible to find the timing offset and the clock frequencies. In other words, the challenge in the *initialization of synchronization* is to increase the statistical significance of the correlation peak with respect to noise, i.e., the signal-to-noise ratio. Three factors have a major impact on this:

1. the binning (number of bins and offset of bins)

2. the *precision* of clocks that affects the initial timing uncertainty and

3. the number of correlations from the source (communication links over large distances usually indicate low signal)

In the following paragraphs, I will elaborate on these individual contributions in more detail and show how to minimize the impact of each of them on the signal-to-noise ratio.
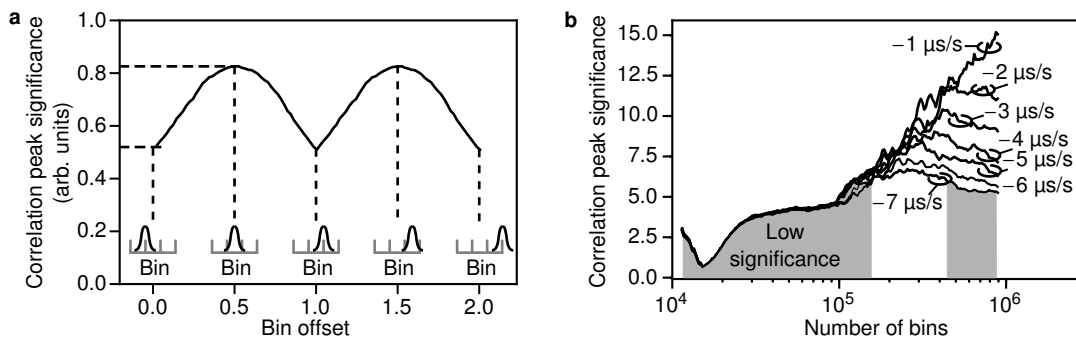

Figure 4.10 | Impact of bin offset and difference of the clock frequency on the significance of the correlation peak. a, When the correlation peak is centered over one bin, this gives the highest significance. This effect is stronger when the bin size is equal to the timing jitter. **b**, The significance of the correlation peak for a varying difference in the clock frequency -1 to -7 ppm. Smaller differences of the clock frequency increase the significance under the constraint that the bin size matches the timing jitter. A too large number of bins (too small bin sizes) again reduces the significance, as the signal is distributed over several bins. Regions with significance ≤ 7 are shaded in gray color.

Binning and the precision of clocks   The analytical significance of correlation features can be described by the number of bins, their offset, and the difference in clock frequency. Let us imagine that the true correlation rate (excluding noise) from the single-photon source is r_C. The number of correlations during acquisition time t is $r_C t$. The total single photon rate at receiver A is r_A and receiver B is r_B. Assuming Poisson statistics for the single-photon source, the uncertainty of the noise count rate (standard deviation) is $\sqrt{r_A r_B t^2}$ for the total number of events being $r_A r_B t^2$. This total noise is distributed over N bins that are used later for the cross-correlation. The significance S is defined by the number of correlations divided by the standard deviation of background noise [HLK09],

$$S_{(y\times N)=1} = \frac{r_C t}{\sqrt{r_A r_B t^2 / N}} = \frac{r_C}{\sqrt{r_A r_B / N}}.$$ (4.20)

However, I will modify the equation from [HLK09], since this is only the case where the bin size $\delta t = t/N$ is equal to the timing jitter introduced by the difference of the clock frequency $\delta_{\mathrm{FWHM}} \approx yt$ (Equation 4.9, note that this approximation is only valid for significant differences in clock frequency). When the size of the bin is too small, the signal r_C is distributed over $\delta_{\mathrm{FWHM}}/\delta t = yN$ bins,

$$S_{(y\times N)\geq 1} = \frac{1}{yN} \frac{r_C}{\sqrt{r_A r_B / N}}.$$ (4.21)

Furthermore, even if the bin size perfectly matches the timing jitter, the bins may have some relative time offset with respect to the timing distribution (Fig. 4.10**a**). In the worst case, the signal would be distributed equally across two bins. This reduces the signal by 50 %. The relative effect is much worse when the bin size is selected right. As an example, imagine the correlation peak to be a distribution over 10 bins. For an offset of half the bin size (worse case), the correlation peak would be distributed over 11 bins. This reduces the signal by only 10 %. On the contrary, when the correlation peak lies in one bin, an offset of half the bin size reduces the signal by 50 %. This means that, when optimizing the bin size to match the width of the correlation peak, one more substantial optimization parameter is the binning offset. On the other hand, when the bin size is not optimized, e.g., it is much too small, the binning offset will play less of a role in finding the correlation peak.

The second factor apart from the binning is the difference in clock frequency y. It is closely related to the number of bins selected, $N = 1/y$ (assuming the correct choice of bin width). At the same time, many bins help reduce the standard deviation of noise (Equation 4.20). This is why we can benefit from small differences of the clock frequency that allow for an increase of the number of bins, due to an inverse relationship (Fig. 4.10**b**). The difference in clock frequency is much smaller with the rubidium clocks used or after application of the algorithm to find the clock frequency (Section 4.4). The bins act as a temporal filter. Consequently, if the frequency difference is large, the significance of the correlation features is reduced.

Link transmission Losses in the link reduce the signal and reduce the probability of finding the correlation characteristics. Let us imagine that receiver A sits right at the single-photon source and is not influenced by any losses. The transmission η affects the signal rate r_C, as well as the count rate of photon detections at receiver B. The total significance is $\propto \sqrt{\eta}$ and can be described as

$$S(N, \eta) = \frac{\eta r_C t}{\sqrt{r_A \eta r_B t^2 / N}} = \sqrt{\eta} \frac{r_C}{\sqrt{r_A r_B / N}}.$$ (4.22)
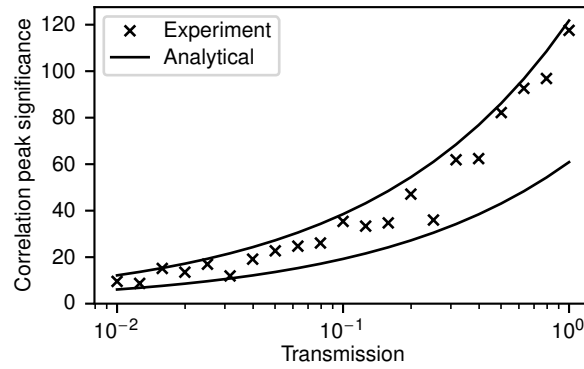
Figure 4.11 | The significance of the correlation peak under varying loss scenarios. The signal-to-noise ratio (coincidence-to-accidentals ratio, CAR) is constant around CAR= 5.4, with CAR = $r_C \eta / (\eta r_A r_B / N)$ for a given transmission η. However, the relative fluctuations (standard deviation) of the accidental correlation events grow, which reduces the significance. The analytical trend (Equation 4.22) is based on the experimental parameters of $r_C = 2.8 \times 10^3$ pairs/s, $r_A = 25.8 \times 10^3$ counts/s, $r_B = 140 \times 10^3$ counts/s, $y = 142$ ns/s ($N \approx 7 \times 10^6$). The lower line corresponds to a non-matching bin offset that reduces the number of correlations by a factor of 2.

This can be confirmed experimentally (Fig. 4.11) and will provide a limit on the maximum distances where clock synchronization with single photons still works (this is described in Section 4.5).

4.4 Detecting the difference of the clock frequency

The large frequency differences between clocks are a big problem for communication scenarios with low signal. The poor *precision* of the oscillators reduces the – already low – signal-to-noise ratio. In the worst-case scenario, clock synchronization with single photons is not possible. For such cases, I developed a frequency compensation algorithm that reduces the frequency difference in a frequency sweep [2; 5]. The same concept has been applied later to compensate for the Doppler shift of the satellite [Wan+21a]. First, I will describe the algorithm and show its application to crystal and rubidium oscillators. Then I conclude with the computational effort that has a significant impact on the feasible synchronization scenarios. The algorithms establish feasibility for long-distance links with small-signal and standard crystal oscillators and scale current point-to-point quantum communication links to multiuser networks.

The frequency difference between the clocks is reduced by sweeping the frequency of one clock in a predefined range. In practice, the physical clock of the analog-to-digital converter can be modified in frequency. Alternatively, a digital correction value (a virtual frequency in some sense) is applied on the computer via post-processing of the photon arrival times, as done here. When the clock frequencies match closer, the timing jitter reduces and the correlation peaks increase their signal-to-noise ratio - this can be related to an archer hitting a target close to its center (Fig. 4.12**a**). If the difference in clock frequency is not compensated, the significance is close to 1. Therefore, it is not possible to initiate the synchronization. In

particular, crystal oscillators are a particular challenge, as they have a frequency precision between 2 and 10 ppm (temperature-controlled crystal oscillators, Table 2.2). This means that the relative frequency difference between two crystal oscillators may be between 0 and 20 ppm. For our crystal oscillators, this is a frequency difference of approximately 18.5 ppm that gives rise to 18.5 μs timing offset every second. To avoid this, the virtual frequency of one oscillator is coarsely swept in 1 ppm steps (Fig. 4.12**b**). The step size depends on the computation time that we can afford. As the timing offset is not known, Fourier-based cross-correlations are applied that correlate every time tag from receiver A with every time tag from receiver B. In doing so, an approximate timing offset is derived. This enables the application of the more efficient start-stop method and fine-tuning of the clock frequency for a better match (Fig. 4.12**c**). Alternatively, the higher signal-to-noise ratio after an initial frequency sweep allows the algorithm to derive the residual frequency difference by measuring the timing offset introduced over time (Equation 4.1), as proposed by [HLK09].

When the frequency sweep is applied, there are significant differences in the photon arrival time histogram that depend on the stability of the clock, as described in the next subsection.
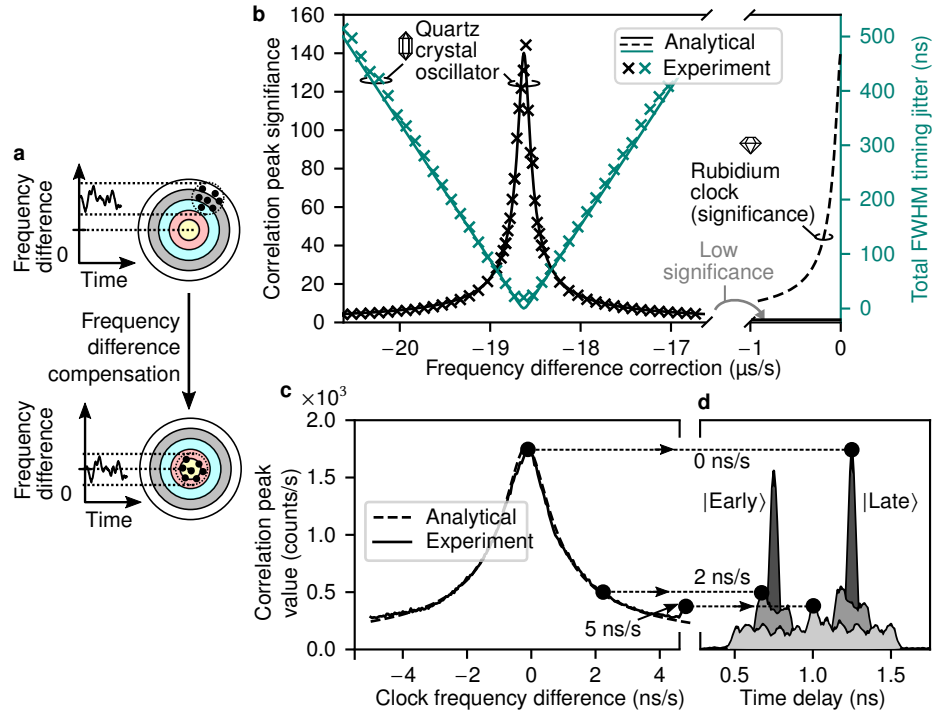
Figure 4.12 | Sweeps of the clock frequency of the slave clock help to find a match with the master oscillator. a, The algorithm increases the *precision* of clocks, i.e. the archer no longer hits a target off-center. However, there is still some scatter that is a symbol for the poor *accuracy* of clocks; that is, the frequency changes continuously. **b**, Crystal oscillators have particularly low precision. As a consequence, a relative frequency difference of approximately -18.5 ppm between clocks is required to compensate for this. Without any compensation, there is a low significance due to large timing jitters that do not permit the initialization of synchronization. Rubidium oscillators, on the other hand, have much better precision and provide a high significance even without any compensation. The analytical trend is $\delta_{\mathrm{FWHM}}^2 = \delta_{\mathrm{init}}^2 + (yt)^2$ (Equation 4.9), with an integration time $t = 0.25$ s and initial full width at half maximum of $\delta_{\mathrm{init}} = 6.09$ ns. **c**, After a coarse search for the approximate clock frequency, some fine-tuning is performed. The signal is maximized when the difference in the clock frequency is zero. **d**, This behavior is apparent in the actual arrival time distribution, which covers longer time delays when the clock frequencies are not matched. Two correlation peaks can even overlap for a frequency difference of 5 ns/s. The figure depicts two correlation peaks, due to the quantum communication protocol used ($|\mathrm{Early}\rangle$ and $|\mathrm{Late}\rangle$ time-bin encoding). The figure is taken from my publications [5; 7].

4.4.1 Crystal oscillators

Crystal oscillators indicate weak stability and have large frequency fluctuations. This means that there is a strong random walk and white noise frequency modulation that becomes apparent at longer integration times (here: 1.26 s). This can be recognized in the experimental timing distribution, which has some asymmetries (Fig. 4.13). The timing distribution indicates asymmetries that I described analytically earlier (Fig. 4.4**b**). They are a feature of strong acceleration of the clocks. This effect of random frequency walk is particularly troublesome for longer integration times, as needed in a low-signal environment (e.g. long-distance communication links). The timing jitter reduces the signal-to-noise ratio, increases the error rate, and reduces the data throughput in a quantum communication scenario. It is possible to compensate for this

by tracking the frequency and applying a continuous live correction during the measurement session (Section 5.2.2).
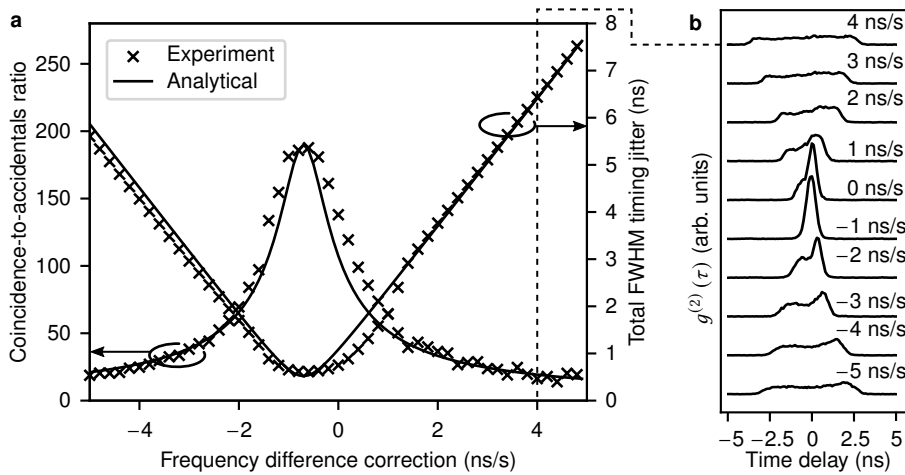

Figure 4.13 | Experimental timing distribution of crystal oscillators. a, When sweeping the frequency of the receiver clock, the signal-to-noise ratio (coincidence-to-accidentals ratio, CAR) reaches its maximum for a correction value of ≈ -1 ns/s. **b**, The timing distribution has some clear asymmetries that give rise to a mismatch between the experimental full-width at half-maximum (FWHM) timing jitter and the analytical trend line. The analytical trend is $\delta^2_{\text{FWHM}} = \delta^2_{\text{init}} + (yt)^2$ (Equation 4.9), with an integration time $t = 1.26$ s and initial full width at half maximum of $\delta_{\text{init}} = 0.52$ ns. The maximum CAR is 190. The figure is modified from my publication [5].

4.4.2 Rubidium oscillators

Atomic references indicate high stability and have small frequency fluctuations. This almost constant frequency results in a symmetrical timing distribution (Fig. 4.14, compare with the analytical trend in Fig. 4.4**a**). The slight asymmetry comes from the very small frequency noise that is only visible at long integration times (here: 10 s). Such clocks are very suitable for long integration times $\gg 1$ s as required in low-signal scenarios and ensure low synchronization timing jitters that keep the data rate high.
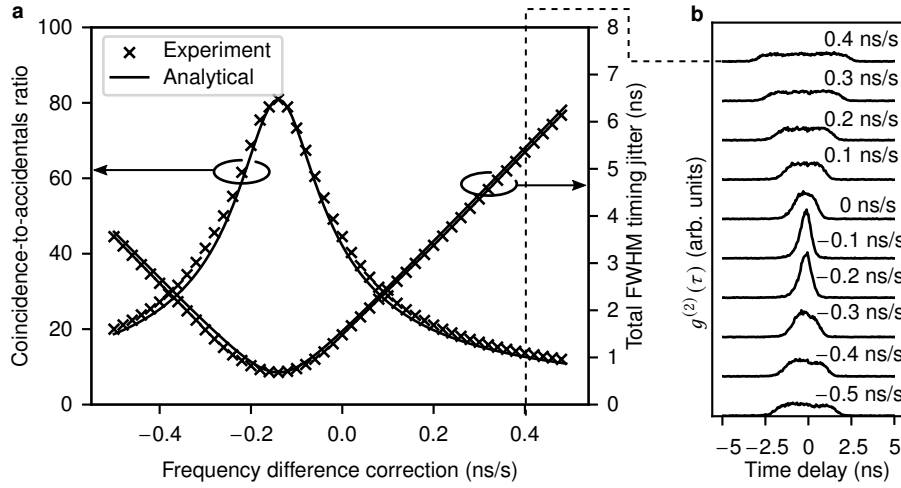
Figure 4.14 | Experimental timing distribution of rubidium oscillators. a, When sweeping the frequency of the receiver clock, the signal-to-noise ratio (coincidence-to-accidentals ratio, CAR) reaches its maximum for a correction value of ≈ -0.15 ns/s. **b**, The timing distribution is very symmetric in contrast to crystal oscillators and matches very well with the analytical trend line. It is described by $\delta^2_{\mathrm{FWHM}} = \delta^2_{\mathrm{init}} + (yt)^2$, with an integration time $t = 10$ s and an initial full width at half maximum of $\delta_{\mathrm{init}} = 0.682$ ns. The maximum CAR is 82. The figure is modified from my publications [2; 5].

4.4.3 Computational effort

The computation time is relevant for the start-up time, i.e. the initialization of the synchronization session and for the subsequent live tracking of the clock frequency during the session. During live tracking, fast calculation times ensure fast matching of clock frequencies. This provides low timing jitters during the communication session. During initialization, an upper limit is set on the frequency sweep resolution by the computation time. In consequence, there will be an upper limit on how well the frequency can be compensated. Thus, this restricts the improvement of the signal-to-noise ratio. This explains why initializing clock synchronization becomes challenging in a low-signal environment with highly imprecise oscillators when asynchronous sources are employed. Asynchronous sources require Fourier-based cross-correlations that demand a lot of computation power.
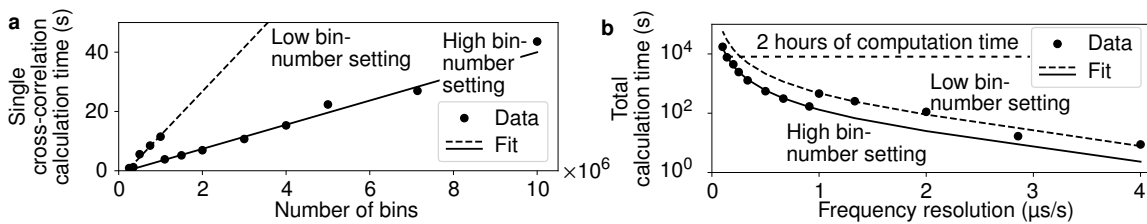
Figure 4.15 | Fourier-based computation times for varying clock frequency resolutions. a, Single-cross-correlation computation time depending on the number of bins N, with the frequency resolution δy being $\delta y = 1/N$ when the bin size is equal to the timing jitter. The personal computer (Table 4.1) applies two different settings for the calculations, depending on the number of bins. **b**, Total computation time for a search window of -20 to 20 ppm with given clock frequency resolution δy (step size). The highest resolution is $\delta y = 1.4$ ppm, considering a computation time limit of 2 h (Equation 4.23). The figure is taken from my publication [5].

Table 4.1	Specifications of the computer.	
Parameter	**Value**
Processor	Intel(R) Core(TM) i5-8250U CPU
Speed	1.60 GHz (1.80 GHz)
RAM	16 GB
Operating system	Windows 10, 64-bit based processor
Language	Python 3.7.0 64 bit, NumPy 1.19.4
Environment	Spyder 5.1.5

The computer is a standard laptop, where the Python library NumPy [Har+20] is used in the scientific Python development environment Spyder [Ray09].

In my implementation in the Python environment NumpPy [Har+20], a single fast Fourier-based cross-correlation takes up to 40 s for an array size of $N = 10^7$ (equal to the size of the binning array). This provides a resolution of the frequency of $\delta y = 1/N$. The total computation time for a frequency sweep in the range $\Delta Y = 40$ ppm (-20 to 20 ppm), decided by the precision of the crystal oscillators according to the datasheet) with resolution δy, is

$$T_{\text{tot}} = \frac{\Delta Y}{\delta y} T(\delta y), \tag{4.23}$$

when every correlation with resolution δy takes time $T(\delta y)$. This limits the frequency resolution to $\delta y = 1.4$ ppm, with a maximum calculation time T_{tot} set to 2 hours (Fig. 4.15). Although this much time is typical for new crystal oscillators without calibration, the time is not required later, as the search range Δy is much reduced. Furthermore, there is much room for optimization. The loop to perform the frequency sweep is parallelizable and calculations can be performed on a graphical processing unit.

4.5 Conclusions with asynchronously heralded single-photon sources

The compensation of difference of the clock frequencies enables the initialization of clock synchronization with crystal oscillators at a much lower signal than previously published [HLK09]. With sufficient signal, no pre-compensation is required before applying the cross-correlations. The significance is high enough (reaches the threshold of at least 7) and correlation peaks can be found even with large differences in the clock frequency, e.g. 20 ppm (Fig. 4.16**a**). When the signal is much lower, this becomes impossible (Fig. 4.16**b**). Note that the exact frequency is still needed and will be extracted in a second step.

In this thesis, I have tested lower signal-to-noise ratios that would result in a significance of barely 2.5 with a difference in clock frequency of $y = 200$ ppm. As a consequence, it would not even be possible to start with the algorithm to find the clock frequencies by measuring the timing offset, as described in [HLK09]. In this work, I propose to vary the frequency and check

the signal every time [2; 5] for this crucial initial step in low signal-to-noise environments. Improvements in the uncertainty of the clock frequency by a factor of 140 to $y = 1.4\,\text{ppm}$ are feasible, depending on computation times (Fig. 4.15). This provides an improvement in significance by a factor $\sqrt{140} \approx 12$ from 2.5 to a value close to 30.
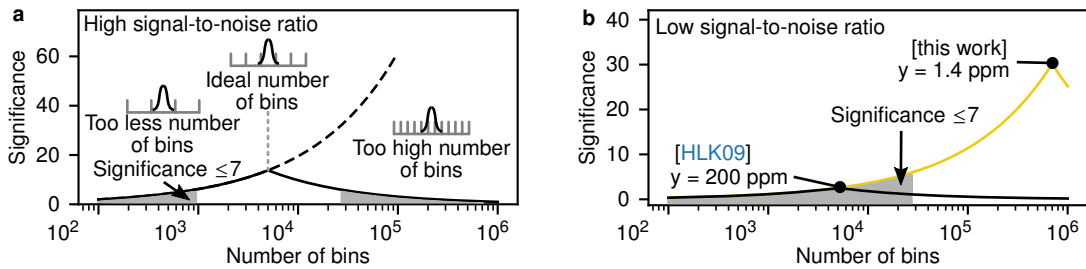

Figure 4.16 | Comparison of literature and this work. a, Time tags are recorded during the acquisition time and sorted into N number of bins that affect significance (see Section 4.3.3). With single count rates $r_A = r_B \approx 77 \times 10^3$ counts/s, signal rates $r_C \approx 15 \times 10^3$ pairs/s, and differences in clock frequency $y = 200\,\text{ppm}$, the significance reaches 13 - sufficient for the initialization of the synchronization. **b**, Methods by [HLK09] fail for lower signal-to-noise ratios, with the rates $r_A = 200 \times 10^3$ counts/s, $r_B = 800 \times 10^3$ counts/s, $r_C = 14 \times 10^3$ pairs/s, as the correlation peak cannot be found due to the low significance of 2.5. Here, I introduce compensation of the difference of the clock frequency, following in a higher significance by the square root of number of cross-correlations in the search of the clock frequency (here is a factor of 12 improvement, yellow curve). The figure is taken from my publication [5].

The compensation algorithm enables reliable identification of the correlation peak under signal-to-noise ratios lower than those published and increases the distances where clock synchronization with single photons is feasible. With crystal oscillators in place, strong signals and small distances are required. As a reference, I take the publication [HLK09] that has a CAR = 230 (similar to the signal-to-noise ratio). As an initial value of the following simulation (Fig. 4.17), this shell corresponds to the rates between a correlated photon pair source and one receiver without any extra loss (0 dB loss). By compensating for the frequency, there could be a CAR of almost 100 that would still make clock synchronization with single photons realizable. This corresponds to 20 dB additional attenuation / loss or, equivalently, 20 dB improvement. The loss can also be represented by 118 km of SMF-28 fiber [Inc14]. The dispersion of this fiber is another contribution to a constant timing jitter, similar to the detection jitter, and behaves as a system constant. On a 70 km fiber link, there is almost no contribution to the total timing jitter with pulse widths of 50 ps (Section 5.3.2).

The developed compensation method identifies the correlation peak well with a moderate signal, as in [5] or [Ste+17]. On the other hand, when there is a very small signal, such as in long distant links [Eck+21], it is not possible to initialize the synchronization with a poor clock precision of 20 ppm. In such cases, I recommend the following options:

1. calibration of the clocks under stronger signal,

2. narrowing down the search range with the help of previous communication sessions,
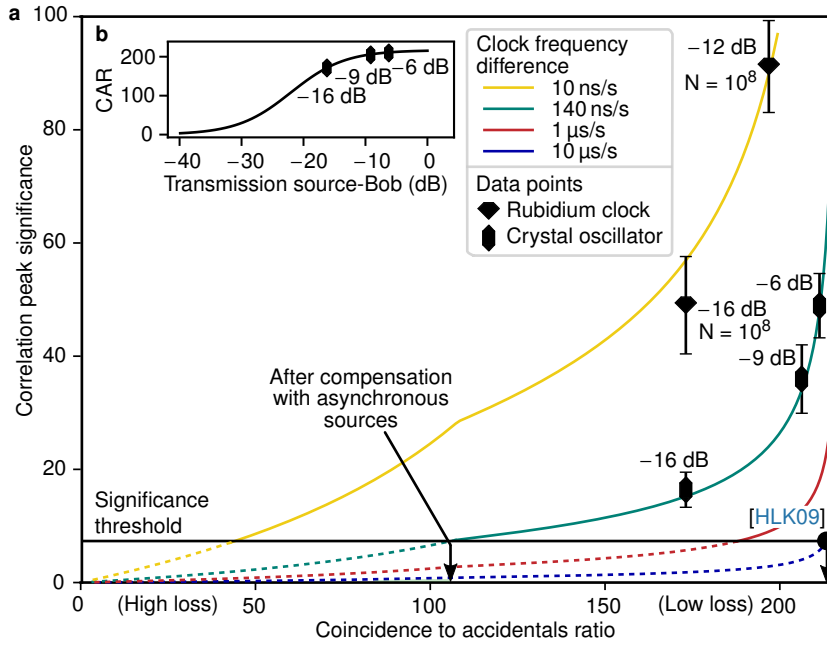
Figure 4.17 | The significance of the correlation peak for different signal-to-noise scenarios.
a, Estimation of the significance of the correlation peak under different coincidence-to-accidental ratios (Equation 4.22) and differences of the clock frequency. The loss increases from right to left. The experimental data points are based on the initial (before adding loss) rates of $r_A = 200 \times 10^3$ counts/s, $r_B = 800 \times 10^3$ counts/s, $r_C = 14 \times 10^3$ pairs/s, $r_{back} = 5 \times 10^3$ counts/s (constant background rates) and the maximum number of bins in the cross-correlation $N = 10^8$. The number of bins is adapted to the spread of the correlation peak, caused by the residual difference in clock frequency, with $\delta y = 1/N$. The error bars indicate the standard deviation after a slight variation in the size of the bin by $\pm 5\%$. The threshold to recover the correlation peak is a significance of 7, which provides a probability of $\approx 10^{-12}$ of a peak found incorrectly [HLK09]. Sweeps of the clock frequency increase the visibility of the correlation peak and thus enable higher noise resistance. **b**, Coincidence-to-accidentals ratio depending on the transmission from Alice to Bob. The full-width coincidence window is constant at 418 ps. The figure is taken from my publication [5].

3. boosting the computation algorithms to achieve smaller computation times, or

4. pulsing the single-photon source.

I will consider the last option in the following Section 4.6. By pulsing the single-photon source, the computation time reduces by orders of magnitude, and finding an accurate clock frequency becomes simple.

4.6 Algorithm for clocked single-photon sources

When there is a clocked single-photon source instead of an asynchronous single-photon source, the steps for clock synchronization change. For this, I developed an algorithm that is dedicated to clocked single-photon sources [6; 7]. Such clocked sources can be, e.g., pulsed driving of the spontaneous parametric down-conversion process for photon pair generation or faint pulse

sources that are intrinsically pulsed. In the following, I will discuss the main differences in each step of the synchronization protocol for the case of clocked single-photon sources.
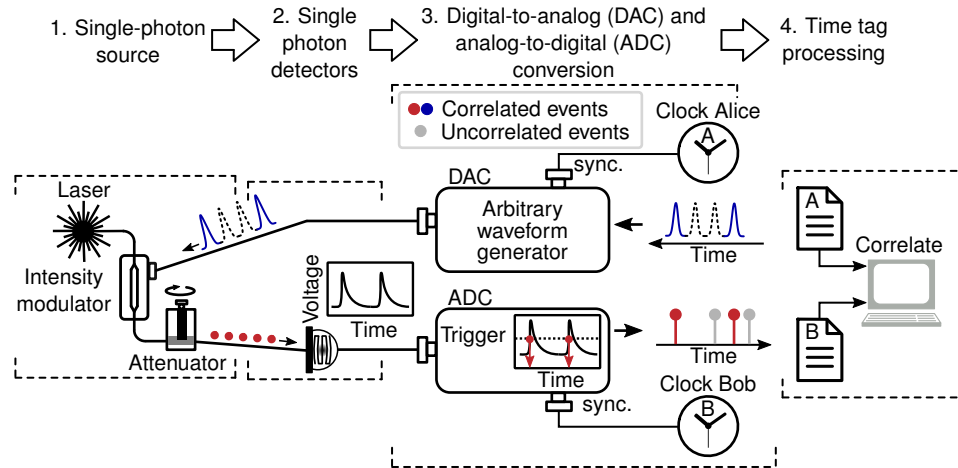

Figure 4.18 | Experimental setup for single-photon detection and processing with a faint pulse source for quantum key distribution. A computer generates a data bit sequence with time slots |Early⟩ or |Late⟩. This is encoded in an arbitrary waveform generator that acts as a digital-to-analog converter. The generated sequence is sent to an electro-optical intensity modulator. Here, optical pulses are created and attenuated to the single-photon level. The following detection procedure applies as in correlated photon pair setups (Fig. 4.2). The generated time stamps are processed on a computer that takes care of correlating the sending times with the received time-of-arrival.

The exemplary experimental setup consists of a faint pulse source, where an arbitrary waveform generator prepares a sequence of pulses that is transferred to the receiver (Fig. 4.18). The sequence is typical for a time-bin quantum key distribution system with the states encoded in a time slot |Early⟩ and |Late⟩. An intensity modulator translates this into optical pulses that are attenuated to the single-photon level. Subsequently, the receiver measures it with the same setup as in systems with correlated photons (Fig. 4.2). In the last step, the received sequence is processed to enable synchronization between the clock of the arbitrary wave generator and the clock of the analog-to-digital converter. The processing begins with the "binning" in the following paragraph.

4.6.1 Binning

While it is required to introduce bins for the photon arrival times in asynchronous sources, this is not the case in clocked single-photon sources (Fig. 4.19). In a clocked single-photon source, the arrival time is predefined by the pulse envelope. These defined slots repeat with the clock rate of the single-photon source and allow for a highly efficient two-stage process that directly uses the high resolution of the detected time stamps, but saves computation power due to a smaller observation window. It is possible to reduce the observation window from the integration time of 100 ms to the inverse of the pulse repetition rate, as the potential arrival time of the photons is clearly defined by the pulses. The two steps consist of deriving a

1. *relative timing offset* with a value $0 \dots 1/f_c$, and the calculation of the

2. *absolute timing offset* with a value that is an integer multiple of the inverse clock rate.

When adding both, the algorithm outputs a complete, high resolution, and absolute timing offset between the clocks.
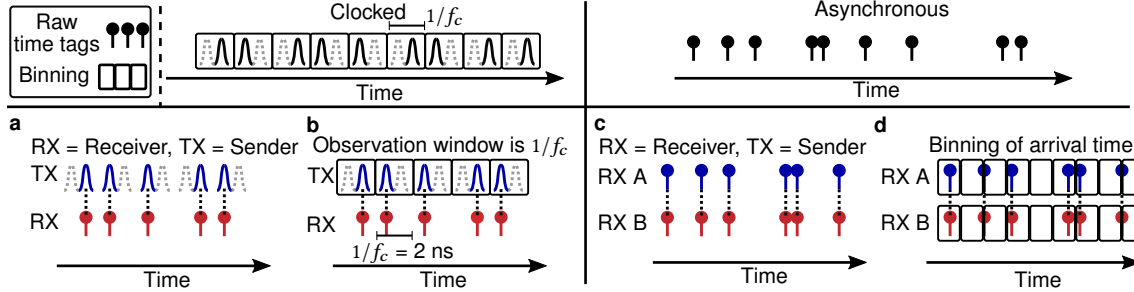

Figure 4.19 | Binning in asynchronous and clocked single-photon sources. a, Sources that are driven by a pulse laser indicate the available time slots given by the pulse envelope. The average repetition rate is $1/f_c$. In this example, the source is used for quantum communication and randomly chooses a time slot $|\text{Early}\rangle$ and $|\text{Late}\rangle$ for the bit value 0 or 1. **b**, No bins are introduced. Instead, the relative arrival time within the average pulse rate is calculated. The observation window is $0 \dots 1/f_c$. **c**, When the single-photon source is driven by a continuous-wave pump, the emission time is random. **d**, The introduction of bins artificially reduces the timing resolution, but it is necessary to reduce the computation time. The observation window is the integration time, for example 0 to 100 ms.

4.6.2 Cross-correlations

The *relative timing offset* is derived by a highly efficient modulo operation (Fig. 4.20**a** with its comparison to the asynchronous counterpart in **c**). The arrival time T_i within a given repetition rate of the single photon source $1/f_c$ for every time stamp t_i is

$$T_i = \text{mod}_{1/f_c}(t_i). \tag{4.24}$$

This gives a statistical envelope of the arrival times as

$$g^{(2)}(\tau) = \text{Histogram}[T_i, \tau], \tag{4.25}$$

with the observation window $0 \dots 1/f_c$. The modulo operation (mod) acts as an operator for cross-correlations here, as it calculates the time difference between the time tag and the edges of the repetition rate window. It behaves as a cross-correlation between the source (its repetition rate) and the receiver (the photon arrival times). In contrast to the start-stop algorithm or the Fourier-based cross-correlations (complexity $O(n \times m)$, with m transmitted and n received photons), the modulo operation only uses a total array length of n (complexity $O(n)$, with n received photons). In summary, we benefit from the following features, which accelerate the computations:
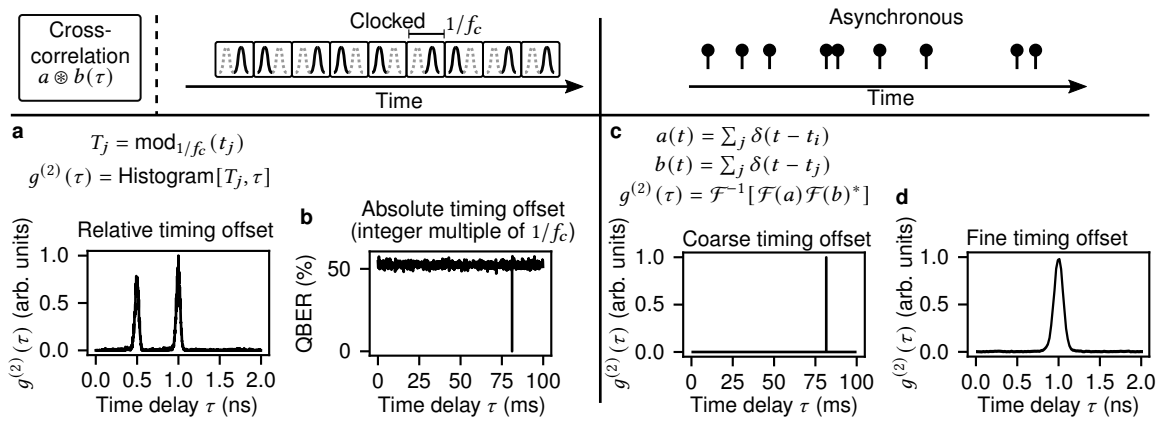
Figure 4.20 | Cross-correlations and finding the timing offset. a, In asynchronous sources, the binned array is cross-correlated (based on a fast Fourier transformation) to find a coarse timing offset. **b**, In a second step, a higher resolution is derived using cross-correlations based on the Start-Stop method. **c**, In pulsed sources, the modulo operator is first applied to find a relative timing offset within the average clock rate of the source (here it is $f_c = 1/2$ ns). As a consequence, the frequency sweep algorithm also benefits. Note that there are two correlation peaks here, since the source is used for quantum communication with two bins $|\text{Early}\rangle$ and $|\text{Late}\rangle$ that represent the bit values 0 and 1. **d**, In the second step, the quantum bit error rate (QBER) is observed by time shifts of multiple integers of the source repetition rate. This provides an absolute value of the timing offset. The figure is modified from my publication [6].

1. The modulo operation is intrinsically more computational power-saving (complexity depends only on the number of time tags and the observation window is only $0 \ldots 1/f_c$, instead of over the full integration time.)

2. The single cross-correlation time is independent of the desired frequency resolution and *independent of the other receiver*. The computation time depends only on the number of time stamps to be processed. In asynchronous sources, the number of bins N is related to the frequency resolution as $1/N$ (Section 4.4.3).

The *absolute timing offset* is derived by comparing the sent and received data bits in a second step (Fig. 4.20**b** with its comparison with the asynchronous counterpart in **d**). This step requires some kind of pattern that is sent out and recognized at the receiving end. In faint pulse sources, the pattern could be represented by the data bits themselves or by other shared public information. The publication [Wan+21a] describes a nice idea of using the vacuum state in the decoy-state protocol. By evaluating the correlation between the detected photons and the publicly available random numbers used for vacuum-state preparation, it becomes possible to extract the time offset. Although it is not specifically designed as a synchronization string, it can be used in this way. In sources of correlated photons, only a single Fourier-based cross-correlation is required to detect the timing offset. When the sent sequence is aligned with the received sequence, the absolute timing offset is right, providing the lowest error rates of the communication session. In simple terms, the algorithm finds the absolute timing offset

by time shifts of the received bit sequence by multiples of the clock cycle until there is a match to the sent bit sequence. In turn, this leads to the lowest error rates.

4.6.3 Detecting the difference of the clock frequency

The clock frequency is identified as part of the concept of frequency sweeps, which is the same as in asynchronous sources but much faster. At first, the frequency of the source is just an estimate. The frequency is uncertain due to the clock precision and accuracy and requires some refinement. The frequency sweep finds the exact clock frequency and incorporates the modulo operation (clocked single-photon sources), instead of Fourier transformations (asynchronous sources). The modulo operation has several advantages:
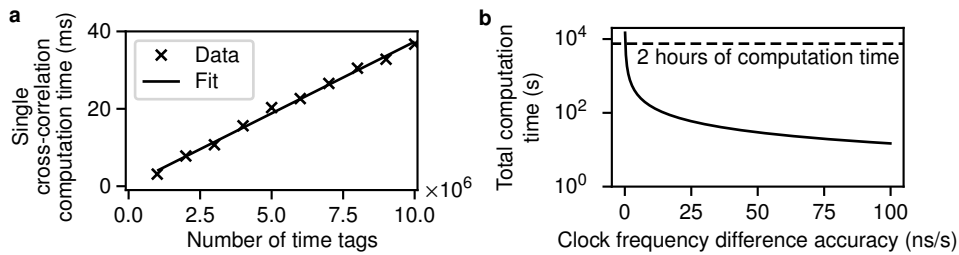
Figure 4.21 | Computation time of modulo-based cross-correlations. a, The computation time increases linearly with the number of time tags (array size). **b**, The total computation time is $T_{tot} = T(\delta y)\Delta Y/\delta y$ (Equation 4.23) with a resolution of the clock frequency δy for a range of $\Delta Y = 40$ ppm (from -20 to 20 ppm) and the computation time for a single cross-correlation $T(\delta u) = $ const $ = 37$ ms (for $N = 10^7$ time tags). With a maximum computation time of 2 hours [5], the clock frequency resolution can be as low as 0.2 ns/s. The figure is taken from my publication [7].

1. It is extremely fast. The same array size of 10^7 takes 40 ms with the modulo operator (Fig. 4.21**a,b**), but 40 s with Fourier-based cross-correlations. This represents the processing of 10 Million time stamps (modulo operation) or 10 Million bins (Fourier-based cross-correlation).

2. It enables the initialization of the synchronization under low signal and simultaneously crystal oscillators with low precision. Given the same maximum computation time, the clock frequency can be matched with a resolution approximately three orders of magnitude higher. For a search range of -20 to 20 ppm, the residual difference of the clock frequency can be reduced to 0.2 ns/s (Fig. 4.22), instead of only 140 ns/s with asynchronous sources.

3. The receivers can process the data independently of the other receiver. For example, in clocked entangled photon pair source, the receivers do not require the correlation rates, but just the single photon rates at each individual site. This concept is very powerful, as the single-photon rate is much higher than the correlation rate. It enables high-performance and fast synchronization.

This gives clocked sources a superior advantage over asynchronous sources and enables the feasibility of clock synchronization at very low signals, such as long-distance links [Eck+21].
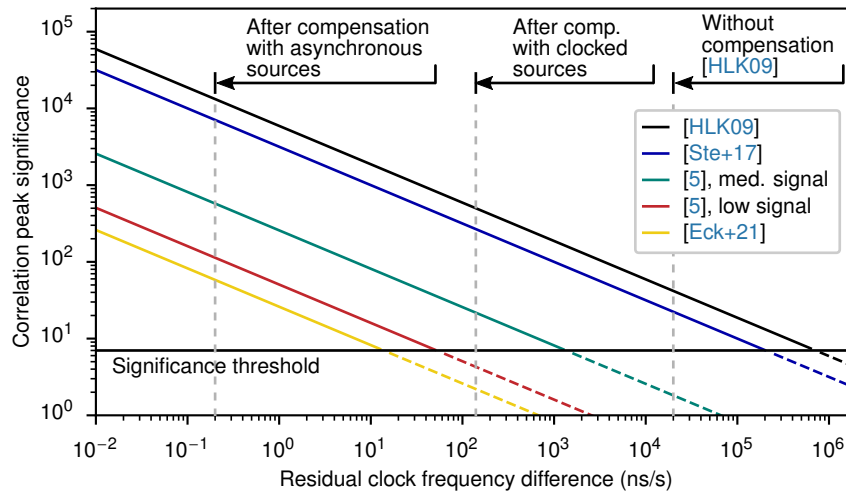

Figure 4.22 | Increase in significance by compensating the frequency difference. The figure depicts the significance of the correlation peak for a selected set of singe-photon-rate scenarios from literature. The significance of the correlation peaks indicates their visibility and their likelihood of detection. The plot shows the smallest significance when initializing the synchronization without compensation [HLK09]. The significance increases when compensating the frequency difference, whereby it can be compensated to a smaller frequency difference when having clocked sources instead of asynchronous sources, due to a shorter computation time. Clocked sources allow synchronization in regimes of very low signal noise ratio ratios, such as in [Eck+21] (signal-to-noise ratio of 5, 143 km free-space quantum key distribution link) or in the low signal regime of [5]. This is not possible with asynchronous sources or without compensation, as the threshold of 7 is not reached. Other references are [Ste+17] and [HLK09]. The computer specifications are described in Table 4.1. The figure is taken from my publication [7].

4.6.4 Conclusions with clocked single-photon sources

Pulsing the single-photon sources is a great method to enable synchronization even at the lowest signal-to-noise ratios with crystal oscillators in place. When initialization of the synchronization was not possible with asynchronous sources, pulsed operation could still enable it successfully. This comes from the fact that the clock frequencies can be calculated with almost three orders of magnitude better precision (Fig. 4.22), which is essential during the initialization of the synchronization. Furthermore, the receivers just need their own single photon rate and not the correlation rate when using clocked entangled photon pair sources. Essentially, the receivers are capable of independent processing. In consequence, there is much more signal available for clock synchronization that in turn enables higher performance. In summary, pulsing the source provides a new range of applications scenarios with crystal oscillators: low-signal regimes. Those may include long-distance and satellite-based quantum communication links or even the metrology of moving objects with low reflectivity (covered in Section 6.2.1).

5 Implementation of the protocol

The last chapter covered the steps for initializing the synchronization session. Now, a live synchronization session will run, where the unstable, fast drifting clocks are kept locked in frequency. As an example, the synchronization with single photons is applied to a quantum communication system, where data are exchanged simultaneously. This chapter contains the following highlights that advance the state-of-the-art, which is partially covered in my own publications [3; 5; 6; 7]. Specifically, this chapter

1. develops a fast algorithm for live frequency tracking with record-high performance with quartz oscillators [3; 6; 7] (Section 5.2.2),

2. provides an in-depth analysis of the performance for an emulated scenario with atmospheric turbulence of a satellite link [5] (Section 5.3.1), and real fiber and free-space link scenarios (Section 5.3.2),

3. demonstrates the first successful synchronization session on a free-space link with only quartz oscillators that allows quantum key distribution (Section 5.3.2).

The following section describes the experimental setups for the quantum key distribution (Section 5.1). As a quantum key distribution session runs for long time, the clock frequencies vary and have to be tracked. The concept of efficient tracking and the concrete adaptation to a quantum key distribution system is part of the next Section 5.2. Then I will describe and apply the synchronization protocol to real link scenarios (Section 5.3). This includes an experiment on a 1.7 km free-space link (Section 5.3.2) and a 70 km deployed fiber link between Jena and Erfurt (Section 5.3.2). I will conclude the chapter with a comparison to the literature (Section 5.4).

5.1 Experimental setup

As part of the implementation, a graphical user interface is created with the Python software tool PyQt [Riv22]. It shows valuable parameters that are important for the quantum key distribution protocol, such as the number of correlation events, the quantum bit error rate, or the key rate (Fig. 5.1). The following single-photon source types are implemented:

1. an *entangled photon source* in the BBM92 [BBM92b] quantum key distribution protocol, and

2. a *faint pulse source* in the BB84 [BB14; LMC05; Ma+05] quantum key distribution protocol.

I will give a brief overview of these source types, its corresponding measurements in the quantum key distribution protocol, and its relevance for clock synchronization.
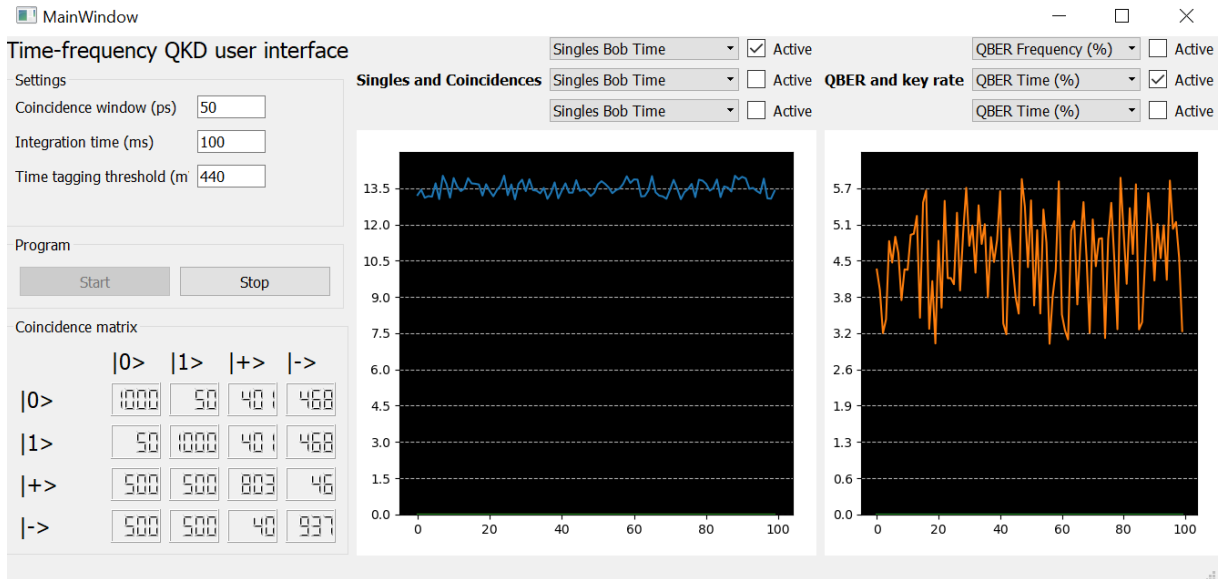

Figure 5.1 | The graphical user interface. The interface is designed with the Python toolbox PyQt [Riv22] and shows the correlation matrix and other useful live data, such as the single-photon count rate or the quantum bit error rate (QBER).

5.1.1 The entangled photon source

The entangled state is generated in a nonlinear parametric downconversion process. With sufficiently low optical pump power, the probability is high of generating true single-photon pairs, called signal *s* and idler *i* [Bra+22] (Fig. 5.2**a**). The generated state $|\Psi\rangle$ is expressed by [Jen+00],

$$|\Psi\rangle = \frac{1}{\sqrt{2}}\left(|H_sH_i\rangle + e^{i\phi}\,|V_sV_i\rangle\right), \tag{5.1}$$

with a relative phase ϕ between the horizontal and vertical polarization contributions. This means that when measuring (Fig. 5.2**b**) a horizontal state $|H_s\rangle$ of the signal photon, the probability is 100 % to measure a horizontal polarization of the idler photon $P(|H_i\rangle) = 1$, assuming that the measurements are in the same polarization basis (here: horizontal/vertical). The same is valid when measuring the vertical polarization state of the signal photon $|V_s\rangle$, which gives $P(|V_i\rangle) = 1$ for the idler photon (Fig. 5.2**c**). Theoretically, the probability is zero for measuring a vertical polarization of the idler photon $P(|V_i\rangle) = 0$, when a horizontal polarization is measured for the signal photon $|H_s\rangle$ (again, the same basis is selected). In practice, this probability is larger than 0, due to poor state fidelity or imperfections in the polarization
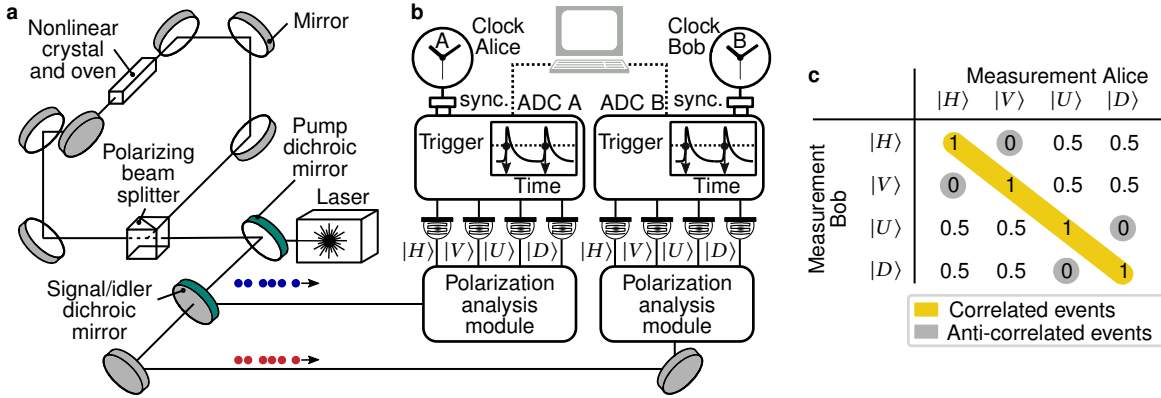
Figure 5.2 | Generation of entangled photons and its measurement in a quantum key distribution protocol. a, Entangled photon sources generate a high rate of photon pairs, for example, in a cross-periscope configuration [Bra+22]. **b**, The generated state is measured with respect to its polarization and then time-stamped in an analog-to-digital converter (ADC). As the photons are entangled, the measurement outcomes are identical when the measurement is performed on the same basis. This can be used to distribute secure bits of information in a quantum key distribution protocol. **c**, Correlation matrix for different measurement settings. The receivers Alice and Bob each project the input state on a polarization horizontal (H), vertical (V), up-diagonal (U), or down-diagonal (D), where H/V corresponds to the H/V polarization basis, and U/D corresponds to the U/D polarization basis. When the polarization measurement at the receiver Alice for the signal photon is identical to the receiver Bob for the idler photon, the number of correlations is maximized (normalized to 1 and highlighted in yellow color). Any measurement on a different polarization basis results in an inconclusive and random outcome.

analysis module, and gives rise to correlation events that cause errors in the quantum key distribution channel.

5.1.2 The faint pulse source

Faint pulse sources create a coherent state with a mean photon number $\bar{n} = |\alpha^2|$, that is, a superposition of states with different photon numbers n [FF+06b],

$$|\Psi\rangle = |\alpha\rangle = e^{-\frac{|\alpha|^2}{2}} \sum_{n=0}^{\infty} \frac{\alpha^n}{\sqrt{n!}} |n\rangle . \tag{5.2}$$

Assuming that the faint pulse source generates polarization states as well, the states $|\Psi, H\rangle$ and $|\Psi, V\rangle$ are prepared by, for example, polarization modulators. After preparation at the sender, they are projected on the horizontal or vertical polarization at the receiver $|H\rangle$, $|V\rangle$, respectively. When the polarization of the prepared and measured states matches, the number of correlations is maximum. For example, the probability is 100 % to measure a horizontal polarization $P(|H\rangle) = 1$ and 0 % to measure a vertical polarization $P(|V\rangle) = 1$, when the horizontal polarization $|\Psi, H\rangle$ has been prepared. In this thesis, I have not implemented a polarization-based faint pulse source, but applied time and phase encoding with intensity and phase modulators (Fig. 5.3). The arrival time is determined by the time bins $|\text{Early}\rangle = |0\rangle$ and $|\text{Late}\rangle = |1\rangle$ with an intensity modulator and the phase states $|+\rangle$ and $|-\rangle$ with a phase modulator.
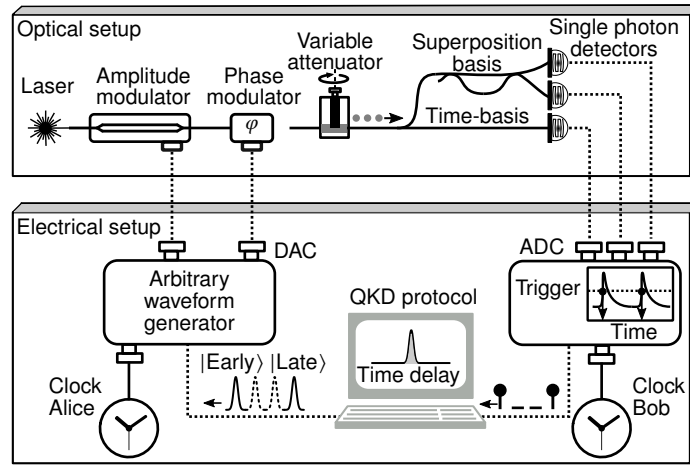
Figure 5.3 | Generation of faint pulses and its measurement in a quantum key distribution protocol. The states |Early⟩ and |Late⟩ in the time basis are prepared by a digital-to-analog converter (DAC) that drives an intensity modulator. The states in the superposition basis are prepared with a phase modulator. The measurement takes place in the time basis, where the photon arrival time is measured (whether it is in the bin |Early⟩ or |Late⟩) and the superposition basis with an interferometer, where the phase is measured (a single photon arrives at output port 1 or 2 of the interferometer). The photon arrival time is time-stamped by an analog-to-digital converter (ADC). Modified figure from my publication [7].

This prepares the coherent states $|\Psi, 0\rangle, |\Psi, 1\rangle, |\Psi, +\rangle$, and $|\Psi, -\rangle$. The correlation matrix is identical to a setup with entangled photons. There is a maximum number of correlations when the basis is the same for the prepared state and its projection at the receiver (Fig. 5.4).
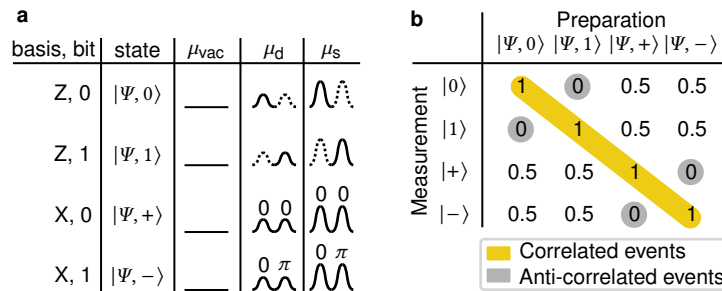
Figure 5.4 | The prepared and measured states in a time-phase encoding faint pulse source. a, The bits are encoded in the Z-basis (arrival time) or in the X-basis (phase). When the photon is in a bin |Early⟩ (|Late⟩) in the Z-basis, it corresponds to a bit value 0 (1). Similarly, when the phase difference is 0 (π) in the X-basis, it corresponds to a bit value 0 (1). To increase the secure data rate [LMC05; Ma+05], three different mean photon numbers are selected $|\alpha|^2 = \mu_{vac}, \mu_d, \mu_s$, for the vacuum state, the decoy state, and the signal state, respectively. **b**, As with the quantum key distribution with entangled photons, we obtain an analogous correlation matrix. When the prepared state is projected onto the correct measurement, there is a maximum number of correlations.

5.1.3 Conclusions

The correlations on specific channel combinations are important for the synchronization protocol. Here is only a high signal-to-noise ratio that gives the best synchronization performance.

Furthermore, when the polarization of light gets altered during propagation, the measurement results for the polarization-encoded protocol change. This reduces the signal-to-noise ratio of previously correlated channels. It raises the difficulty of synchronization and may make it impossible.

5.2 Concept of the frequency live tracking

The algorithm implemented is divided into two parts: the initialization, which takes several seconds (Fig. 5.5) and the live part, where the receiver frequency is kept locked to the sender in real time. The initialization is almost identical to the protocol described in Chapter 4, but with a focus on quantum key distribution systems that require one to filter some data. The highest priority for successful and high-performance clock synchronization is to maximize the signal-to-noise ratio. It gives a positive feedback loop, i.e., when algorithms give a higher signal-to-noise ratio, the clock frequency can be estimated with higher precision, which in turn provides an even higher signal-to-noise ratio. This optimization is done on three levels:

1. selecting the channel combinations of the quantum key distribution system that have the strongest signal,

2. compensating for the difference in clock frequency during initialization, and

3. tracking the frequency of the master clock with the corresponding adjustments of the slave clocks.
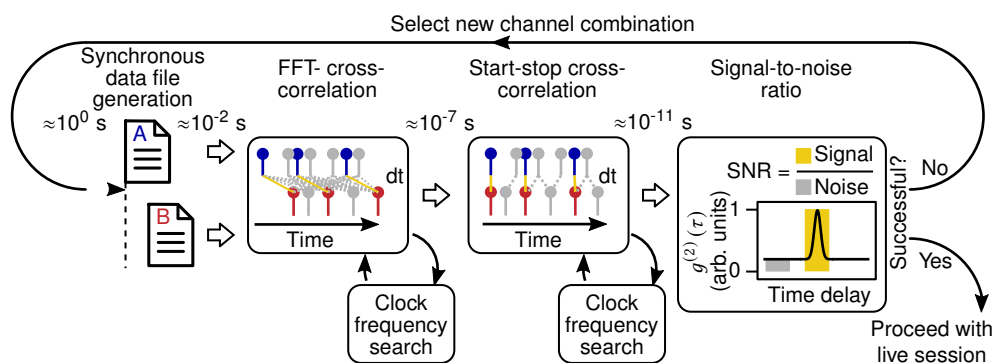
Figure 5.5 | Implementation of the clock synchronization algorithm. The first part is the generation of synchronous data files using, e.g., the network time protocol [Mil11] which provides a temporal precision of milliseconds ($\approx 10^{-2}$ s). This ensures that both files share the same correlation events. The step is followed by cross-correlations that are based on the fast Fourier transformation (FFT) algorithm. This is done in combination with a clock frequency search that increases the timing precision to a few hundreds of nanoseconds ($\approx 10^{-7}$ s). The next step is to perform Start-Stop correlations with a fine-tuning of the clock frequency that provides picosecond ($\approx 10^{-11}$ s) timing precision. The final step is to check the signal-to-noise ratio. When there was a poor signal-to-noise ratio (smaller than 5-7) that resulted in failure of the initialization of synchronization, a new channel combination is selected.

In the beginning, it is not clear whether a channel combination with strong signal has been selected, as the timing offset is uncertain between the communicating parties. Only after the precise timing offset is found is it possible to derive the signal-to-noise ratio. It can be derived from counting the correlation events from the single-photon source and requires the reduction of the temporal dispersion from the clocks and the measurement uncertainties. That is why the first step is to process the time tags and perform cross-correlations and frequency sweeps for clocks with poor precision. As part of the frequency sweep algorithm, several cross-correlations are performed with a selected frequency correction (Fig. 5.6). When there is no significant correlation peak appearing now, it is required to select a different channel pair in the system for quantum key distribution. This could be the vertical channel of the local receiver (instead of horizontal) and to correlate it again with the horizontal / vertical channel of the remote receiver. Note that it is not possible to receive the distinction between horizontal and vertical from the remote receiver for security reasons. Details of this system and the corresponding experimental setup are provided in Section 5.1. When one channel selection brings a significant correlation peak, the clock frequency found is valid for all other channels as well. This comes from the fact that a single clock provides the same time for all channels for a given receiver.

The security in quantum key distribution systems is not compromised by this method. For generating the key, the remote receiver of the photons publishes the choice of the basis (measurement in the horizontal/vertical basis or diagonal-up/diagonal-down basis), but without full channel information (e.g., whether horizontal or vertical polarization has been measured). The full channel information is only sent for a small fraction of data and is not used to create a secure key. This small fraction of data contains only a few correlation events, which results in high statistical uncertainty and makes it less useful for synchronization. The useful data are only those that are later used for the key. As there are more correlation events available, it allows for a fast synchronization procedure. In addition, these data are exchanged anyway, which in turn does not compromise security.

Apart from publishing the channel selection, the time tag data itself is also relevant for security. This comes from the fact that the channel information could be hidden in the time tags, which is a serious security loophole [PDT22b]. The origin lies in the differences in runtimes of the signal towards the time-to-digital converter. To be more concrete, the photon measured in the horizontal polarization channel may propagate longer optically than the photon in the vertical channel. There might also be differences in the electrical path lengths. Proper time synchronization closes the loophole by applying a correction value to the time tags before sending them over the public channel.

After matching the clock frequency, the algorithm proceeds with frequency locking. While keeping the frequency locked, other quantum key distribution parameters are calculated, like the coincidental counts, accidentals correlation events, quantum bit error rate or heralding of the single-photon source. Ideally, these calculations run as a second computation thread, to not slow down the processing for clock synchronization. Fast processing is highly relevant to

keeping the frequency locked. This is discussed in the next section after a short trip into the analytical estimations of the timing jitter while live tracking.

---

1 **Input:**   time tags Alice t_A and Bob t_B
2   Functions: READ TIME TAGS(), CONVOLUTION()
3 **Output:** difference in the clock frequency
4 t_A, t_B = READ TIME TAGS(integration time = 0.1 sec)
5 frequency vector = $-20\,\mu s/s \cdots + 20\,\mu s/s$, step: $140\,ns/s$
6 bins = $0 \ldots 0.1\,s$, step: $14\,ns$
7 Peak = data array(frequency vector size)
8 index = 0
9 **for** y_{corr} **in** frequency vector **do**
10 $\quad$ $t_{B,\mathrm{corr}} = t_B + (t_B - t_B[0]) \times y_{\mathrm{corr}}$
11 $\quad$ c = CONVOLUTION($t_A, t_{B,\mathrm{corr}}$, bins)
12 $\quad$ Peak[index] = max(c)
13 $\quad$ index+ = 1
14 difference in the clock frequency = $-$frequency vector(argmax(Peak))

Figure 5.6 | Pseudocode for the clock frequency sweep. The convolution can be base on a Fourier transform (FFT) or the Start-Stop method. The FFT approach is taken when the precise timing offset is not known. The algorithm includes the following variables: time stamps from Alice and Bob $t_{A/B}$, peak values of the cross-correlations Peak, clock frequency vector for correction y_{corr}, frequency corrected time stamps from Bob $t_{B,\mathrm{corr}}$, cross-correlation output c. Note that the bin step size of $14\,ns$ corresponds to the integration time times the resolution of the frequency vector. Higher resolutions of the (normalized) clock frequency ($< 140\,ns/s$, i.e. $1.4\,Hz$ deviation from a $10\,MHz$ frequency carrier) require considerably higher computation effort (Section 4.4.3). If there is knowledge of the approximate difference of the clock frequency, the range for the frequency search can be reduced.

5.2.1 Achievable synchronization timing jitter during live tracking

The final synchronization jitter after live correction during a communication session is decided by clock drift and the number of correlation events during measurement.

In this subsection, I present analytical estimations of the synchronization limits that might be helpful for easy transfer of the synchronization protocol to any communication scenario. The most important parameter is the difference in clock frequency during a communication session. The difference in clock frequency y is calculated from two or more detected timing offsets ΔT_1 and ΔT_2 between the two parties to be synchronized over a measurement time T_{meas},

$$y = \frac{\Delta T_2 - \Delta T_1}{T_{\mathrm{meas}}}. \tag{5.3}$$

However, a low number of N correlation events gives rise to uncertainty about the location of the correlation peak δT through the total RMS timing jitter σ_0 [HLK09],

$$\delta T = \frac{\sigma_0}{\sqrt{N-1}}. \tag{5.4}$$

Through error propagation, the uncertainty of the difference in clock frequency is obtained from the measurement y_{meas},

$$y_{\mathrm{meas}} = \sqrt{2}\frac{\delta T}{T_{\mathrm{meas}}}. \tag{5.5}$$

Together with Equations 4.1 and 5.4, signal (coincidence) rate r_C and the acquisition time t, is the synchronization jitter due to the uncertainty of the measurement of the peak position,

$$\delta_{\mathrm{FWHM,\ clock\text{-}meas}} = \sqrt{2}\frac{\sigma_0}{\sqrt{r_C t - 1}T_{\mathrm{meas}}}t. \tag{5.6}$$

Both the measurement $\delta_{\mathrm{FWHM,\ clock\text{-}meas}}$ and the clock timing jitter $\delta_{\mathrm{FWHM,\ clock}}$ (Equation 4.11) limit the total achievable synchronization jitter during live tracking,

$$\delta^2_{\mathrm{FWHM,\ sync}} = \delta^2_{\mathrm{FWHM,\ clock\text{-}meas}} + \delta^2_{\mathrm{FWHM,\ clock}}. \tag{5.7}$$

This means that the stability of the clock during the frequency update time and the strength of the quantum signal affect the achievable synchronization timing jitter. The uncertainty of the measurement influences the total timing jitter σ_0, but the precision of the measurement itself is also affected by the device timing jitter. Consequently, when the detection timing jitter is low, the measurement is accurate and has a small contribution to the total timing uncertainty of synchronization. While this is a good model for estimating the physical limits of the synchronization timing error, the timing uncertainty can be much larger in practice, for example, due to interruptions of the link.

5.2.2 The frequency locking algorithm

Random walk and white frequency modulation affect the clock frequency and increase the timing jitter as time passes. This can be avoided with an algorithm for frequency tracking that adjusts the frequency to the master clock. In the following, I will first describe the algorithm with its corresponding optimization. Then I show the performance and compare it with the literature. The algorithm significantly increases the relative timing stability between two communicating parties that have standard quartz oscillators. Interestingly, the timing stability is almost identical to that of free-running rubidium clocks without time transfer at small averaging times of 0.15 s. Although there is some deviation from rubidium clocks in an intermediate region, the performance is again close to that of rubidium clocks at long averaging times (100 s).

The mechanism for limiting the frequency is simple and uses the clock timing offset ΔT as time passes. The difference in clock frequency y over feedback loop time t_f is,

$$y = \frac{\Delta T}{t_f}.$$

(5.8)

Note that the feedback time t_f should be shorter than the averaging time. As a consequence, the compensation mechanism is run several times until the complete data is recorded. This results in small time deviations.

In case of clocked sources that use the modulo operator, the timing offset must not exceed the inverse clock rate (that is, the time window) [7]. For visualization, let us take the example of a faint pulse source [Ma+05] that sends a bit sequence with a clock rate of 500 MHz. This means, every 2 ns a new quantum bit with a specific state is sent to the receiver. When the timing offset changes by 2.5 ns, the bit sequence at the sender no longer matches the received sequence, as its shifted by more than one clock cycle. Consequently, the quantum bit error rate is 50 %. Worse still, the modulo operator cannot find the 2.5 ns timing offset. Instead, it just returns an incorrect (relative) offset of 0.5 ns. In such cases, I recommend varying the timing offset by ±1 or ±2 of the clock cycle and checking the corresponding quantum bit error rate. In our example, adding 2 ns works for recovery. The probability of this effect can be reduced by having a fast feedback loop time t_f that keeps the introduced timing offset low. However, when there is a broken optical link and no signal, the clock frequency cannot be adjusted. This increases the probability of finding such large changes of the timing offset by several clock cycles.

The first step in the algorithm is to process the received data (start-stop cross-correlation with asynchronous sources and the modulo operator for clocked sources). For this, the latest clock frequency is applied (Fig. 5.7**a**). This frequency is out of date by the feedback loop time. The next step is to create the timing distribution of the measured arrival time of single photons, as done through cross-correlations. The envelope is called to have an *a priori* timing jitter, estimated from all previous clock frequencies, but without including the current measurement. On the contrary, the *a posteriori* timing jitter is an estimate of all previous clock frequencies, including the current measurement. These terms are widely used in classical networking for predictive modeling [GN11]. At the same time, the algorithm estimates a correction timing offset, which is the difference between the predicted and measured timing offset, essentially (Fig. 5.7**b,c**). With this, a new frequency is derived and applied to the time stamps of the current data set (Fig. 5.7**d**). This provides a new timing distribution with the *a posteriori* timing jitter (after correction by the current data set). This timing jitter can be very small and can reach almost zero for fast feedback loop times.

The fundamental limit are higher-order timing errors from the acceleration of the clock on even smaller time scales. These errors are also reduced with fast feedback loop times. However, they cannot be zero as the model is based only on a linear prediction (Equation 5.8).

In conclusion, the feedback algorithm reduces residual timing offset by updating the local clock frequency to have a better match with the remote clock.
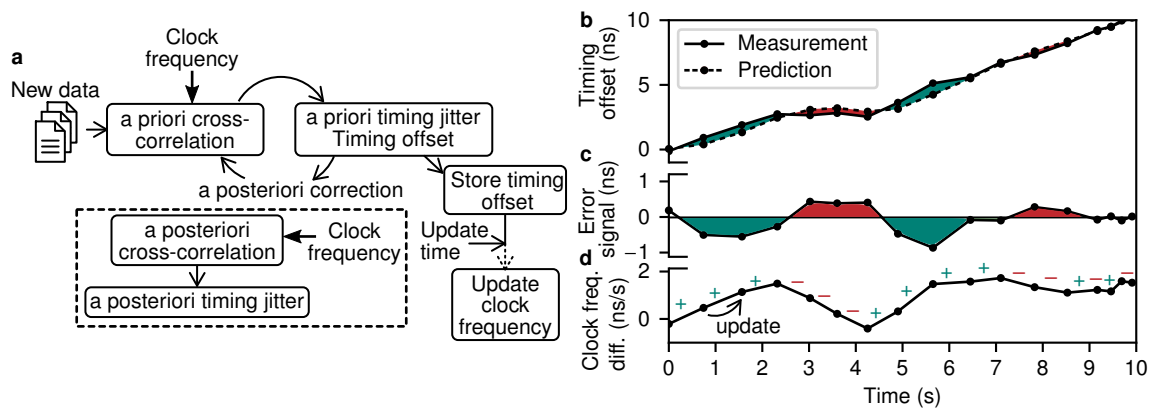

Figure 5.7 | Workflow and application of the live tracking algorithm. a, The timing offset is stored continuously in a buffer. When the clock frequency update time is reached, the software reads the buffer and updates the clock frequency. The timing jitter before and after such a clock frequency update is the *a priori* and *a posteriori* timing jitter, respectively. Note that the *a priori* cross correlation is seeded by the clock frequency of the previous data set. The *a posteriori* cross-correlation function receives the clock frequency of the current data set. **b,** Any deviation of the predicted timing offset from the measured value serves as an error signal, as shown in **c**. This provides an updated correction value for the clock frequency at the receiver (difference in the clock frequency), as depicted in **d**. The figure is taken from my publication [7].

In the final step of the algorithm, two parameters can be used to specify the increase in stability. It can be derived from

1. the timing offset directly, which also serves as an error signal to correct the frequency, or

2. the timing jitter, where the residual timing offset could be calculated from the synchronization timing jitter compared to an ideal reference jitter (Equation 4.10).

When the stability is derived directly from the timing offset, it refers to an out-of-date frequency. This method is also taken by colleagues in reference, e.g. [Cos+20; Lee+19; Qua+22; Wan+21a], and might work well for a fair comparison. However, it does not reflect the performance boost that we obtain by calculating the *a posteriori* correction timing jitter. As this timing jitter also includes the clock frequency of the current data set, it provides a more accurate timing and should be the choice for any time transfer system. It provides a high stability even when the frequency changes throughout the data acquisition, because the average frequency can be extracted. In this way, the corresponding frequency difference is compensated for. The stability limitations mainly stem from residual (higher-order) fluctuations in the clock frequency during data acquisition. The approximate residual timing offset can be estimated by comparing the measured FWHM timing jitter $\delta_{\text{FWHM, meas}}$ with the FWHM reference jitter $\delta_{\text{FWHM, ref}}$ which corresponds to identical clocks,

$$\Delta T^2 = 2\left(\delta^2_{\text{FWHM, meas}} - \delta^2_{\text{FWHM, ref}}\right). \tag{5.9}$$

Note that this estimation is only valid for $\Delta T < \delta_{\text{FWHM, ref}}$ (see Equation 4.10), that is, for small residual timing offsets. The residual timing offset can also be considered as the synchronization timing jitter $\delta_{\text{FWHM, sync}}$ with,

$$\delta_{\text{FWHM, sync}} = \Delta T / \sqrt{2} \tag{5.10}$$

The fundamental limits of the stability are only residual changes in the clock frequency while acquiring data. This residual effect could be reduced by fast feedback cycles that require sufficient signal for high measurement confidence; this is not always the case.

Returning to the application, a low *a posteriori* timing jitter is highly relevant in quantum key distribution systems, as it immediately keeps the error rate low. The downside is a slightly longer computation time than the *a priori* jitter, as the data set takes one more correction. This delay is less of an issue in quantum key distribution systems, as the key extraction runs on its own computation thread, which is less restricted in time.
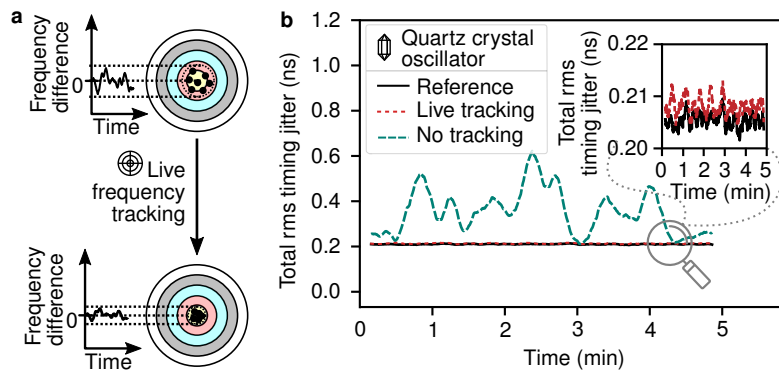

Figure 5.8 | Timing jitter before and after live tracking of the sender clock frequency. a, Tracking of the sender's clock frequency increases the accuracy of stabilization. This high accuracy is a symbol for reduced scatter in archery. **b**, Live tracking of the correlation peak reduces the difference in clock frequency. The clock frequency at the receiver is adjusted every 600 ms in a feedback loop and results in a much smaller total timing jitter that is almost identical to the reference measurement with the same clocks. The synchronization jitter contribution $\sigma_{\text{RMS, sync}}$ is as small as 35 ± 8 ps with acquisition time of 100 ms. The figure is modified from my publication [5].

5.2.3 Optimization and performance

Fast update times of the clock frequency minimize timing jitter and ensure high stability during the communication session. One sign of an increased stability is that the envelope of the timing distribution varies less in its width, that is, the timing jitter fluctuations reduce with the compensation mechanism in place (Fig. 5.8). Here, I measure the stability in terms of the timing jitter. For this, I compare the RMS timing jitter from a Gaussian fit with a reference measurement that uses the same clocks or uses a 10 MHz synchronization signal in an RF cable.

In several 5-minute measurement sessions, the timing jitter and its dependence on the update time were checked. This provides the synchronization jitter $\sigma_{RMS, \, sync}$ being

$$\sigma_{RMS, \, sync}^2 = \sigma_{RMS, \, meas}^2 - \sigma_{RMS, \, ref}^2, \tag{5.11}$$

with $\sigma_{RMS, \, ref} = 39.4 \pm 1.4 \, ps$. There is an almost linear relationship between the synchronization timing jitter and the update time for update times >1 s (Fig. 5.9). This trend is more nonlinear at very fast rates, due to the envelope of the timing distribution that is affected by the frequency difference of clocks (Section 4.3.1). There is a transition from a super-Gaussian function to a standard Gaussian function (Equation 4.5). The timing jitter is even smaller when the correlation envelope is corrected for by the clock frequency of the current measurement. This *a posteriori* timing jitter is always smaller than the *a priori* correction timing jitter, as the *a priori* timing jitter is calculated with an out-dated frequency of the previous data set and excludes the current measurement. The average synchronization timing jitter is only 3 ps and is an order of magnitude smaller than the timing jitter introduced by free-running rubidium clocks in literature with 30-50 ps [Eck+21; Ste+17] (estimated from the residual timing offset variation).
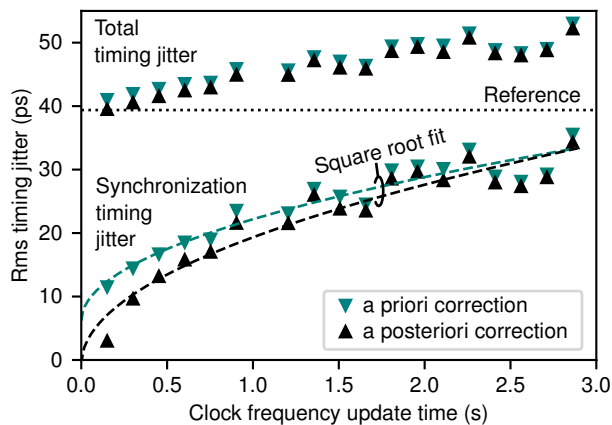

Figure 5.9 | Synchronization timing jitter from varying frequency update times. The figure compares the measured mean root mean squared (RMS) timing jitter from a Gaussian fit with the reference of an ideal clock frequency transfer through an RF cable between source and receiver. The measured synchronization jitter (Equation 5.11) increases with the clock frequency update time as a square root function (see the fits). The *a priori* correction jitters refer to the applied differences in the clock frequency of the previous data set, that is, the last update (Fig. 5.7**a**). *A posteriori* correction refers to timing jitters after applying an updated clock frequency from the current data set. Every data point shows the mean timing jitter in a 5-min measurement session. The sender clock rate is 500 MHz. The receiver detects the signal with single count rates of $(270 \pm 20) \times 10^3$ counts/s and correlation rate of $(160 \pm 20) \times 10^3$ pairs/s with half-width correlation window of 39 ps. The correlation window is equal to the average RMS timing jitter that mainly comes from the single-photon detectors. The algorithm achieves RMS synchronization jitters as small as 3.0 ps with an update time of approximately 150 ms. The acquisition time is 100 ms. The figure is taken from my publication [7].

5.2.4 Stability

The timing stability describes fluctuations in the clock timing offset for a given integration time. For this, the measure is the Allan time deviation [WD08] that is calculated from the variations in the timing offset over time (Fig. 5.10**a**). These variations can be represented by the timing offset error signal that is used to adjust the clock frequency of the receiver (Fig. 5.7**c** in Section 5.2.2). The goal is to find a measure for the stability improvement by time-frequency transfer with single photons. For this, the following scenarios are considered:
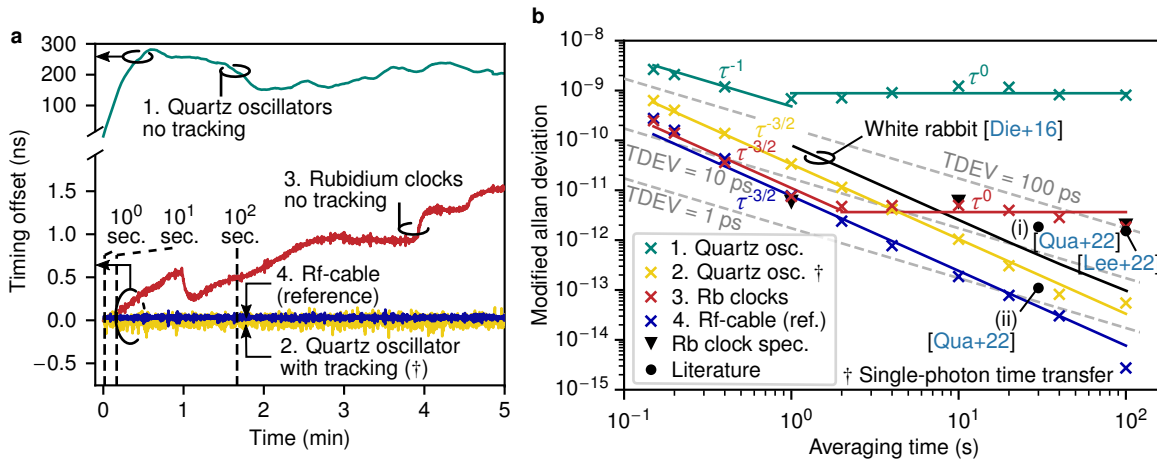

Figure 5.10 | Timing stability measurements. a, Timing offset change for different experimental setups. (1.) Quartz oscillators at source and receiver without updating the clock frequencies (linear component of 15.8 ns/s subtracted after fit). (2.) Quartz oscillators at source and receiver with clock frequency tracking (†). (3.) Free-running rubidium (Rb) clocks at the source and receiver with stability specifications (MDEV) of each being 3×10^{-12} at 1 s, 3×10^{-12} at 10 s and 1×10^{-12} at 100 s. (4.) An RF cable provides the 10 MHz reference output of the source to the receiver. **b**, Modified Allan deviation [WD08], for varying the averaging times. For reference, I included the Allan time deviation (TDEV) in the figure as dotted gray lines (see Table 5.1 for the TDEV of all measurements). The measurements are fit by a linear function to find the noise source that each follows a different power law (τ^0 Flicker FM, τ^{-1} Flicker PM, $\tau^{-3/2}$ White PM). Note that this stability describes the uncertainty of timing offset of the upcoming data set after the wrong prediction of the clock frequency (*a priori* correction). It is directly proportional to the clock instability during the clock update time. TDEV from the literature: two Rb clocks [Lee+22] and (i) Rb clock and H-maser only, (ii) additional microwave frequency transfer for increased stability [Qua+22] and the White Rabbit protocol [Die+16]. The figure is taken from my publication [7].

1. quartz crystal oscillators at the source and receiver *without* tracking of the clock frequencies,

2. quartz crystal oscillators at the source and receiver *with* time-frequency transfer with single photons,

3. free-running rubidium clocks at the source and receiver,

4. the reference with quartz crystal oscillators at the source and receiver, and with time-frequency transfer by a 10-MHz clock signal through an RF cable.

Table 5.1 | Time deviation (TDEV) for varying averaging times τ.

τ (s)	0.15	0.2	0.4	1	2	4	10	20	40	100
1. Rb (ps)	21.5	16.2	8.3	4.3	5.5	11.4	28.7	45.8	65.9	106.2
2. XO (ps)	200	220	240	350	780	2030	7370	13900	19600	44000
3. XO † (ps)	54	46	32	19	13	9.5	6.0	3.5	1.9	3.2
4. Ref (ps)	24.1	18.6	10.0	4.5	2.8	1.8	1.1	0.93	0.75	0.25

The TDEV [WD08] is measured from the residual variation of the timing offset for two rubidium clocks (Rb), crystal oscillators without frequency tracking (XO), crystal oscillators with single-photon frequency transfer (XO †) and the reference measurement (Ref) with two XOs and 10 MHz frequency transfer via an RF cable. The short-term stability of the reference measurement is a bit worse than the measurement with free-running rubidium clocks. This comes from the fact of using quartz oscillators in the reference measurement that have a poor short-term stability in our case. The time deviation with single-photon time transfer (see graphical representation in Fig. 5.10) is much better than what is reported in the literature with highly stable clocks - 88 ps at 100 s averaging time [Lee+22] (two rubidium clocks), 38.1 ps at 30 s averaging time [Qua+22] (rubidium clock and H-maser). When comparing the results of this thesis to classical synchronization schemes, the overall time deviation is identical to the White Rabbit protocol (WR: 11 ps at 1 s and 2 ps at 30 s [SSR18]) or even smaller (WR: 45 ps at 1 s, 15 ps at 10 s and 6 ps at 100 s [Die+16]).

The reference is an idealized frequency carrier between the two clocks and acts as the ground truth. The clock frequencies are locked by a common 10-MHz signal. With this in place, it is easily possible to achieve femtosecond time deviations by only 100 s integration time (Fig. 5.10). It is much harder to achieve high stability with a standard crystal oscillator, as they indicate several hundreds of picosecond time deviations at integration times of 1 second (Table 5.1). Rubidium oscillators have only a few picosecond time deviations. However, when frequency tracking mechanisms are applied, the performance improves drastically. In particular, the timing uncertainty with crystal oscillators at small integration times <1 s is only 19 to 54 ps now - this is sufficient for high-bandwidth quantum key distribution systems. Note that the actual synchronization timing jitter is even smaller and lies at 3 ps (Fig. 5.9). At longer integration times (100 s), the variations average out and the time deviation reaches 3.2 ps. This is an improvement of more than 4 orders of magnitude in contrast to crystal oscillators without single-photon time transfer and shows the high performance of the frequency tracking algorithm.

Compared to the White Rabbit protocol for high-precision time transfer [Die+16; SSR18], the timing stability is very close to or even better. This comes from having a fast feedback algorithm. Note that there is an important difference in implementation. This thesis essentially only considers the stability of the photon arrival times where both the clock and the link itself contribute. However, the White Rabbit protocol refers only to the stability of the clocks and isolates it from the contribution of the link, which is technically more challenging. It is achieved by a two-way time transfer protocol [Gio+13] that is straightforward to implement with single photons as well [Hon+22; Hou+19; Qua+22; Xia+22].

The introduction of single-photon time transfer successfully reduces the frequency mod-

ulation noise (Flicker FM) until mainly white phase modulation noise is present (Fig. 5.10). Essentially, there remain only random fluctuations of the timing offset that also exist in the reference measurement but with a different magnitude. These fluctuations come from the timing jitter of the system, but also from the intrinsic phase noise of the quartz oscillators. By the reduction of the system timing jitter, e.g. taking detectors higher timing accuracy, the white phase modulation noise reduces. However, the presented optical transfer system includes single-photon detectors with tens of picosecond timing jitter [QUA22; Qua22] which could explain the difference in stability with respect to the reference. The reference is based on a purely electrical time transfer system (RF cable). The electrical components used can have timing jitters of just a few picoseconds [Gmb22; Ins22], resulting in better overall timing stability.

In contrast to rubidium clocks, we find a strong improvement at longer integration times. Free-running rubidium clocks miss an external reference and do not have a feedback mechanism to lock their oscillators. Such an external global reference could be, for example, a GPS clock. The missing reference gives rise to a lot of frequency modulation noise (Flicker FM) at longer integration times (> 1 sec), as the frequencies no longer match. The behavior is observed impressively in the recording of the timing offset that drifts (Fig. 5.10 **a**). In contrast, these drifts are not observed when transferring the time via single photons. This gives a great advantage of single photons as a mediator for high-performance synchronization, in particular at long averaging times.

5.3 Application to deployed link scenarios

The algorithms for clock synchronization are applied to real link scenarios. The first section covers in-lab experiments with an emulated turbulent free-space link (experiment ID: A1). The atmospheric turbulence is introduced through a rotating phase plate, designed by Andrej Kržič to represent an atmospheric link to a satellite from the Mt. Teide optical ground station (the Fried parameter is 1 mm with a $1/e^2$ full-width beam waist of 3.4 mm [Gar+11]). The rotating phase plate has a nonuniform refractive index (or phase) profile that corresponds to the Kolmogorov model of turbulence [AP05]. The rotation continually changes the spatial phase of the beam as it happens in real atmospheric turbulence. The second section describes experiments on a 1.7 km intra-city free-space link (experiment ID: A2), as well as on a 70 km fiber link Jena and Erfurt (experiment ID: B2).

With respect to the time line, the first experiments took place with an entangled photon source that is driven by a continuous-wave laser to generate photon pairs at 810 nm in the lab (ID: A1, Fig. 5.11, summary in Table 5.2). Later, the experiments have been extended to an actual free-space link with the receiver not being in the same lab (ID: A2). In consequence, this gives rise to an intrinsic time delay that slows down the feedback mechanism for synchronization
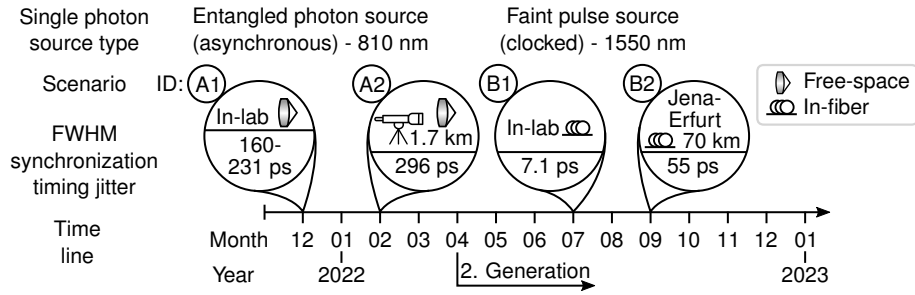
Figure 5.11 | Experimental time line. The first experiments considering real-life aspects took place in December 2021 with an emulated free-space link and a continuous-wave-driven (asynchronous) entangled photon source. Later, the scheme was applied to an actual 1.7 km intercity free-space link. The second generation of the synchronization mechanism has been evolving throughout the year 2022 with experiments with a faint pulse source. After in-lab experiments (last Section 5.2.2), the schemes have been applied to the actual fiber link between Jena and Erfurt. Details of the experimental setups in Table 5.2.

Table 5.2 | Experimental systems to cover different application scenarios.

ID	Date	Scenario	Alg.	Source	T-trans.	SPD	$\delta_{\text{FWHM, sync}}$ (ps)
A1	12/2021	In-lab, emu. FS	1G	EPS	No	AV	160-231
A2	02/2022	Depl., FS	1G	EPS	Yes	AV	296
B1	07/2022	In-lab, fiber	2G	WCS	No	Nano	7.1
B2	09/2022	Depl., fiber	2G	WCS	No	Nano	55

The scenarios A1, A2, B1 and B2 are covered in the Sections 5.3.1, 5.3.2, 5.2.2 and 5.3.2, respectively. The experiments took place in deployed (depl.) free space (FS), emulated free space (emu. FS), or in-fiber. There was an update of the synchronization algorithm (Alg.) from first (1G) to second generation (2G) in summer 2022 that increased the performance. Continuous-wave driven entangled photon sources (EPS) require a transfer of time stamps (T-trans.) when the receivers are not located in the same lab. This classical transfer is done via an RF antenna, which is not required with pulsed weak coherent sources (WCS, different term for faint pulse source). Classic transfer slows the clock frequency update time and increases the synchronization timing jitter ($\delta_{\text{FWHM, sync}}$). Furthermore, the choice of single-photon detectors (SPD) plays a role, i.e. whether avalanche-based SPDs (AV) or low-jitter nanowire detection systems (Nano) are in place. Nanowire-based SPDs increase the synchronization performance.

and increases the timing jitter, as the time stamps have to be shared with the sender. Then, I developed an enhanced second-generation synchronization mechanism and applied it to faint pulse sources at 1550 nm (ID: B1 and B2).

5.3.1 Emulated free-space link experiment

The objective of the in-lab emulated free-space experiment (ID: A1) is to test the synchronization performance under strong signal fluctuations in a controlled environment. In use is an entangled photon source that is based on spontaneous parametric down-conversion and generates photon pairs at 810 nm. The following scenario is emulated: one photon is kept at the source and the other one is sent to a distant receiver. On the way to the receiver, the photons experience three factors that degrade the performance (Fig. 5.12):

1. additional noise (represents the day light noise),

2. fluctuations of the link transmission efficiency (represents atmospheric turbulence on the free-space link), or

3. a blocked link (represents obscuration of the link by, e.g. birds, lost alignment lock of the telescopes).

The start of the synchronization algorithm is particularly challenging, as the source operates in asynchronous mode. As part of the initialization of the synchronization, data is acquired and saved. The next step is the search of the clock frequency by several cross-correlations (frequency tuning) as required for low-precision crystal oscillators. As described above (Chapter 4), a sufficient signal is necessary, and even more so in the case of asynchronous single-photon sources. However, this is not always the case because of atmospheric turbulence that affects link transmission. The turbulence alters the wavefront, which complicates the coupling of light back into fiber at the receiver. This could make it necessary to process several data packages at different times until a sufficiently strong signal is found. The overall performance is a FWHM synchronization timing jitter of 160 ps with single-photon count rates at Alice, Bob, and the correlation rate is $(15 \pm 5) \times 10^3$ counts/s, $(195 \pm 3) \times 10^3$ counts/s and 440 ± 200 pairs/s, respectively.

Let us discuss the impact of all the factors on this synchronization timing jitter.

Additional noise ,such as day light noise, reduces the signal-to-noise ratio until the correlation peak disappears. This is critical for the tracking algorithm, as the chances increase that a noise peak is wrongly identified as the correlation feature. As a consequence, an error frequency is calculated, or the frequency lock may become lost. For this reason, I introduced a signal-to-noise ratio threshold (coincidence-to-accidentals, CAR threshold) that I selected to be 5. This is a compromise between keeping the frequency tracked even at a low signal-to-noise ratio and not losing the lock due to a faulty identification of a peak. Note that with such strong noise signatures (CAR of 5), synchronization is still possible, but the quantum key distribution would no longer be. Thus, the live tracking algorithm works over the full dynamic range, where a quantum key distribution is also possible.

Intensity fluctuations ,due to atmospheric turbulence, leading to fluctuations in the signal-to-noise ratio. Similarly to the case of additional noise, the correlation peak is not estimated with sufficient resolution. This reduces the resolution of the tracked clock frequency and increases the timing jitter. The introduction of a CAR threshold may cause the system to stop frequency tracking. However, this is much easier to handle than a faulty calculation of the clock frequency, which may require a restart of the full system.

At very low signal-to-noise ratios, live tracking is still possible, even for a CAR 10 ± 4 that is close to a long-distance link between the Canary Islands (140 km) [Eck+21]. In such cases, the

CAR is below the tracking threshold of 5 sometimes, which results in a lost frequency reference, i.e., the tracking is no longer possible (Fig. A.2). However, since this happens only for short times, this results in only small frequency differences between clocks that slightly increase the FWHM synchronization timing jitter to 231 ± 14 ps. In contrast to live tracking, the initialization of the clock synchronization is very difficult here without knowing the approximate clock frequency. The initialization would not be possible when the normalized frequency is uncertain in a range between -20 μs/s and +20 μs/s (1 μs/s = 1 ppm), as typical for crystal oscillators. In this case, it is necessary to narrow the search range with the help of previous measurement sessions or to initiate with a better signal-to-noise ratio.

Blocking the link results in the signal dropping to zero, causing the frequency tracking algorithm to stop. As a consequence, the frequency difference between the clocks increases and causes a timing offset when the signal returns. The timing offset ΔT between the two clocks comes from its individual integration of the frequency and phase noise components up to the time t (Equation 2.6 in Section 2.3),

$$\Delta T(t) \approx \int_0^t y_A(t')dt' + w_A(t) - \int_0^t y_B(t')dt' + w_B(t), \tag{5.12}$$

with the frequency deviation and other white noise of clocks A, B being $y_{A,B}$ and $w_{A,B}$, respectively. Large-frequency noise (as in crystal oscillators) gives rise to a large timing offset. The same happens when the link is blocked for long periods of time. The algorithm finds such a high timing offset (here: 580 ns) only when the observation window is large enough. This is the reason why I included an adaptive observation window. The observation window is automatically increased when the signal is lost to still find the correlation peak. When the link is blocked for even longer time (minutes), a new initialization may be required by FFT-cross correlations or frequency sweeps (in case of very low signal and crystal oscillators).

In conclusion, noise increases the synchronization timing jitter due to the larger uncertainty during a measurement (Equation 5.7). Furthermore, when the noise is so high that the CAR is smaller than the threshold, the frequency tracking stops, and the timing jitter rises. In the following section, the algorithm developed is applied to a real intercity link experiment. Here, another contribution plays a role; as the receiver is remote, the time stamps have to be transferred classically to a common computer to calculate the cross-correlation.
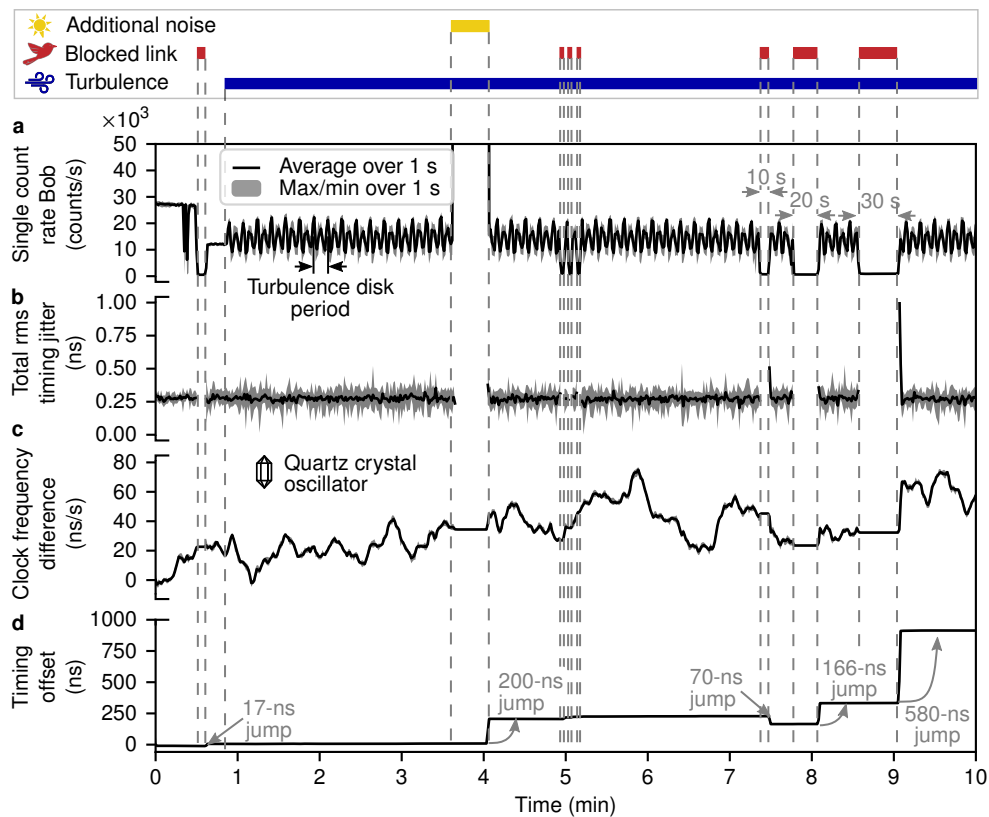
Figure 5.12 | In-lab emulated free-space link experiment. At different times I add additional noise at Bob's receiver, block the optical link, or add atmospheric turbulence (Fried parameter 1 mm, $1/e^2$ full-width beam waist of 3.4 mm). **a**, Single count rate at receiver Bob with an initial drop to 15×10^3 counts/s after inserting the turbulence disk. The mean single count rate is $(15 \pm 5) \times 10^3$ counts/s with coincidence rate of 440 ± 200 pairs/s (coincidence window is equal to the RMS timing jitter of 269 ps) in the time window from minute 1 to 3.5. The count rate in Alice is constant at $(195 \pm 3) \times 10^3$ counts/s. The introduction of a noise source increases Bob's count rate to 6 Mcps. The low signal-to-noise ratio stops the correlation peak tracking and keeps the clock frequency at the receiver Bob constant. **b**, The time-dependent total timing jitter root mean squared (RMS) remains constant even after switching on the atmospheric turbulence at minute 1 - only the fluctuations increase. The timing jitter probability distribution describes a Gaussian with its fitted center at 268.7 ± 0.7 ps (minute 1 to 3.5). Setups with the same clock (perfect synchronization) show timing jitters of 260 ± 2 ps from a fit to 10 s of data acquisition, estimating the synchronization jitter RMS to 68 ± 8 ps. **c**, The tracking algorithm is stopped in regions with low signal-to-noise ratios (blocked optical link or additional noise) and results in a constant clock frequency skew for correction there. **d**, The timing offset jumps after time intervals with low signal-to-noise ratio, as the correlation peak is not tracked and the clock frequency is not adjusted. This phenomenon is stronger for longer blocked links. The timing offset varies within a window of ±1 ns on time scales of 30 s. The feedback loop time and the size of the data package are 200 ms and 100 ms, respectively. The figure is modified from my publication [5].

5.3.2 Deployed link experiments

The first experiment is a free-space experiment (ID: A2) that builds on developments in laboratory conditions under emulated turbulence of the atmosphere. The experiment is performed with an entangled photon pair source at 810 nm for a polarization-encoded quantum key distribution with avalanche-based single-photon detectors. The total timing jitter δ_{FWHM}, excluding the timing jitter for synchronization, is 715 ± 5 ps with the contribution of a single-photon detector (SPD), analog-to-digital converter (ADC) and a single-photon source (SPS), $\delta_{\text{FWHM}}^2 \approx 2\delta_{\text{FWHM, SPD}}^2 + 2\delta_{\text{FWHM, ADC}}^2 + \delta_{\text{FWHM, SPS}}^2$. The second experiment is on the fiber link between Jena and Erfurt (ID: B2). The fiber introduces time-dependent polarization changes that affect the error rate. For a full demonstration of quantum key distribution, the compensation of the change in polarization is required. This was, however, not yet implemented here. This is the reason why a time-phase-encoded faint-pulse source (at 1550 nm) is used, where the key rate is independent of the polarization. The total FWHM timing jitter, excluding (!) the synchronization timing jitter is 98.0 ± 2.8 ps and almost one order of magnitude better than in the free space setup. This is mainly due to the nanowire single-photon detectors that have lower timing jitter, which will give much higher precision for measuring the clock frequency and an improved synchronization performance.

A. 1.7 km free-space intracity link experiment with an entangled photon source

The intracity link experiment took place at a very early stage of research and has been part of the QuNet project [1]. The goal was to establish the infrastructure for the distribution of quantum keys on a 1.7 km free-space link (Fig. 5.13**a**). Over the following months, the algorithms improved and the synchronization performance could be increased. With this being said, let us start with the results and then elaborate on what can be improved. The synchronization timing jitter amounts to $\delta_{\text{FWHM, sync}}$ = 297 ± 19 ps (Fig. 5.13**b-d**). This is a bit worse than the counterpart emulated in the lab with a synchronization timing jitter of $\delta_{\text{FWHM, sync}}$ = 160 ± 19 . . . 231 ± 14 ps.

The major challenge for clock synchronization in this application scenario is the large physical distance between the sender and the receiver. The bottleneck is the classical communication link that transfers the time tags from the receiver back to the sender to perform the correlations. Furthermore, the classical link sometimes breaks. This delay increases the frequency update time and increases the timing jitter. In addition, the single-photon source and both receivers have much worse environmental control than in-lab. Poor air conditioning or vibrations affect the system, as there is no optical table. In particular, crystal oscillators are very susceptible to the environment and change their frequency rapidly (Fig. 2.7 in Section 2.4). The outlook for this experiment is to improve the classical communication channel to achieve faster frequency update times and to upgrade the post-processing algorithm.
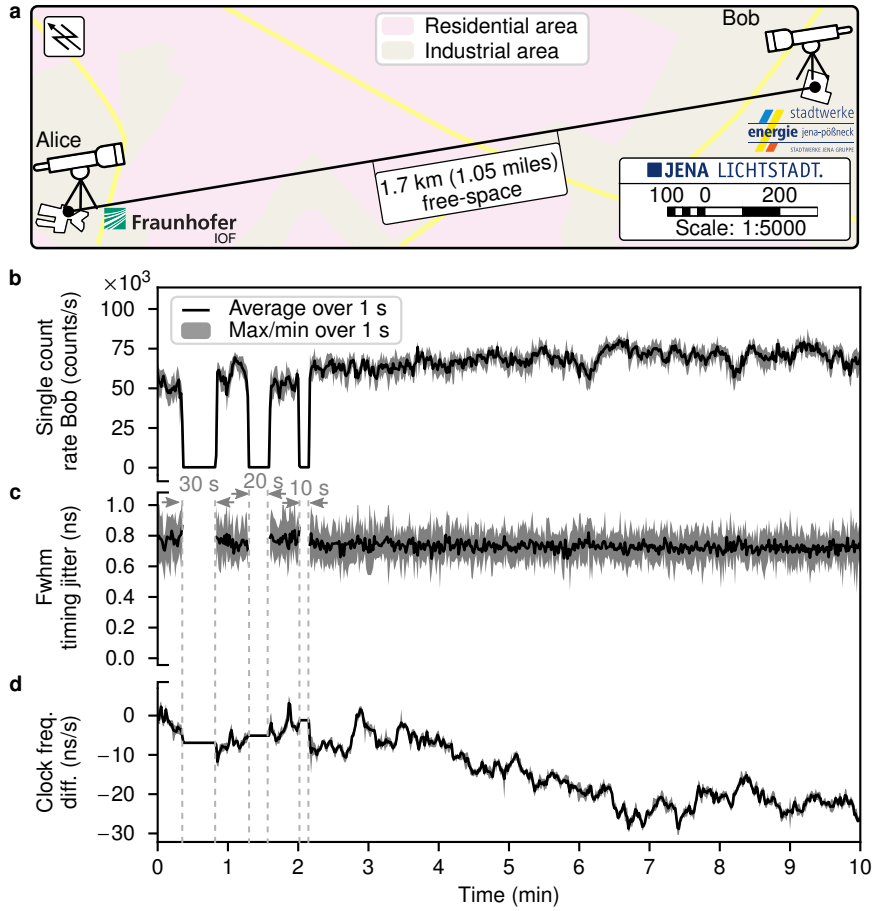
Figure 5.13 | Measurement session on the turbulent free-space link. a, The entangled photon pair source is situated at the same place as the receiver Alice. Here, one photon is measured locally. The other photon is sent to the receiver Bob through the free-space link. The time stamps at the receiver Bob are sent back to Alice for processing via an antenna. The experiment took place on 14 February 2022 at 8:30 pm (after sun set). Residential and industrial areas indicate different concentrations of particulate pollution [BM10] and industrial exhausts may have a stronger contribution to the total atmospheric turbulence. The map is modified from Ref. [Lic21]. **b**, The synchronization works reliably even with interruptions of the optical link by 10 s, 20 s or 30 s. The single count rate at the receiver Alice and Bob is $r_A = (322 \pm 2) \times 10^3$ counts/s and $r_B = (69 \pm 6) \times 10^3$ counts/s, respectively. The number of correlations over a coincidence window equal to the RMS timing jitter is $r_C = (1.2 \pm 0.2) \times 10^3$ pairs/s. **c**, The timing jitter is measured from the mean value of a Gaussian fit to the timing jitter distribution over time. The total displayed timing jitter is $\delta_{\text{FWHM}} = 774 \pm 6$ ps. This provides a synchronization timing jitter of $\delta_{\text{FWHM, sync}} = 297 \pm 19$ ps with the reference timing jitter (same clock) of $\delta_{\text{FWHM, ref}} = 715 \pm 5$ ps. **d**, The clock difference is tracked reliably except when the link is interupted.

B. 70 km fiber intercity link experiment with a faint pulse source

The link experiment between Jena and Erfurt is done with a faint pulse source at 1550 nm. The clocked single-photon source is located in Jena, and the measurement took place at the receiver in Erfurt (the setup is identical to Fig. 5.3). The clocked operation is beneficial not only due to its low computational effort through the modulo operator (Section 4.6), but also from a classical communication perspective. Data are not transferred over a communication channel for synchronization. The receiver only requires the repetition rate of the source, which is 500 MHz in our setup. The exact clock frequency is derived during the initialization of the synchronization. In the actual synchronization session, the receiver adjusts its frequency to match the sender frequency. In practice, this is done by adjusting the frequency that is put as the divisor in the modulo operation. This means that it is possible to perform all clock synchronization without any communication effort between the source and the receiver. Although I have not implemented it, clock synchronization could run on a separate (high-speed) computation thread that is independent of the quantum key distribution thread. This would result in unmatched small synchronization timing jitter and very high timing stability.
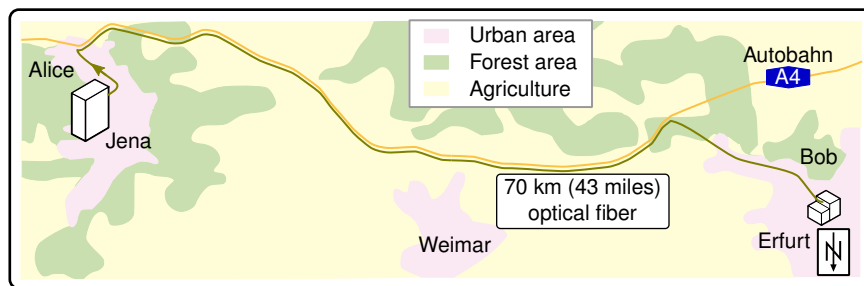

Figure 5.14 | Optical fiber link experiment. The clocked single-photon source is based on weak coherent states and is located in Jena (Alice). The single-photon states are sent to the receiver in Erfurt (Bob) through a 70 km long optical dark fiber that is not used for classical data transfer. The dispersion for a length $z = 70$ km amounts to $z\beta_2 = 1600 \, \text{ps}^2$ at 1550 nm. The total losses are approximately 21 dB. The phase and polarization of light is stronger influenced in urban areas and close to highways, as, e.g., moving vehicles introduce vibrations or heat expands the fiber. Forest areas are known for their much lower temperature [Sch+21]. The map is modified from Ref. [Lic21].

The clock frequency is tracked by observing the $|\text{Early}\rangle$ and $|\text{Early}\rangle$ pulses in the time base. When the timing offset error between the estimated and measured values exceeds the symbol range ($0\ldots 2$ ns with an average frequency of 500 MHz), the frequency tracking is stopped (Fig. 5.15**a**). Otherwise, the calculated frequency is incorrect (see Section 5.2.2). This stopped frequency tracking gives rise to an increase in timing jitter, as observed in the experiment (Fig. 5.15**b**). Such large timing jitters also lead to higher uncertainties in the measured clock frequency. This situation can be avoided by accelerating the computation time. Hence, the frequency update time is shorter, and the timing offset error is reduced.

The performance of the synchronization session with crystal oscillators is tested by comparing it to rubidium clocks at both the source and the receiver that act as an ideal reference (Fig.
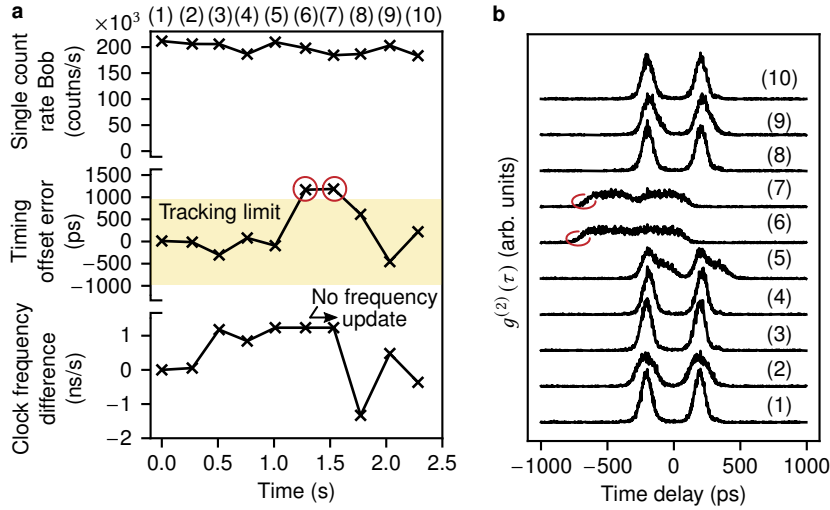
Figure 5.15 | Tracking the clock frequency with single photons. a, The clock frequency is adjusted constantly as long as the timing offset error does not exceed $1000\,\text{ps}$. This value originates in the symbol range of 0 to 2 ns for the quantum key distribution. **b**, When the tracking limit is exceeded, this leads to an increase in timing jitter of the arrival time histogram $g^{(2)}(\tau)$ (numbers (6) and (7)).

5.16). The FWHM timing jitter with free-running rubidium clocks is $\delta_{\text{FWHM, Rb}} = 98.5 \pm 2.8\,\text{ps}$. The timing jitter is increased by a bit because of a small frequency mismatch between the two independent rubidium oscillators. The frequency mismatch y is easily derived from the average change in timing offset ΔT over time t and is $y = \Delta T / t = 136\,\text{ps/s}$ (Equation 4.1). When subtracting this, the reference timing jitter $\delta_{\text{FWHM, ref}}$ over an integration time of $t = 0.1\,\text{s}$ is then (see Equation 4.10),

$$\delta^2_{\text{FWHM, ref}} = \delta^2_{\text{FWHM, Rb}} - \frac{1}{2}(yt)^2, \tag{5.13}$$

giving a value of $\delta_{\text{FWHM, ref}} = 98.0 \pm 2.8\text{ps}$ for frequency-corrected rubidium clocks. With the reference timing jitter, it is possible to obtain the synchronization timing jitter $\delta_{\text{FWHM, sync}}$ from the measured timing jitter with crystal oscillators $\delta_{\text{FWHM, XO}} = 112.2 \pm 30.9$,

$$\delta^2_{\text{FWHM, sync}} = \delta^2_{\text{FWHM, XO}} - \delta^2_{\text{FWHM, ref}}. \tag{5.14}$$

This brings us to a mean synchronization timing jitter of $\delta_{\text{FWHM, sync}} = 54.6\,\text{ps}$ with only crystal oscillators.
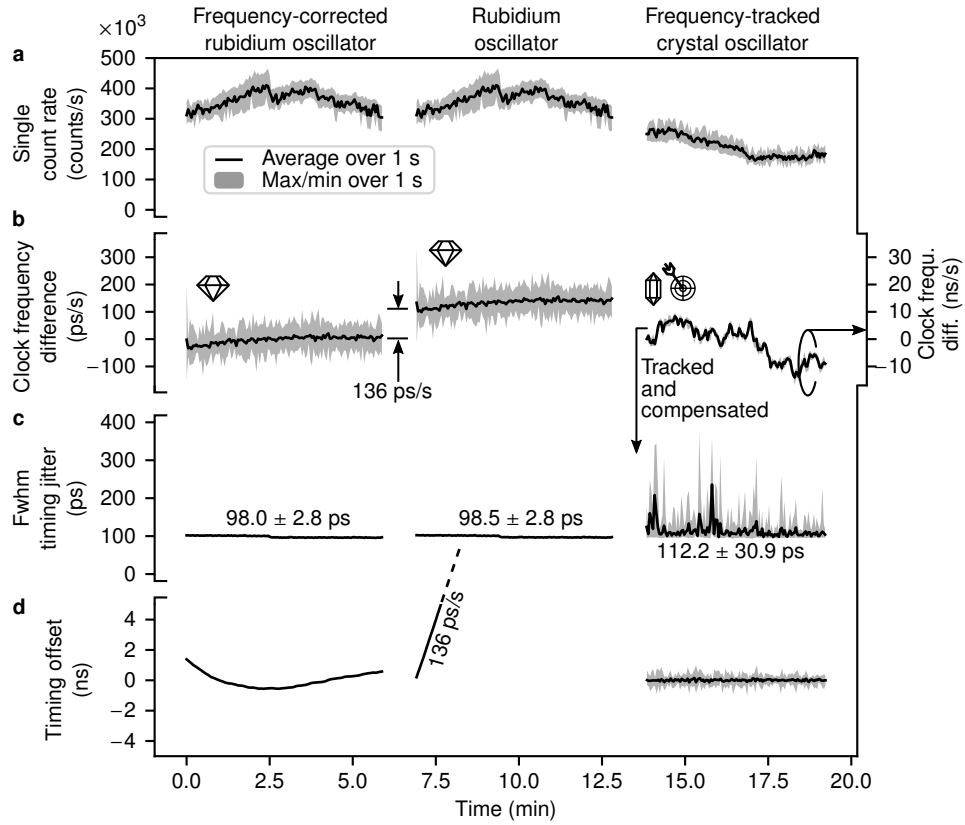
Figure 5.16 | Measurement session on the 70 km fiber link. The first measurement is the reference. For this, I take the data from rubidium oscillators and correct them for their frequency mismatch. Subsequently, crystal oscillators are in use, and the frequency is tracked by using single photons. **a**, The single-photon count rate at the receiver. With crystal oscillators in place, the received count rate is $r_B = (360\pm40)\times10^3$ counts/s and the correlation rate of the $|\text{Early}\rangle$ time bin $r_C = (105\pm14)\times10^3$ counts/s. The signal with quartz oscillators is reduced because of natural changes in the polarization of light that reduce the detection efficiency of the single-photon detectors. **b**, The difference in clock frequency of the two crystal oscillators is more than two orders of magnitude larger with the rubidium oscillators. **c**, The full width at half-maximum (FWHM) timing jitter is measured from a Gaussian fit to the arrival time histogram. The values in the figure represent mean values with its standard deviation. **d**, The timing offset of rubidium oscillators is reduced to a range of 2 ns when correcting for its frequency difference of 136 ps/s. Notably, in the same range lies the timing offset with frequency-tracked crystal oscillators, although its frequency varies much more. The integration time of the data points is 100 ms.

The stability. The stability on the 70 km fiber link is reduced in contrast to its in-lab counterpart, due to longer frequency update times, fiber dispersion, and run-time fluctuations of the single photons (Fig. 5.17 and the corresponding Table 5.3). The greatest impact comes from the longer frequency update time, which has increased from 150 ms to almost 300 ms.

The second influence originates in the fiber dispersion that increases the timing jitter, since no dispersion compensation module is in place. I measured the dispersion by a round trip to Erfurt and back (2×70 km). The dispersion increases the pulse width of an input pulse with an FWHM width of $\delta_{\text{FWHM, in}} = 58.9$ ps to $\delta_{\text{FWHM, out}} = 98.8$ ps when it is back in Jena. The following equation provides the group delay dispersion $z\beta_2$ for $z = 140$ km of fiber [Gov07],

$$\delta_{\text{FWHM, out}}^2 = \delta_{\text{FWHM, in}}^2 + \left(2\sqrt{2\log_e 2}\right)^4 \left(\frac{z\beta_2}{4\delta_{\text{FWHM, in}}}\right)^2, \tag{5.15}$$

with $z\beta_2 \approx 3370$ ps^2. This matches almost the dispersion characteristics of standard SMF-28 fiber [Inc22] that would give rise to 3200 ps^2. The one-way dispersion from Jena to Erfurt is only ≈ 1700 ps^2 and would increase the intrinsic timing jitter of the single-photon source from $\delta_{\text{FWHM}} = 58.9$ ps to 71.2 ps. As a consequence, the total timing jitter increases from $\delta_{\text{FWHM}} = 92.7$ ps to a measured reference jitter of 98.0 ps (there are also small timing jitter differences arising from nanowire single-photon detectors). This increase in timing jitter is almost negligible and has a small impact on synchronization performance (Equation 5.6) considering the high correlation event rate of several tens of kcps.

The third reason for poor stability comes from variations of the run-time of the single photons, as the fiber changes its refractive index and geometry due to temperature. The phase change can be described by a geometric change in the fiber length L and its refraction index n with temperature T for the wavelength λ [Ele+18],

$$\Delta\phi = \frac{2\pi}{\lambda}\left(n\frac{\partial L}{\partial T} + L\frac{\partial n}{\partial T}\right)\Delta T. \tag{5.16}$$

The thermo-optic coefficient $\epsilon = \partial n/\partial T = 11 \times 10^{-6}\,\text{K}^{-1}$ is at least one order of magnitude higher than the thermal expansion coefficient $\alpha = \partial L/\partial T = 0.55 \times 10^{-6}\,\text{K}^{-1}$ for the core of silica glass [Tao+13; Wan+22]. When applying Equation 5.16 to 70 km of fiber, a change of

Table 5.3 | Time deviation (TDEV) with crystal oscillators that have single-photon time-transfer applied.

Averaging time (s)	0.4	1	2	4	10	20	40	100
TDEV, in-lab	32	19	13	9.5	6.0	3.5	1.9	3.2
TDEV, deployed Jena-Erfurt	175	115	76	46	26	19	12	5.9

The table compares the stability of the experiment in-lab (Fig. 5.10) with the 70 km intercity link (Fig. 5.17). The reference timing jitters are comparable and amount to $\delta_{\text{FWHM, ref}} = 92.7 \pm 3.3$ ps (in-lab) and $\delta_{\text{FWHM, ref}} = 98.0 \pm 2.8$ ps (intercity link). The main difference is that the frequency update time is 150 ms (in-lab) and 300 ms (intercity link). The update time is longer, as a quantum key distribution session was run on the same computation thread as the synchronization.

temperature by $\Delta T = 1\,\text{K}$ gives rise to a time delay of 2.6 ns at 1550 nm. As the temperature changes slowly, it affects the timing offset stability at longer averaging times when it is not compensated. This is visible by a poor Allan deviation, although rubidium oscillators are in place. However, by using the single photons as a time-frequency carrier, this effect can be mitigated and provides high stability.
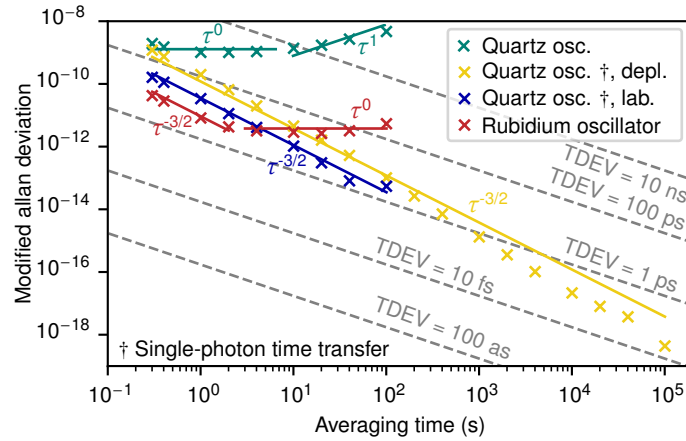

Figure 5.17 | Timing stability measurement on the 70 km fiber link. The stability is measured from the residual timing offset variation that serves as the error signal to adjust the receiver clock frequency. The stability with standard crystal oscillators is improved with a single-photon time-frequency transfer on the deployed link (†, depl.). This is compared with a measurement with two free-running rubidium oscillators at the sender and receiver sites. Furthermore, the figure includes the stability of the measurement in the laboratory (Fig. 5.10). The stability with rubidium oscillators reduces with longer averaging times (> 100 s), which could be a consequence of photon run-time fluctuations, because of the long fiber. This is compensated for by using single-photon time transfer, which gives rise to a very low time deviation down to femtoseconds at integration times of 1000 seconds on the deployed link. The measurements are fit by a linear function to find the noise source that each follow a different power law (τ^1 frequency drift, τ^0 Flicker FM, $\tau^{-3/2}$ White PM). The crosses represent interpolated data points that are summarized in Table 5.3.

5.4 Discussion and Conclusions

As a summary of the experiments, the following elements increase the synchronization performance:

1. increase the high signal-to-noise ratio (high link transmission),

2. pulse the single-photon source (clocked operation mode),

3. minimize classical data transfer - this can be close to zero for the computation thread dedicated to synchronization in clocked single-photon sources,

4. take an isolated computation thread for the synchronization calculations,

5. reduce the timing jitter of single-photon detectors,

6. introduce fault-tolerant algorithms to find the timing offset (peak finder).

In the following, I will describe these factors and how they impact(-ed) the synchronization performance.

Low **signal-to-noise ratios (1.)** in long-distance links reduce the significance of the correlation peak. It is further reduced when crystal oscillators with weak frequency precision are in place. This combination of a poor frequency precision and low signal is a potential setting where synchronization is no longer feasible, and applies to asynchronous sources in particular. On the contrary, synchronization could be feasible with **clocked single-photon sources (2.)**. In the initialization, the clock frequency can be found with almost three orders of magnitude higher precision (Fig. 4.22) as the computation time is much lower (Fig. 4.21). This substantially increases the signal-to-noise ratio. The low computation time also increases the refresh rate of the frequency in the live tracking. As a consequence, the timing jitter is kept low.

Any delay in **classical data transfer (3.)** increases the update time of the clock frequencies and results in a clock frequency mismatch that increases the timing jitter. This has been a critical factor in the free-space setup (ID: A2), where the time stamps have been transferred from the remote receiver back to the sender. The sender incorporates a computer to calculate the cross-correlation between the received time tags. In consequence, the feedback signal for adjusting the clock frequency is only delivered after receiving the time tags and calculating the cross-correlation. In contrast, the experiments with a clocked single-photon source (ID: B1 and B2) did not require any classical data transfer. The receiver only needs the source repetition rate and can extract the source clock frequency by using only its own time stamps. This avoidance of data transfer with clocked single-photon sources reduces the timing jitter.

In the same direction, there is the introduction of a **second computation thread (4.)** for synchronization to increase the update frequency. In particular, it is useful when additional calculations are required for the quantum key distribution protocol. This has not been implemented in the quantum key distribution experiments (ID: A2, B2), but it will be in the future.

Single-photon detectors (5.) with low timing jitters provide high precision of the clock frequency. The clock frequency is derived from the timing offset of the correlation peak over time. Any error in timing offset directly propagates to an error in clock frequency that lowers the synchronization performance. This gives lower synchronization timing jitters when nanowire single-photon detectors are in place (as in the scenario ID: B1 and B2). Likewise, **the algorithm to find the timing offset (6.)** also has a major impact. The algorithm has to find the correlation peak correctly (peak finder). Otherwise, the derived clock frequency is wrong. The peak finder algorithm has been updated in scenarios B1 and B2. As a consequence, the synchronization performance is enhanced.

Table 5.4 | Timing jitter of the tested scenarios.

ID	Scenario	$\delta_{\text{FWHM, sync}}$ (ps)	Δ (%)
A1	EPS, in-lab, emulated free-space link	$160 \pm 19 \ldots 231 \pm 14$	$+3.3 \cdots +6.4$
A2	EPS, deployed, free-space	297 ± 19	$+7.6$
B1	WCS, in-lab, fiber	$7.1 \pm$ n.a.	$+0.3$
B2	WCS, deployed, fiber	$54.6 \pm$ n.a.	$+12.6$

The synchronization timing jitter $\delta_{\text{FWHM, sync}}$ is displayed for scenarios with an entangled photon pair source (EPS) or weak coherent source (WCS). The experiments take place in-lab with an emulated free-space link (A1), on a 1.7 km intercity free-space link (A2), in-lab in fiber (B1) or on a deployed 70 km fiber link between Jena and Erfurt (B2). This synchronization timing jitter increases the original timing jitter (perfect synchronization with the same clock) by some percent (Δ).

The developed synchronization methods with single photons successfully made its way out to real link experiments to enable quantum key distribution with a minimum of hardware overhead. The synchronization timing jitter reaches 7.1 ps (FWHM) with fast feedback loops of 150 ms for adjusting the clock frequency. This corresponds to an increase of the timing jitter with the same clocks (the reference) by only 0.3 % (Table 5.4). The stability is comparable to state-of-the-art synchronization experiments with rubidium oscillators (Table A.2). Note that the stability with rubidium clocks is significantly higher. In consequence, the experiments in the literature can afford lower count rates of the single photons. I confirmed such a high synchronization performance not only in the lab, but also on a 1.7 km turbulent free space and 70 km intercity fiber link. The increase in total timing jitter is very small and amounts to only 12.6 % with respect to an ideal synchronization scheme. This indicates only a small contribution of the single-photon-based synchronization to the total system jitter. These values are likely to improve with accelerated algorithms and low-timing-jitter detectors, which will further increase the potential of using single photons for clock synchronization.

6   Conclusions and outlook

The following two sections give the conclusions of the thesis (Section 6.1) and show two examples for further applications of the methods for clock synchronization (Section 6.2).

6.1 Conclusions

The conclusion section first provides a summary of the thesis content, relates it to the literature, and discusses its significance (Subsection 6.1.1). The following subsections show the limitations of the protocol for the synchronization of clocks with single photons (Subsection 6.1.2) and give a short outlook for potential relevant updates of the protocol (Subsection 6.1.3). The next section describes further applications and gives two examples, namely metrology and interferometer stabilization (Section 6.2).

6.1.1 Summary, comparison with literature and significance

This work addressed, developed, and characterized algorithms to utilize single photons for high-performance clock synchronization with standard crystal oscillators and achieved time-frequency stability comparable to previously published results with ultra-stable clocks. In the following, I will summarize the key steps of the algorithm, the findings, relate it to the literature (summarized in Table 6.1 and Fig. 6.1), and assess its significance.

The thesis provides a complete description of the **arrival time uncertainty** of single photons for clocks with constant and varying frequency offset. Differences in clock frequency cause a timing offset ΔT that increases timing uncertainty. The relationship between clock frequencies and timing jitter gives a better understanding of the limits of single-photon timing and its corresponding uncertainties. In particular, applications with long integration times benefit from the findings, as they suffer from increased timing jitters that are caused by poor-performing clocks.

Numerical optimizations and **sweeps of the frequency of crystal oscillators** improve the signal-to-noise ratio. The highest signal-to-noise ratio during the initialization of the synchronization is reached for a time bin size equal to the cross-correlation width. Furthermore, the bins are required to be equal to the width of the cross-correlation function and centered. For clocks with weak precision, such as unstable crystal oscillators, frequency sweeps significantly
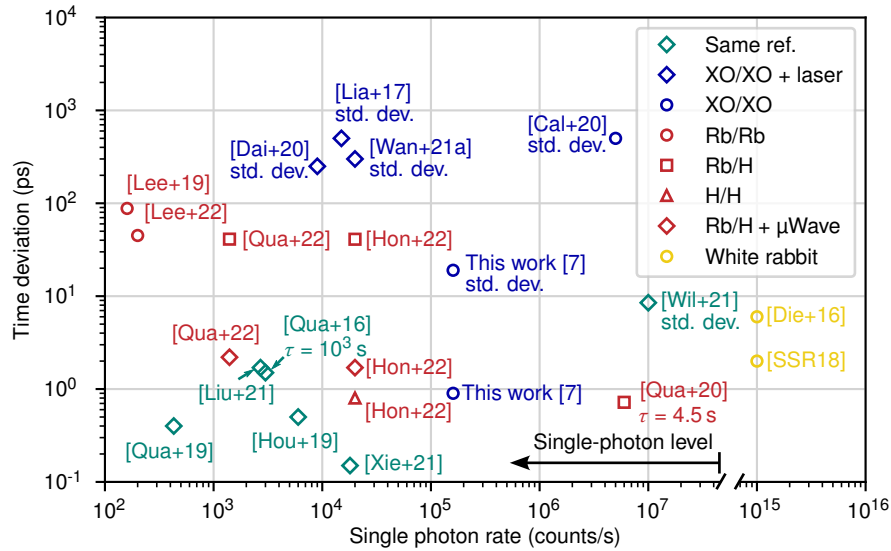
Figure 6.1 | Overview of clock synchronization performance with single photons. The time deviation strongly depends on the clock type being used. Setups that use identical clocks for both parties to be synchronized (green color) achieve the best performance. This changes when two different (high-precision, red-colored) clocks are used, such as rubidium vapor cell oscillators (Rb) or hydrogen masers (H). The time deviation is reduced by sharing the frequency through an additional 10-MHz clock synchronization channel (+μWave). Crystal oscillators (XO, blue color) are the most challenging to work with, but the requirements are relaxed when additionally transferring the clock signal via strong pulsed lasers (laser). The high-precision time transfer protocol White Rabbit (yellow color) uses classical strong laser light, but this thesis shows that significantly less signal on the single-photon level does not compromise the timing performance. In addition, the time deviation is comparable to that of using hydrogen masers or even the same reference. The plot displays the time deviation for an averaging time of $\tau = 100$ s, if not stated otherwise. The publications [Cal+20; Dai+20; Lia+17; Wan+21b] indicate the standard deviation (std. dev.) of the timing offset variation.

increase the signal-to-noise ratio. In contrast to a wide range of publications [Eck+21; Hon+22; Hou+19; Lee+19; Lee+22; Liu+21; Qua+16; Qua+19; Qua+20; Qua+22; Ste+17; Urs+07; VSS04; Wil+21], additional (or the same) stable references are no longer required. The frequency uncertainty can be reduced by almost two orders of magnitude with asynchronous single-photon sources, compared to previously reported values [HLK09]. I published this method in [2] as the conference proceeding and in [5]. Since then, the method has been applied to compensate for the Doppler shift in satellites for quantum communication [Wan+21a], or to initialize quantum key distribution sessions [Fit+22]. In particular, application scenarios with low signal and unstable references benefit from the optimizations, e.g., long-distance and multi-user quantum communication networks.

Live tracking algorithms update the clock frequency of the slave clock to the master clock during a communication session. Previous work focused on live algorithms with active synchronization strings [Cos+20] and implemented it in quantum key distribution systems [Ave+21; Mar+22]. Synchronization strings are not desired in entanglement-based systems, as additional modulators would be required. The implementation of synchronization based on

single photons is also described in the publication [Fit+22], but without presenting the algorithm or characterizing and optimizing the performance. Here, I developed a novel algorithm that does not require actively encoded synchronization strings [Ave+21; Cos+20; Mar+22], or stable references as in the publications [Eck+21; Hon+22; Hou+19; Lee+19; Lee+22; Liu+21; Qua+16; Qua+19; Qua+20; Qua+22; Ste+17; Urs+07; VSS04; Wil+21]. Furthermore, the performance of the synchronization method was developed and optimized. The frequency tracking method provides an RMS synchronization timing jitter of as low as 3 ps and a timing stability of 19 ps at an integration time of 1 s and 3.2 ps at 100 s. The synchronization performance is even better than free-running rubidium oscillators (41.1 ps [Qua+22], 16.7 ps [Lee+22] and 40.8 ps [Hon+22] at 100 s integration time) and much lower than the 30 to 50 ps jitters reported for systems that employ GPS-disciplined clocks [Eck+21; Ste+17] (estimated from residual timing offset variation). This comes mainly from two facts:

1. I employ fast feedback cycles of 5-10 Hz, while the GPS provided 1 feedback per second. Additionally, depending on the GPS module, it may show high time deviations between 1 and 10 ns (Fig. 2.9).

2. My developed algorithms not only adjust the timing offset, but also match the frequency of the clocks. This drastically reduces the variation of timing offset between feedback cycles.

Compared with classical methods for high-precision time transfer, like the White Rabbit protocol, the performance is similar (11 ps at 1 s and 2 ps at 30 s [SSR18]) or even lower (45 ps at 1 s, 15 ps at 10 s and 6 ps at 100 s [Die+16]) although significantly less signal is used (single-photon level). Highly stable references, like rubidium clocks or synchronization lasers, are mostly used to establish clock synchronization. This is no longer required with the developed methods. No further hardware is needed for participants in multi-user quantum networks, as the synchronization protocol works with low-performance quartz crystal oscillators. The protocol significantly compensates for the imperfections of the unstable crystal oscillator. This allows devices with crystal oscillators integrated by default. Imagine a scenario where standard laptops (that have crystal oscillators) are connected to the quantum network, similar to our today's communication network. The laptop would no longer require highly stable rubidium clocks for quantum communication. The single photons themselves provide sufficient synchronization, simultaneously, to the actual data transfer.

The synchronization algorithm for **clocked single-photon sources** is much faster than for asynchronous sources. This provides lower time deviations and smaller timing jitters caused by the synchronization. To my knowledge, to date, no other publication has accessed the difference between clocked and asynchronous sources in the synchronization algorithm [6; 7]. In clocked single-photon sources, the observation window is reduced from the integration time

(~ms) to the clock rate (~ns). Furthermore, only a single array of arrival times is processed, instead of two in, e.g., the Start-Stop method (one from receiver A and one from receiver B). Essentially, the *receiver is capable of processing the arrival time and locking its clock frequency independently of the other receivers*. In particular, this can also be applied to clocked entangled photon-pair sources, where every receiver locks its slave clock to the source master independently. In addition, this enables very fast processing of the arrival-time information of photons. As a consequence, fast processing of the arrival time enables a frequency search with higher resolution because the frequency sweeps of the oscillators depend strongly on the computation time. The resolution of the frequency after the sweeps is three orders of magnitude higher than with asynchronous sources. The large clock frequency uncertainty with asynchronous sources is critical in low-signal environments, as the signal-to-noise ratio is further reduced. This could prevent a successful initialization of the synchronization. Clocked single-photon sources solve this challenge and enable synchronization at extremely small signal-to-noise ratios, such as long-distance communication links. These research results were published in [6; 7].

In the experiments shown, the algorithms were applied to **realistic link scenarios**, including a 70 km intercity fiber link and a 1.7 km turbulent free-space intracity link. Longer fiber links have already been used to assess performance [Hon+22; Hou+19; Lee+22; Liu+21; Qua+16; Qua+19; Qua+22; Xie+21], relying on stable references instead of simple crystal oscillators as were used in this work. On a free-space link, the concept has been applied to a satellite link in the publication [Dai+20]. Recently, in December 2022, the first quantum-based two-way time transfer over a hybrid link (fiber and free space) appeared on arXiv [Xia+22]. The first theoretical estimations of the synchronization performance on a free space link have been published on arXiv in November 2022 [LL22]. However, all publications have in common that the same frequency reference is used. In contrast, separate, remote, and unstable crystal oscillators are used, which demonstrates a realistic scenario for a future scaled quantum network. Although unstable crystal oscillators are used, the synchronization performance reduces only slightly, as the protocol uses the timing of single photons as well. In an emulated turbulent satellite uplink, the FWHM synchronization timing jitter is as low as 231 ps with only 440 counts/s correlation events from an entangled photon-pair source. The same source gives rise to 297 ps FWHM timing jitters on the 1.7 km intracity link. This is just an increase in the reference timing jitter (perfect synchronization) by 7.6 %. On the 70 km intercity fiber link there is a FWHM synchronization timing jitter of 54.6 ps, which corresponds to an increase in the reference timing jitter of only 12.6 %.

When timing jitter increases, it limits the extent to which quantum key distribution can work effectively. Keeping timing jitter low means that we can use filters that reduce noise and errors. This thesis suggests a compromise: we accept a small increase in timing jitter in exchange for a much simpler quantum key distribution system. The algorithms for single-photon clock synchronization stay strong, even when signals fluctuate a lot, as in complicated free-space

scenarios.

In summary, the findings of the thesis reduce the required hardware in future quantum communication systems, set the foundation for much enhanced time transfer, and enable metrology with single photons. The algorithms developed for single-photon sources:

1. work with any single-photon source source (clocked or asynchronous),

2. work with any clock (even crystal oscillators),

3. are not limited by the application scenario (feasibility at low signal-to-noise ratios, turbulent free-space links, long-distance fiber links). I show a timing stability that reaches the femtosecond level after just 1000 s of time averaging on a 70 km deployed fiber link.

4. establish 3 ps synchronization timing jitter and 19 ps stability (TDEV) at 1-s integration time (this is better than free-running rubidium clocks and comparable to the White Rabbit time transfer protocol),

5. provide applications for single-photon metrology (e.g. location, velocity, or acceleration of moving objects), and

6. could be the foundation for high performance synchronization on interferometric level.

Table 6.1 | Non-exhaustive list of relevant publications.

Reference	Setup	Oscillator	Performance
[VSS04]	EPS	same ref	$\approx 1 - 10$ ps
[HLK09]	EPS	XO/XO	no performance
[Qua+16]	EPS, HOM	same ref	TDEV $1.5 - 1.9$ ps @ 1000 s
[Die+16]	White Rabbit	XO/XO	6 ps @ 100 s
[Lia+17]	WCS, not live	XO/US-XO	$\sigma_{RMS,sync} = 500$ ps (sync. laser)
[SSR18]	White Rabbit	XO/XO	2 ps @ 30 s
[Qua+19]	EPS, HOM	Same ref	TDEV $0.4 - 1.0$ ps @ 100 s
[Lee+19]	EPS	Rb/Rb	TDEV 45 ps @ 100 s
[Hou+19]	EPS, HOM	same ref	TDEV $3.6 - 4.1$ ps in 100 s
[Qua+20]	EPS	Rb/H	0.72 ps @ 4.5 s
[Dai+20]	WCS, not live	XO/US-XO	Residuals $250 - 450$ ps (RMS) @ 1 s
[Cal+20]	WCS	XO/XO	$\Delta T = \pm 1.5$ ns (3σ), RMS ≈ 500 ps @ 1 s
[Cos+20]	WCS, live QKD	XO/XO	no performance
[Xie+21]	EPS, HOM	same ref	TDEV 0.25 ps @ 100 s
[Wan+21a]	WCS	XO/XO	residuals $302 - 420$ ps (RMS)
This work [5]	EPS, live QKD	XO/XO	$\sigma_{RMS,sync} = 68 - 98$ ps, no TDEV avail.
[Liu+21]	EPS, HOM	same ref	TDEV $1.7 - 6.0$ ps @ 100 s
[Wil+21]	EPS	same ref	8.5 ps (RMS)
[Qua+22]	EPS	Rb/H	TDEV 41.1 ps @ 100 s
[Qua+22]	EPS	Rb/H+µWave	TDEV 2.16 ps @ 100 s
[Lee+22]	EPS	Rb/Rb	TDEV 88 ps @ 100 ps
[Hon+22]	EPS	Rb/H+µWave	TDEV 1.7 ps @ 100 s
[Hon+22]	EPS	H/H	TDEV 0.8 ps @ 100 s
[Hon+22]	EPS	Rb/H	TDEV 41 ps @ 100 s
[Fit+22]	EPS, live QKD	XO/XO	no performance
This work [7]	WCS, live QKD	XO/XO	$\sigma_{RMS,sync} = 3$ ps, TDEV 3.2 ps @ 100 s

The experimental setup consists of an entangled photon pair source (EPS) or a weak coherent source (WCS) that uses attenuated laser light. The synchronization setup may be based on the Hong-Ou-Mandel interference (HOM) or is suited (or already integrated) for quantum key distribution (QKD). The QKD mode of operation may be in real time or via post-processing of all the data after long-term collection. The oscillators at Alice/Bob to be synchronized may be crystal oscillators (XO), ultra-stable crystal oscillators (US-XO), rubidium clocks (Rb), or H-maser (H). In some literature, a microwave frequency transfer takes place (+µWave) or the same reference is used. Same reference means that the same time-to-digital converter is used, or one clock synchronizes two time-to-digital converters, so that the frequency difference between the clocks is close to zero. There are various types of definitions for the synchronization performance, like the Allan time deviation (TDEV), the synchronization timing jitter $\sigma_{RMS,sync}$ (RMS = root mean squared, FWHM = full width at half maximum), residual timing offset variations after a linear fit (residuals) or the variation of the timing offset ΔT in a given interval (see Chapter 2).

6.1.2 Limitations

The current bottlenecks of synchronization with single photons are the following:

1. The speed of light. The time it takes to transfer the measurement information has an upper limit and concerns asynchronous single-photon sources. When the measurement takes place at a remote receiver at a distance of 100 km, it takes 0.33 ms to bring the data back to correlate the events. As a consequence, the maximum update frequency is 3 kHz. However, this does not apply to clocked single-photon sources, where measurement and processing are done at the same place.

2. Computation time. Time stamp processing is time consuming and limits the feedback time. This time is reduced by following hardware-based approaches with Field-Programmable-Gate Arrays (FPGAs).

3. Single-photon detectors and time taggers. Smaller timing jitters result in higher performance time transfer. The precision is likely to increase in the future.

4. Electronics in general. There is always a delay for the processing and transfer in single-photon detectors, time taggers, etc. Ideally, an all-optical synchronization method without electrical interfaces should be applied to lock clocks with the fastest feedback cycles. The first steps towards this goal have been demonstrated impressively with remote optomechanical systems [Li+22] and X-ray free electron lasers [Sch+15].

6.1.3 Further directions

There are some interesting aspects that have not been covered in this thesis, but could be a promising avenue to improve and advance the synchronization protocols used. In particular, the following two deserve attention:

1. symmetrical clock synchronization (two-way optical time transfer) as one step towards secure time transfer,

2. synchronization with the second-order correlation function (Hong-Ou-Mandel) to increase the timing precision.

The introduction of a **two-way optical time transfer** has potential for quantum-secure time transfer [Dai+20; NH18] and the precision can be enhanced using the **Hong-Ou-Mandel effect** of the two-photon states. There are several publications that show successful experimental setups [Liu+21; Qua+16; Qua+19; Xie+21]. However, the increase in precision by a factor of $\sqrt{2}$ for a photon state of $N = 2$ [GLM01] comes at the cost of a much reduced rate of the signal. This is caused by the low probability of two photons arriving at the beam splitter at the same time due to system losses. This could be a bottleneck considering an implementation with

unstable clocks. They require fast update loop times of the clock frequency, but low signal rates increase the uncertainty and limit the synchronization performance. However, when solving the main challenge of losses, two-photon states could be a promising direction towards quantum-enhanced timing and precision [GLM01].

6.2 Further applications

Apart from quantum communication, there are already other interesting applications where the developed methods could be applied, namely metrology of moving objects or the stabilization of interferometers. For the first step, I applied the synchronization methods to a moving satellite to calculate its relative speed with respect to a ground station (Section 6.2.1). The findings can also be applied to, e.g., measure the speed of moving aircrafts with single photons. After this metrology section, I will describe how single photons can be used to effectively stabilize the interferometer (Section 6.2.2). This could give an outlook to a timing precision of femtoseconds with single photons.

6.2.1 Feasibility study: metrology of moving objects

RADAR, or radio detection and ranging, has long been used to detect the position and estimate the velocity of objects using radio frequency signals [MJW10]. Similarly, LIDAR, or laser-based detection and ranging, has become increasingly popular due to its higher precision and accuracy, finding applications in remote sensing, automated process control, collision avoidance systems [STS01; Wil+04], and autonomous driving [Yoo+18]. Recent advances in LIDAR have demonstrated the ability to use single photons for long-range (kilometers) and eye-safe operation [Rap+20; Tac+19]. This technology has also been successfully applied in scenarios such as the robust reconstruction of snapshots of moving objects based on single photons [Tob+21]. In this section, I will give an insight of how to advance current methods that use LIDAR for moving objects by using single photons. By emulating a satellite downlink scenario [AAH98] and applying relevant processing algorithms of this thesis, I investigated the impact on the timing of single photons. The goal is to show that even without knowing the precise orbit of the satellite, it is possible to measure its relative distance and velocity accurately using only single photons.

For the feasibility study, I took an orbit in 1000 km height and the assumption that there is a sufficient (and constant!) signal on the receiver side. The count rates are $r_A = 500 \times 10^3$ counts/s, $r_B = 80 \times 10^3$ counts/s, and the correlation rate is $r_C = 4.2 \times 10^3$ pairs/s. The count rates come from a recent quantum key distribution experiment on our 1.7 km intracity free-space link. They are not representative for a satellite link and are orders of magnitude higher but comply with the assumption that there is enough signal at the receiver. The goal is to understand the impact of the relative acceleration and velocity of the satellite on the timing distribution. I
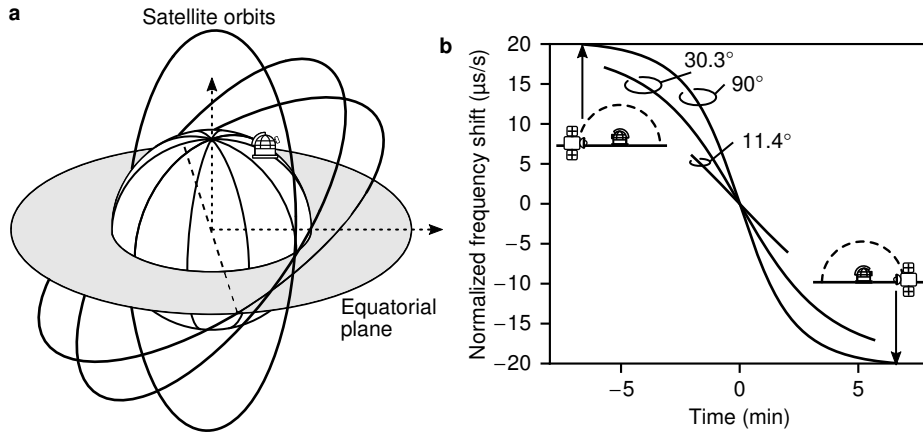
Figure 6.2 | The satellite orbit and its corresponding frequency shift. a, Satellite orbits for varying elevations. **b**, Calculated frequency shift for an inclination of 50° (the latitude coordinate of the city Jena is 50°) and varying elevations. The satellite is assumed to be in an orbit of 1000 km above the surface of earth.

took the recorded time stamps to emulate the effect of the Doppler shift in time by a satellite overflow without knowing the orbit. An analytical representation of the Doppler effect is used to seed the scenario.

Compared to the ground station, there is a frequency shift of up to 20 ppm (Fig. 6.2). This is not much different from the precision of crystal oscillators. However, this frequency changes to -20 ppm in just 12 minutes, which greatly affects the timing distribution (Fig. 6.3**a,b**). The change in frequency is small when the satellite appears on the horizon. Here, my developed frequency tracking algorithm would keep up. However, when the satellite approaches the zenith, it has a very high relative acceleration, which requires fast update times. However, as the update time is constant (here: 1 s), the timing distribution increases its width.

Taking a quantum communication scenario, a wide timing distribution reduces the coincidence-to-accidentals ratio (CAR), as the number of accidental correlation events increases with a larger timing jitter δ_{FWHM}. The CAR is the ratio between true coincidences c_{true} (without accidental correlation events), divided by accidental correlation events c_{acc} [C X+11; He+15; Zha+20],

$$\text{CAR} = \frac{c_{true}}{c_{acc}} = \frac{r_C - r_A r_B \delta_{FWHM}}{r_A r_B \delta_{FWHM}}. \tag{6.1}$$

The introduced timing offset ΔT depends on the relative Doppler frequency shift $\Delta f / f$, the feedback loop time to adjust the frequency at the receiver T_{feed} and the integration time T_{int},

$$\Delta T = \left| \frac{\partial(\Delta f / f)}{\partial t} \right| T_{int} T_{feed}. \tag{6.2}$$

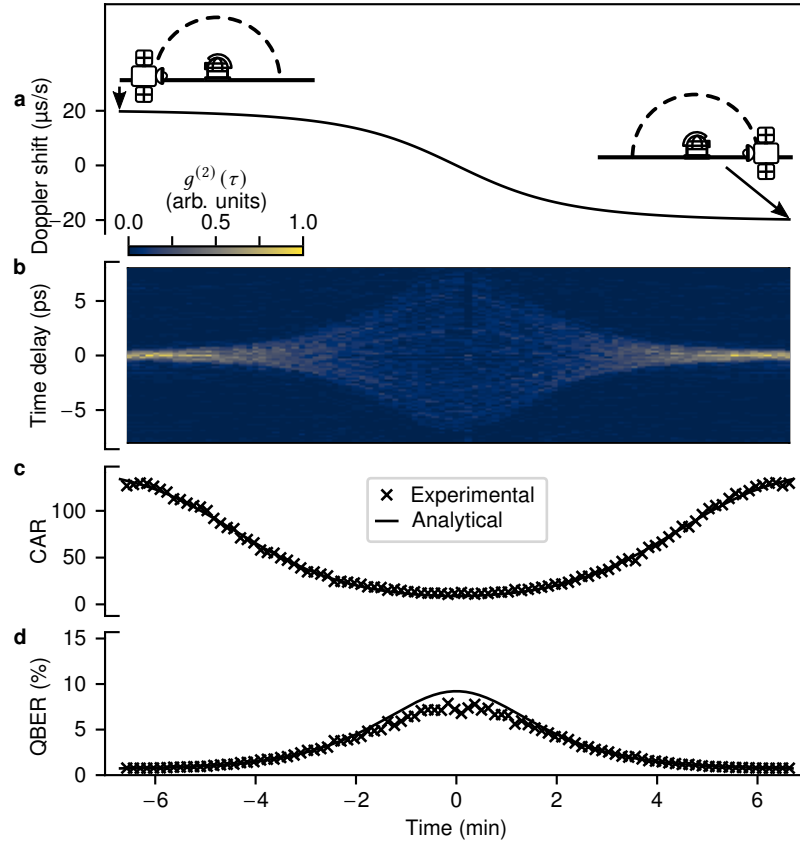This gives the timing jitter δ_{FWHM} from the initial jitter $\delta_{FWHM,init} = 714\,\text{ps}$,

Figure 6.3 | Emulating the timing distribution without knowing the satellite orbit and with single-photon frequency transfer. a, When the satellite appears and disappears at the horizon, the change in the Doppler frequency shift is the smallest. **b**, As the frequency update time is only 1 s, the tracking algorithm cannot keep up with the rapid frequency changes. As a consequence, the timing distribution enlarges when the satellite reaches the zenith. **c**, Assuming a constant signal from the satellite, the coincidence-to-accidental ratio (CAR) is highest for small relative satellite accelerations with respect to the ground station. **d**, The quantum bit error rate (QBER) is the highest at the zenith. Analytical trend lines are based on Equations 6.1, 6.5 and 6.3 with $r_A = 500 \times 10^3$ counts/s, $r_B = 80 \times 10^3$ counts/s and the correlation rate $r_C = \text{const.} = 4.2 \times 10^3$ pairs/s.

$$\delta_{\text{FWHM}}^2 = \delta_{\text{FWHM,init}}^2 + \Delta T^2/2. \tag{6.3}$$

As described in Section 4.3.1, the Equation 6.3 is a good estimate of the timing distribution for $\Delta T > \delta \text{FWHM,init}$. The CAR decreases as the timing jitter increases (Fig. 6.3**c**). This ratio gives a visibility V that is defined with the highest c_{max} and minimum c_{min} detected correlation events [Han+07; T H+08; TS10],

$$V = \frac{c_{\text{max}} - c_{\text{min}}}{c_{\text{max}} + c_{\text{min}}} = \frac{c_{\text{true}}}{c_{\text{true}} + 2c_{\text{acc}}} = \frac{\text{CAR}}{\text{CAR} + 2}. \tag{6.4}$$

The quantum bite error rate (QBER) for quantum communication is then derived as [T H+08; Tho+09],

$$\text{QBER} = \frac{1}{2}(1 - V). \tag{6.5}$$

The error rate is the highest at large accelerations of the satellite (Fig. 6.3**d**). Note that I assumed that the orbit of the satellite is unknown, which is not the case in practice. Due to that, it is possible to just estimate the deviations between the measured and estimated satellite orbits and correct for them [Wan+21b]. As a consequence, the error rate can be drastically reduced.

When the methods are applied to tracking the velocity of the satellite, the update time can be small when the satellite is at the horizon. Here, the relative velocity does not change much. On the other hand, there is large acceleration when the satellite is in the zenith; here, fast update times are required to still track the satellite's velocity. As optimization parameter takes the ground station the timing distribution, or the timing offset. In this way, the ground station can measure the instantaneous distance and velocity of the moving satellite and derive the acceleration from it. The same is possible with moving aircrafts. Here, it is more feasible as the signal rates are much higher to enable fast feedback loops for tight tracking of the motion parameters.

6.2.2 Stabilization of interferometers with single photons

The phase stabilization of interferometers plays a crucial role in both classical and quantum communication protocols [Che+20]. However, achieving a stable phase in fiber-based interferometers presents significant challenges due to factors such as thermal and mechanical influences [TJM82]. Although single photons have been successful in stabilizing interferometers with minor phase variations of $2 - 20\,°/\text{s}$ [VAD04; Wan+20], this level of stability falls short for fiber-based interferometers that experience phase fluctuations in the range of hundreds of °/s. Consequently, conventional methods [CK16], such as the use of the pump that generates single photons [Tol+15], are still used for stabilization. However, the scenario changes with the introduction of fast feedback algorithms developed in this thesis.
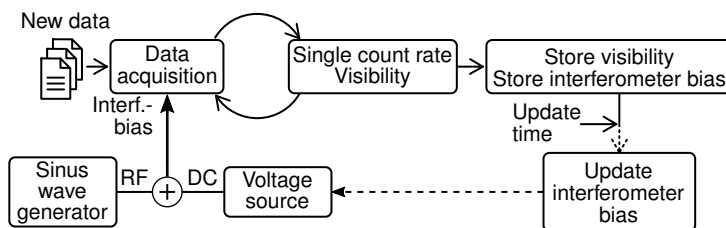

Figure 6.4 | Feedback algorithm for interferometer stabilization. Photons are detected continuously while modulating the phase with a sinus generator and its DC offset. The offset is adjusted after an update time to reach highest interference visibilities. The figure is from my publication [4].

The compensation concept operates as follows, as depicted in Figure 6.4: A sinusoidal generator produces a low-amplitude, $20\,\text{Hz}$ periodic phase modulation, acting as a dither [Li+18]. Within each cycle of the sinusoidal generator, the algorithm acquires five data points,

each with an integration time of 10 ms. The subsequent step is straightforward: the algorithm selects the voltage applied to the interferometer's phase modulator (piezo) that yields the highest interference visibility among the five data points. This selected voltage becomes the new bias DC voltage, which is then combined with periodic and constant phase modulation.

The experimental setup consists of a single-photon source that utilizes attenuated laser pulses (see Fig. 6.5**a**). These single photons follow a designated path leading to an interferometer equipped with a piezoelectric element to stabilize and lock the phase difference between its two arms. The interferometer outputs exhibit a phase difference of π, resulting in destructive or constructive interference when phaselocked. Any alterations in the phase within the interferometer cause changes in the count rate observed by the single-photon detectors.

Although the accuracy of phase lock achieved ($\sigma_\lambda = 0.012\,\lambda$) is lower compared to classical systems ($\sigma_\lambda = 0.0029\,\lambda$) as reported by [Wu+19], single photons can still be a valuable asset in achieving a minimum level of stabilization in strongly drifting fiber-based interferometers, especially in resource-efficient quantum communication networks. It is worth noting that stabilizing an interferometer with a kilometer-long imbalance becomes less feasible due to the substantial phase variations. However, I believe that the concept holds promise for fiber-based interferometers with imbalances on the scale of tens of meters. This opens up various applications for single photons, including standard or interferometer-assisted clock synchronization, as well as the stabilization of interferometers in future quantum communication networks. By utilizing single photons, these applications can benefit from improved stability and enable advancements in quantum communication technologies.
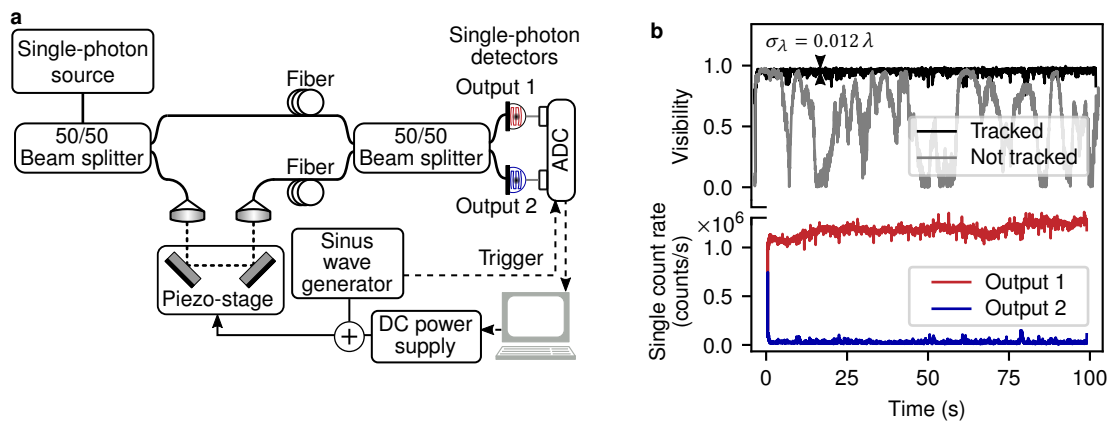

Figure 6.5 | Experimental setup to stabilize fiber-based interferometer with single photons. a, The interferometer consists of a piezo element that I use for stabilization. Depending on the phase shift in the interferometer, the detected single-photon count rate changes. This feedback is used to modify a DC voltage that is summed with a constant sinus voltage modulation. **b**, The visibility before and after activation of the interferometer phase tracking algorithm. The precision in the optical path length difference is 72 ± 18 nm ($\sigma_\lambda = 0.012\,\lambda$), estimated from the residual visibility (0.96) and its fluctuations (0.03), since the phase is $\delta \approx 2\arccos(V)$ rad. The fiber length fluctuations indicate a magnitude of 440 °/s (1 x standard deviation) that I derive from the untracked visibility. The figure is modified from my publication [4].

A Appendix

A.1 Laser rate equations

When the working point of the laser diode is not correct, this could complicate the frequency lock at the receiver and lower the synchronization performance. The working point is defined by the current amplitude and repetition rate sent from the function generator to the laser diode. To find the optimum point, I model and optimize the dynamic evolution of the output intensity based on the input current. The goal is to achieve sharp edges of the pulses that are beneficial for the frequency lock at the receiver. For this, I take a representative experimental measurement and match it with the theoretical model. This gives me a set of parameters of the laser diode, e.g., the volume of the active region, that is not provided by the manufacturer. With the model and the parameter set of the laser diode, I can simulate different working points of the laser diode and optimize it.
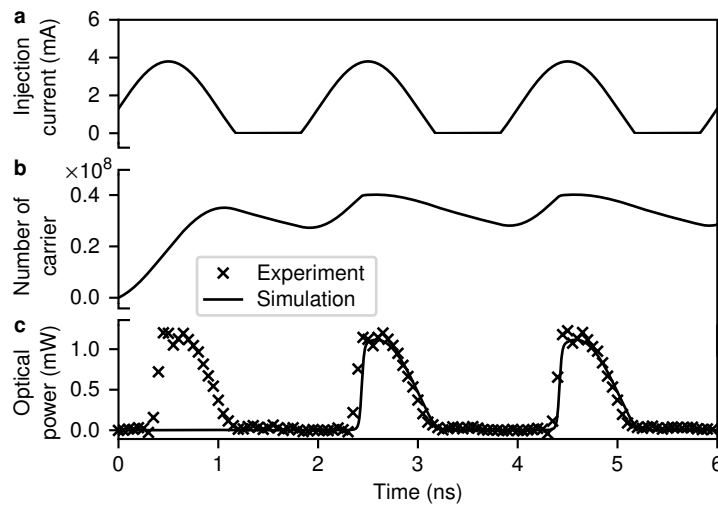
Figure A.1 | Simulated and experimental laser diode dynamics. a, The injection current is a sine wave with a peak-to-peak current of 5 mA and a mean value of 1.3 mA. **b**, When injecting the first current peak, the number of carriers does not reach the optical lasing threshold. Only after the second injection peak does lasing begin. **c**, The simulated trend of the optical output power matches the experimental values well. The other parameters of the laser diode are described in Table A.1.

The dynamic characteristics of a semiconductor laser can be described by the following single-mode rate equations of the carrier density N and photon density S for an injected current J from the function generator [Li+19],

$$\frac{\mathrm{d}N}{\mathrm{d}t} = \frac{J}{eV} - \frac{g_0(N - N_t)S}{1 + \epsilon S} - \frac{N}{\tau_N},$$

(A.1)

Table A.1 | Parameters to describe the dynamical output of laser diodes.

Variable	Description	Value	Unit
g_0	Gain slope constant	2×10^{-12}	m^3/s^{-1}
N_t	Carrier density at transparency	1.2×10^{24}	m^{-3}
τ_N	Total spon. emission carrier lifetime	3×10^{-9}	s
τ_P	Average ph. lifetime inside the cavity	10^{-12}	s
Γ	Mode confinement factor	0.44	-
ϵ	Gain compression factor	2×10^{-25}	m^{-3}
β	Fraction of spontaneous emission	4×10^{-4}	-
e	electronic charge	1.6×10^{-19}	C
V	Active region volume	1.4×10^{-20}	m^3
μ_0	Differential quantum efficiency	1	-
h	Planck's constant	6.6×10^{-34}	Js
ν	Frequency	193.9×10^{12}	Hz

Only the gain slope constant g_0, the gain compression factor ϵ and the active region volume V have been adapted to the experimental laser diode from $3 \times 10^{-12}\,\mathrm{m^3/s^{-1}}$, $3.4 \times 10^{-23}\,\mathrm{m^{-3}}$, $9 \times 10^{-17}\,\mathrm{m^3}$, respectively, as given by [Li+19].

$$\frac{dS}{dt} = \frac{\Gamma g_0 (N - N_t)S}{1 + \epsilon S} - \frac{S}{\tau_P} + \Gamma \beta \frac{N}{\tau_N}, \tag{A.2}$$

with the all parameters and values described in Table A.1. The optical output power P_{out} is

$$P_{\text{out}} = \frac{\mu_0 V h\nu}{2\Gamma \tau_P} S. \tag{A.3}$$

With the rate equations and the parameters of the laser diode, it is possible to simulate the dynamical behavior for much simpler waveforms that also match the experiment (Fig. A.1). Biased sine waveforms are easy to generate, as it is just a combination of a sine wave plus offset (bias). When applied to the laser diode, they can still create sharp optical pulses, thanks to the nonlinear transfer function of the laser diode. The biased sine waveform does not require many electrical resources, as it can be generated in an analog function generator. Consequently, the electrical driving circuit can be compact, lightweight, and resource-efficient, which is compelling for use on satellites or up-scaled communication networks.

A.2 Live tracking of the clock frequency under low signal-to-noise ratio with an entangled photon pair source
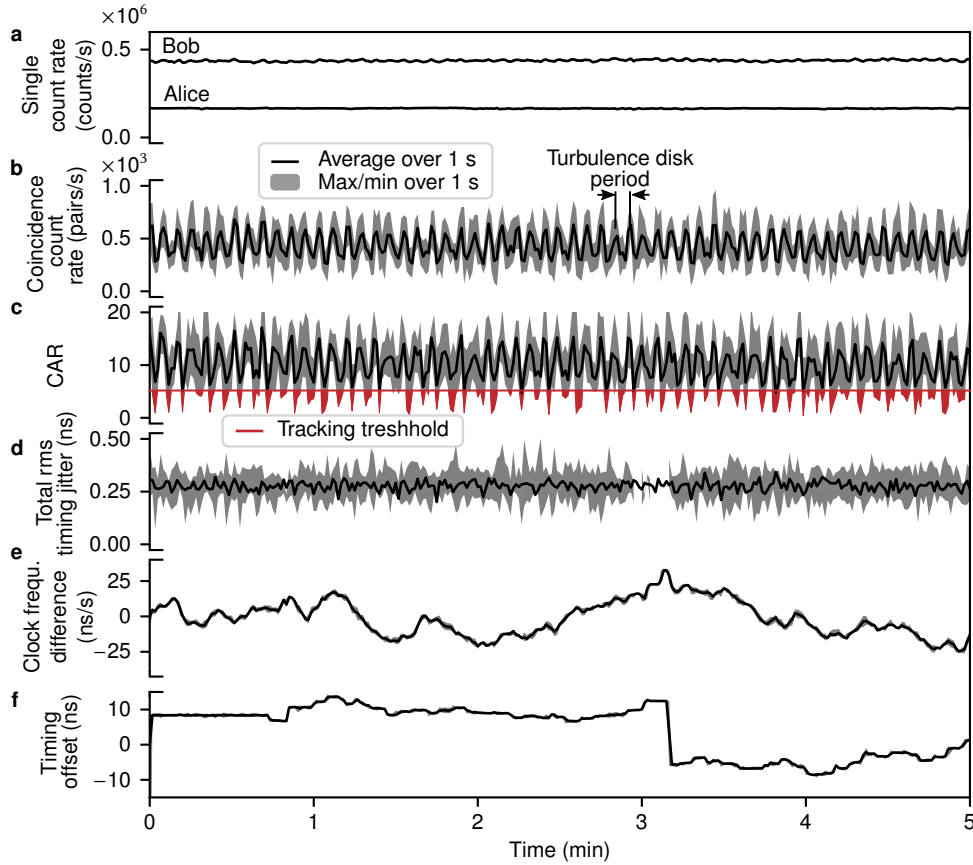
Figure A.2 | Low correlation rate live tracking under atmospheric turbulence. Turbulence parameter: Fried parameter 1 mm, $1/e^2$ full-width beam waist of 3.4 mm. **a**, The count rate at the receiver Bob of 437 ± 6 kcps is artificially increased by a noise source. Alice's count rate amounts to 165 ± 3 kcps. **b**,The average coincidence rate is 430 ± 160 cps (coincidence window is equal to RMS timing jitter of 267 ps) and indicates periodic fluctuations from the rotating turbulence disk. **c**, The mean coincidence-to-accidentals ratio is 10 ± 4 with a live tracking threshold of 5 for the correlation peak. **d**, The total timing jitter probability distribution describes a Gaussian with its fitted center at 277.8 ± 0.8 ps. Together with same-clock total timing jitter of 260 ± 2ps is the synchronization jitter approximately 98 ± 6 ps. **e**, The tracked difference of the clock frequency over time. **f**, The timing offset varies more than in an environment with higher signal-to-noise ratio (Fig. 5.12), because of partially stopped tracking when the coincidence-to-accidentals ratio falls below 5. This gives rise to an increase of the total timing jitter. The feedback loop time and data package size amounts to 200 ms and 100 ms, respectively. The figure is modified from my publication [5].

A.3 Time deviation for different experimental scenarios

Table A.2 | Time deviation (TDEV) in the unit of ps for different experimental scenarios from literature.

Reference	Scenario	System jitter	Count rate	Averaging time (s)									
				0.15	0.2	0.4	1	2	4	10	20	40	100
1. Rb/Rb	WCS, 10 m lab	92 ps	160×10^3 counts/s	21.5	16.2	8.3	4.3	5.5	11.4	28.7	45.8	65.9	106.2
2. XO/XO (ns)	WCS, 10 m lab	92 ps	160×10^3 counts/s	0.20	0.22	0.24	0.35	0.78	2.03	7.37	13.9	19.6	44.0
3. XO/XO-†	WCS, 10 m lab	92 ps	160×10^3 counts/s	54	46	32	19	13	9.5	6.0	3.5	1.9	3.2
4. XO/XO-μ (Ref)	WCS, 10 m lab	92 ps	160×10^3 counts/s	24.1	18.6	10.0	4.5	2.8	1.8	1.1	0.93	0.75	0.25
5. XO/XO-†-J/E	WCS, 70 km depl.	98 ps	100×10^3 counts/s	-	-	175	115	76	46	26	19	12	5.9
[Qua+22] Rb/H	EPS, 7 km depl.	≈ 200 ps	1.4×10^3 pairs/s	-	-	-	-	-	-	-	-	29.9	41.1
[Qua+22] Rb/H-μ	EPS, 7 km depl.	≈ 200 ps	1.4×10^3 pairs/s	-	-	-	-	-	-	-	-	1.87	2.16
[Lee+22] Rb/Rb	EPS, 10 km lab	900 ps	160 pairs/s	-	-	-	-	-	25.9	19.4	18.1	17.1	16.7
[Hon+22] H/H	EPS, 50 km lab	120 ps	220 pairs/s	-	-	-	-	-	-	2.3	1.65	1.21	0.83
[Hon+22] Rb/H	EPS, 50 km lab	120 ps	220 pairs/s	-	-	-	-	-	-	14.4	21.2	26.2	40.8
[Hon+22] Rb/H-μ	EPS, 50 km lab	120 ps	220 pairs/s	-	-	-	-	-	-	2.33	1.70	1.23	0.82
[Wil+21] same CK	EPS+, 50 km lab	-	$>5\times10^6$ pairs/s	8	-	-	-	-	-	-	-	-	-

The sender/receiver may consist of a rubidium oscillator (Rb) or a hydrogen maser (H). Sometimes a 10 MHz microwave frequency transfer is added (-μ). In reference [Wil+21], the same clock (CK) has been used. The first five rows (1.-5.) represent the scenarios covered in this thesis. Single-photon time-frequency transfer (†) increases stability significantly and provides stability comparable to highly stable references. Row number 5 represents the experiment on the 70 km fiber link between Jena and Erfurt (J/E). The values from literature may come from linear interpolations, as the data are recorded at averaging times not equal to the times in this thesis. Other parameters are the following. The source type: faint pulse source (WCS, weak coherent source), entangled photon pair source (EPS), or an EPS with synchronization based on single photons from an external laser (EPS+). Link setup: in the lab or on a deployed link (depl.) and the corresponding distance. The system jitter that excludes the timing jitter caused by poor synchronization. The count rate of correlation events in a faint pulse source (unit: counts/s) and in a photon pair source (unit: pairs/s).

Bibliography

[AAH98]   I. Ali, N. Al-Dhahir, and J. E. Hershey. **Doppler characterization for LEO satellites**. *IEEE Transactions on Communications* 46:3 (1998), 309–313. ISSN: 00906778. DOI: 10.1109/26.662636 (see page 96).

[All+04]   R. Alléaume, F. Treussart, J-M Courty, and J-F Roch. **Photon statistics characterization of a single-photon source**. *New Journal of Physics* 6 (2004), 85. DOI: 10.1088/1367-2630/6/1/085 (see page 44).

[AP05]   Larry Andrews and Ronald Phillips. "Laser Beam Propagation Through Random Media." In: 2005. ISBN: 0819459488. DOI: 10.1117/3.626196 (see page 75).

[Ang14]   James J. Angel. **When Finance Meets Physics: The Impact of the Speed of Light on Financial Markets and Their Regulation**. *Financial Review* 49:2 (2014), 271–281. DOI: 10.1111/fire.12035 (see page 5).

[Ave+21]   Marco Avesani, Luca Calderaro, Giulio Foletto, Costantino Agnesi, Francesco Picciariello, Francesco B. L. Santagiustina, Alessia Scriminich, Andrea Stanco, Francesco Vedovato, Mujtaba Zahidy, Giuseppe Vallone, and Paolo Villoresi. **Resource-effective quantum key distribution: a field trial in Padua city center**. *Optics letters* 46:12 (2021), 2848–2851. DOI: 10.1364/OL.422890 (see pages 6–8, 90, 91).

[Bec05]   Wolfgang Becker. **Advanced time-correlated single photon counting techniques**. Vol. 81. Springer Science & Business Media, 2005 (see page 36).

[Bel95]   J. C. Bellamy. **Digital network synchronization**. *IEEE Communications Magazine* 33:4 (1995), 70–83. ISSN: 01636804. DOI: 10.1109/35.372197 (see page 5).

[BB14]   Charles H. Bennett and Gilles Brassard. **Quantum cryptography: Public key distribution and coin tossing**. *Theoretical Computer Science* 560 (2014), 7–11. ISSN: 03043975. DOI: 10.1016/j.tcs.2014.05.025 (see pages 5, 7, 11, 12, 27, 62).

[BBM92a]   Charles H. Bennett, Gilles Brassard, and N. David Mermin. **Quantum cryptography without Bell's theorem**. *Physical Review Letters* 68:5 (1992), 557–559. ISSN: 0031-9007. DOI: 10.1103/PhysRevLett.68.557. URL: https://link.aps.org/doi/10.1103/PhysRevLett.68.557 (see page 7).

[BBM92b]   Charles H. Bennett, Gilles Brassard, and N. David Mermin. **Quantum cryptography without Bell's theorem**. *Phys. Rev. Lett.* 68 (5 Feb. 1992), 557–559. DOI: 10.1103/PhysRevLett.68.557. URL: https://link.aps.org/doi/10.1103/PhysRevLett.68.557 (see pages 12, 61).

[Ber+16]   P. Berceau, M. Taylor, J. Kahn, and L. Hollberg. **Space-time reference with an optical link**. *Classical and Quantum Gravity* 33:13 (2016), 135007. ISSN: 0957-0233. DOI: [10.1088/0264-9381/33/13/135007](https://doi.org) (see page 5).

[Bes07]   Roland E. Best. **Phase-Locked Loops: Design, Simulation, and Applications**. 6th ed. New York: McGraw-Hill Education, 2007. ISBN: 9780071493758. URL: https://www.accessengineeringlibrary.com/content/book/9780071493758 (see page 27).

[BM10]   B. Vijay Bhaskar and Vikram M. Mehta. **Atmospheric Particulate Pollutants and their Relationship with Meteorology in Ahmedabad**. *Aerosol and Air Quality Research* 10:4 (2010), 301–315. ISSN: 16808584. DOI: [10.4209/aaqr.2009.10.0069](https://doi.org) (see page 81).

[Boa+18]   Alberto Boaron, Boris Korzh, Raphael Houlmann, Gianluca Boso, Davide Rusca, Stuart Gray, Ming-Jun Li, Daniel Nolan, Anthony Martin, and Hugo Zbinden. **Simple 2.5 GHz time-bin quantum key distribution**. *Applied Physics Letters* 112:17 (2018), 171108. ISSN: 0950-0340. DOI: [10.1063/1.5027030](https://doi.org) (see page 27).

[Bra+22]   Emma Brambila, Rodrigo Gómez, Riza Fazili, Markus Gräfe, and Fabian Steinlechner. **Ultrabright Polarization-Entangled Photon Pair Source for Frequency-Multiplexed Quantum Communication in Free-Space** (2022). DOI: [10.48550/ARXIV.2205.10214](https://doi.org). URL: https://arxiv.org/abs/2205.10214 (see pages 62, 63).

[Bre97]   S. Bregni. **Clock stability characterization and measurement in telecommunications**. *IEEE Transactions on Instrumentation and Measurement* 46:6 (1997), 1284–1294. DOI: [10.1109/19.668274](https://doi.org) (see page 8).

[Bru+99]   Christian Brunel, Brahim Lounis, Philippe Tamarat, and Michel Orrit. **Triggered Source of Single Photons based on Controlled Single Molecule Fluorescence**. *Physical Review Letters* 83:14 (1999), 2722–2725. ISSN: 0031-9007. DOI: [10.1103/PhysRevLett.83.2722](https://doi.org). URL: https://link.aps.org/doi/10.1103/PhysRevLett.83.2722 (see page 44).

[C X+11]   C. Xiong, Christelle Monat, Alex S. Clark, Christian Grillet, Graham D. Marshall, M. J. Steel, Juntao Li, Liam O'Faolain, Thomas F. Krauss, John G. Rarity, and Benjamin J. Eggleton. **Slow-light enhanced correlated photon pair generation in a silicon photonic crystal waveguide**. *Optics Letters* 36:17 (2011), 3413–3415. ISSN: 0146-9592. DOI: [10.1364/OL.36.003413](https://doi.org) (see page 97).

[Cal+20]   Luca Calderaro, Andrea Stanco, Costantino Agnesi, Marco Avesani, Daniele Dequal, Paolo Villoresi, and Giuseppe Vallone. **Fast and Simple Qubit-Based Synchronization for Quantum Key Distribution**. *Physical Review Applied* 13:5 (2020), 054041. DOI: [10.1103/PhysRevApplied.13.054041](https://doi.org) (see pages 6, 7, 25, 90, 94).

[CD15]   James C. Camparo and Travis U. Driskell. **The Mercury-Ion Clock and the Pulsed-Laser Rubidium Clock: Near-Term Candidates for Future GPS Deployment**. Tech. rep. Accessed on December 16, 2022. Photonics Technology Department, Physical Sciences Laboratories,The Aerospace Corporation, PO Box 92957, Los Angeles, CA 90009, USA, Oct. 2015. URL: https://www.researchgate.net/publication/329946899_The_Mercury-

Ion_Clock_and_the_Pulsed-Laser_Rubidium_Clock_Near-Term_Candidates_for_Future_GPS_Deployment (see page 22).

[Cao+22] Yuan Cao, Yongli Zhao, Qin Wang, Jie Zhang, Soon Xin Ng, and Lajos Hanzo. **The Evolution of Quantum Key Distribution Networks: On the Road to the Qinternet**. *IEEE Communications Surveys & Tutorials* 24:2 (2022), 839–894. DOI: 10.1109/COMST.2022.3144219 (see page 11).

[Che+21] Yu-Ao Chen, Qiang Zhang, Teng-Yun Chen, Wen-Qi Cai, Sheng-Kai Liao, Jun Zhang, Kai Chen, Juan Yin, Ji-Gang Ren, Zhu Chen, Sheng-Long Han, Qing Yu, Ken Liang, Fei Zhou, Xiao Yuan, Mei-Sheng Zhao, Tian-Yin Wang, Xiao Jiang, Liang Zhang, Wei-Yue Liu, Yang Li, Qi Shen, Yuan Cao, Chao-Yang Lu, Rong Shu, Jian-Yu Wang, Li Li, Nai-Le Liu, Feihu Xu, Xiang-Bin Wang, Cheng-Zhi Peng, and Jian-Wei Pan. **An integrated space-to-ground quantum communication network over 4,600 kilometres**. *Nature* 589 (2021), 214–219. DOI: 10.1038/s41586-020-03093-8 (see pages 5, 25, 26).

[Che+20] Jiu-Peng Chen, Chi Zhang, Yang Liu, Cong Jiang, Weijun Zhang, Xiao-Long Hu, Jian-Yu Guan, Zong-Wen Yu, Hai Xu, Jin Lin, Ming-Jun Li, Hao Chen, Hao Li, Lixing You, Zhen Wang, Xiang-Bin Wang, Qiang Zhang, and Jian-Wei Pan. **Sending-or-Not-Sending with Independent Lasers: Secure Twin-Field Quantum Key Distribution over 509 km**. *Physical review letters* 124:7 (2020), 070501. DOI: 10.1103/PhysRevLett.124.070501 (see page 99).

[CK16] Seok-Beom Cho and Heonoh Kim. **Active stabilization of a fiber-optic two-photon interferometer using continuous optical length control**. *Optics express* 24:10 (2016), 10980–10986. DOI: 10.1364/OE.24.010980 (see page 99).

[Chu00] Isaac L. Chuang. **Quantum Algorithm for Distributed Clock Synchronization**. *Physical Review Letters* 85:9 (2000), 2006–2009. ISSN: 0031-9007. DOI: 10.1103/PhysRevLett.85.2006. URL: https://link.aps.org/doi/10.1103/PhysRevLett.85.2006 (see page 5).

[CLW67] J. W. Cooley, P.A.W. Lewis, and P. D. Welch. **Historical notes on the fast Fourier transform**. *Proceedings of the IEEE* 55:10 (1967), 1675–1677. ISSN: 0018-9219. DOI: 10.1109/PROC.1967.5959 (see page 44).

[Cor+13] James C. Corbett, Jeffrey Dean, Michael Epstein, Andrew Fikes, Christopher Frost, J. J. Furman, Sanjay Ghemawat, Andrey Gubarev, Christopher Heiser, Peter Hochschild, Wilson Hsieh, Sebastian Kanthak, Eugene Kogan, Hongyi Li, Alexander Lloyd, Sergey Melnik, David Mwaura, David Nagle, Sean Quinlan, Rajesh Rao, Lindsay Rolig, Yasushi Saito, Michal Szymaniak, Christopher Taylor, Ruth Wang, and Dale Woodford. **Spanner: Google's Globally Distributed Database**. *ACM Trans. Comput. Syst.* 31:3 (2013). ISSN: 0734-2071. DOI: 10.1145/2491245 (see page 5).

[Cos+20] Costantino Agnesi, Marco Avesani, Luca Calderaro, Andrea Stanco, Giulio Foletto, Mujtaba Zahidy, Alessia Scriminich, Francesco Vedovato, Giuseppe Vallone, and Paolo Villoresi. **Simple quantum key distribution with qubit-based synchronization**

and a self-compensating polarization encoder. *Optica* 7:4 (2020), 284–290. DOI: 10.1364/OPTICA.381013 (see pages 6–8, 25, 70, 90, 91, 94).

[Dai+20]   Hui Dai, Qi Shen, Chao-Ze Wang, Shuang-Lin Li, Wei-Yue Liu, Wen-Qi Cai, Sheng-Kai Liao, Ji-Gang Ren, Juan Yin, Yu-Ao Chen, Qiang Zhang, Feihu Xu, Cheng-Zhi Peng, and Jian-Wei Pan. **Towards satellite-based quantum-secure time transfer**. *Nature Physics* 11 (2020), 25. ISSN: 1745-2473. DOI: 10.1038/s41567-020-0892-y (see pages 6, 7, 9, 10, 90, 92, 94, 95).

[Dia+16]   Eleni Diamanti, Hoi-Kwong Lo, Bing Qi, and Zhiliang Yuan. **Practical challenges in quantum key distribution**. *npj Quantum Information* 2:1 (2016), 16025. DOI: 10.1038/npjqi.2016.25 (see page 5).

[Die+16]   Erik F. Dierikx, Anders E. Wallin, Thomas Fordell, Jani Myyry, Petri Koponen, Mikko Merimaa, Tjeerd J. Pinkert, Jeroen C. J. Koelemeij, Henk Z. Peek, and Rob Smets. **White Rabbit Precision Time Protocol on Long-Distance Fiber Links**. *IEEE transactions on ultrasonics, ferroelectrics, and frequency control* 63:7 (2016), 945–952. DOI: 10.1109/TUFFC.2016.2518122 (see pages 5, 25, 73, 74, 90, 91, 94).

[Eck+21]   Sebastian Ecker, Bo Liu, Johannes Handsteiner, Matthias Fink, Dominik Rauch, Fabian Steinlechner, Thomas Scheidl, Anton Zeilinger, and Rupert Ursin. **Strategies for achieving high key rates in satellite-based QKD**. *npj Quantum Information* 7:1 (2021), 5. DOI: 10.1038/s41534-020-00335-5 (see pages 5, 7, 8, 54, 60, 72, 77, 90, 91).

[Eke91]   Artur K. Ekert. **Quantum cryptography based on Bell's theorem**. *Physical review letters* 67:6 (1991), 661–663. DOI: 10.1103/physrevlett.67.661 (see page 5).

[Ele+18]   M. S. Elezov, M. L. Scherbatenko, D. V. Sych, and G. N. Goltsman. **Active and passive phase stabilization for the all-fiber Michelson interferometer**. *Journal of Physics: Conference Series* 1124 (2018), 051014. ISSN: 1742-6588. DOI: 10.1088/1742-6596/1124/5/051014 (see page 85).

[Fit+22]   Erik Fitzke, Lucas Bialowons, Till Dolejsky, Maximilian Tippmann, Oleg Nikiforov, Thomas Walther, Felix Wissel, and Matthias Gunkel. **Scalable Network for Simultaneous Pairwise Quantum Key Distribution via Entanglement-Based Time-Bin Coding**. *PRX Quantum* 3:2 (2022), 020341. DOI: 10.1103/PRXQuantum.3.020341 (see pages 6–9, 90, 91, 94).

[FF+06a]   Anthony Mark Fox, Mark Fox, et al. **Quantum optics: an introduction**. Vol. 15. Oxford university press, 2006 (see page 35).

[FF+06b]   Anthony Mark Fox, Mark Fox, et al. **Quantum optics: an introduction**. Vol. 15. Oxford University Press, 2006 (see page 63).

[Gar+11]   B. García-Lorenzo, A. Eff-Darwich, J. J. Fuensalida, and J. Castro-Almazán. **Adaptive optics parameters connection to wind speed at the Teide Observatory: corrigendum**. *Monthly Notices of the Royal Astronomical Society* 414:2 (2011), 801–809. ISSN: 00358711. DOI: 10.1111/j.1365-2966.2011.17787.x (see page 75).

[Gio+13]   Fabrizio R. Giorgetta, William C. Swann, Laura C. Sinclair, Esther Baumann, Ian Codding-ton, and Nathan R. Newbury. **Optical two-way time and frequency transfer over free space**. *Nature Photonics* 7:6 (2013), 434–438. ISSN: 1749-4885. DOI: 10.1038/nphoton.2013.69 (see pages 13, 74).

[GN11]   Giada Giorgi and Claudio Narduzzi. **Performance Analysis of Kalman-Filter-Based Clock Synchronization in IEEE 1588 Networks**. *IEEE Transactions on Instrumentation and Measurement* 60:8 (2011), 2902–2909. ISSN: 0018-9456. DOI: 10.1109/TIM.2011.2113120 (see pages 16, 69).

[Gio+01]   V. Giovannetti, S. Lloyd, L. Maccone, and F. N. Wong. **Clock synchronization with dispersion cancellation**. *Physical review letters* 87:11 (2001), 117902. DOI: 10.1103/PhysRevLett.87.117902 (see page 5).

[GLM01]   Vittorio Giovannetti, Seth Lloyd, and Lorenzo Maccone. **Quantum-enhanced position-ing and clock synchronization**. *Nature* 412:6845 (2001), 417–419. DOI: 10.1038/35086525 (see pages 6, 95, 96).

[Gis+02]   Nicolas Gisin, Gre´goire Ribordy, Wolfgang Tittel, and Hugo Zbinden. **Quantum cryp-tography**. *Reviews of Modern Physics*: 74(1) (2002), 145(51) (see page 11).

[GT07]   Nicolas Gisin and Rob Thew. **Quantum communication**. *Nature Photonics* 1:3 (2007), 165–171. ISSN: 1749-4885. DOI: 10.1038/nphoton.2007.22 (see page 5).

[Gmb22]   qutools GmbH. **quTAG HR - High Resolution**. Tech. rep. Accessed on December 17, 2022. qutools GmbH, Kistlerhofstraße 70 (Geb. 88), 81379 München, Germany, 2022. URL: https://www.qutools.com/files/quTAG/qutools_quTAG_HR_Datasheet.pdf (see pages 41, 75).

[Gov07]   Govind P. Agrawal. **Nonlinear Fiber Optics**. 4th Edition. Academic Press, 2007. ISBN: 9780123695161 (see page 85).

[Had09]   Robert H. Hadfield. **Single-photon detectors for optical quantum information applications**. *Nature Photonics* 3:12 (2009), 696–705. ISSN: 1749-4885. DOI: 10.1038/nphoton.2009.230 (see page 36).

[Han+07]   Hannes Hübel, Michael R. Vanner, Thomas Lederer, Bibiane Blauensteiner, Thomas Lorünser, Andreas Poppe, and Anton Zeilinger. **High-fidelity transmission of polar-ization encoded qubits from an entangled source over 100 km of fiber**. *Optics Express* 15:12 (2007), 7853–7862. ISSN: 1094-4087. DOI: 10.1364/OE.15.007853 (see page 98).

[Har+20]   Charles R. Harris, K. Jarrod Millman, Stéfan J. van der Walt, Ralf Gommers, Pauli Virtanen, David Cournapeau, Eric Wieser, Julian Taylor, Sebastian Berg, Nathaniel J. Smith, Robert Kern, Matti Picus, Stephan Hoyer, Marten H. van Kerkwijk, Matthew Brett, Allan Haldane, Jaime Fernández del Río, Mark Wiebe, Pearu Peterson, Pierre Gérard-Marchant, Kevin Sheppard, Tyler Reddy, Warren Weckesser, Hameer Abbasi, Christoph Gohlke, and Travis E. Oliphant. **Array programming with NumPy**. *Nature* 585:7825 (Sept. 2020), 357–362. DOI: 10.1038/s41586-020-2649-2. URL: https://doi.org/10.1038/s41586-020-2649-2 (see pages 43, 53).

[He+15]   Jiakun He, Bryn A. Bell, Alvaro Casas-Bedoya, Yanbing Zhang, Alex S. Clark, Chunle Xiong, and Benjamin J. Eggleton. **Ultracompact quantum splitter of degenerate photon pairs**. *Optica* 2:9 (2015), 779. DOI: 10.1364/OPTICA.2.000779 (see page 97).

[HLK09]   Caleb Ho, Antía Lamas-Linares, and Christian Kurtsiefer. **Clock synchronization by remote detection of correlated photon pairs**. *New Journal of Physics* 11:4 (2009), 045011. DOI: 10.1088/1367-2630/11/4/045011 (see pages 6, 8, 25, 43, 46, 47, 49, 53–55, 60, 67, 90, 94).

[Hon+22]   Huibo Hong, Runai Quan, Xiao Xiang, Wenxiang Xue, Honglei Quan, Wenyu Zhao, Yuting Liu, Mingtao Cao, Tao Liu, Shougang Zhang, and Ruifang Dong. **Demonstration of 50 Km Fiber-Optic Two-Way Quantum Clock Synchronization**. *Journal of Lightwave Technology* 40:12 (2022), 3723–3728. ISSN: 0733-8724. DOI: 10.1109/JLT.2022.3153655 (see pages 6, 7, 13, 74, 90–92, 94, 105).

[Hou+19]   Feiyan Hou, Runai Quan, Ruifang Dong, Xiao Xiang, Baihong Li, Tao Liu, Xiaoyan Yang, Hao Li, Lixing You, Zhen Wang, and Shougang Zhang. **Fiber-optic two-way quantum time transfer with frequency-entangled pulses**. *Physical Review A* 100:2 (2019). ISSN: 1050-2947. DOI: 10.1103/PhysRevA.100.023849 (see pages 6, 7, 13, 74, 90–92, 94).

[Inc20]   Stanford Research Systems Inc. **AFS740 GPS Time and Frequency System**. Tech. rep. Accessed on November 20, 2022. 1290-C Reamwood Avenue, Sunnyvale, California 94089, US, 2020. URL: https://www.thinksrs.com/downloads/pdfs/manuals/FS740m.pdf (see page 23).

[Inc14]   Corning Incorporated. **Corning SMF-28 ULL Optical Fiber**. Tech. rep. Accessed on February 28, 2023. Corning Incorporated, One Riverfront Plaza, Corning, NY 14831, USA: Corning Incorporated, 2014. URL: https://www.corning.com/optical-communications/ worldwide/en/home/products/fiber/optical-fiber-products/smf-28-ultra.html? (see page 54).

[Inc22]   Corning Incorporated. **Corning SMF-28 Ultra Optical Fiber**. Tech. rep. Accessed on December 29, 2022. Corning Incorporated, One Riverfront Plaza, Corning, NY 14831, USA, 2022. URL: https://www.corning.com/media/worldwide/coc/documents/Fiber/product- information-sheets/PI-1424-AEN.pdf (see page 85).

[Ins22]   Swabian Instruments. **Time tagger series: Streaming time-to-digital converters**. Tech. rep. Accessed on December 17, 2022. Swabian Instruments, Stammheimer Str. 41, 70435 Stuttgart, Germany, 2022. URL: https://www.swabianinstruments.com/static/ downloads/TimeTaggerSeries.pdf (see pages 41, 75).

[ITU00]   Telecommunication Standardization Sector of ITU. **G.825: The control of jitter and wander within digital networks which are based on the synchronous digital hierarchy (SDH)**. Tech. rep. International Telecommunication Union, Mar. 2000 (see page 31).

[Jen+00]   Thomas Jennewein, Christoph Simon, Gregor Weihs, Harald Weinfurter, and Anton Zeilinger. **Quantum Cryptography with Entangled Photons**. *Physical Review Letters* 84:20 (2000), 4729–4732. ISSN: 0031-9007. DOI: 10.1103/PhysRevLett.84.4729. URL: https://link.aps.org/doi/10.1103/PhysRevLett.84.4729 (see page 62).

[Joh28]   J. B. Johnson. **Thermal Agitation of Electricity in Conductors**. *Phys. Rev.* 32 (1 July 1928), 97–109. DOI: 10.1103/PhysRev.32.97. URL: https://link.aps.org/doi/10.1103/PhysRev.32.97 (see page 20).

[Joz+00]   Richard Jozsa, Daniel S. Abrams, Jonathan P. Dowling, and Colin P. Williams. **Quantum Clock Synchronization Based on Shared Prior Entanglement**. *Physical Review Letters* 85:9 (2000), 2010–2013. ISSN: 0031-9007. DOI: 10.1103/PhysRevLett.85.2010. URL: https://link.aps.org/doi/10.1103/PhysRevLett.85.2010 (see page 5).

[Ker+18]   Erik Kerstel, Arnaud Gardelein, Mathieu Barthelemy, Matthias Fink, Siddarth Koduru Joshi, Rupert Ursin, and The CSUG Team. **Nanobob: a CubeSat mission concept for quantum communication experiments in an uplink configuration**. *EPJ Quantum Technology* 5:1 (2018), 6. DOI: 10.1140/epjqt/s40507-018-0070-7 (see page 5).

[KMH12]   Hayang Kim, Xiaoli Ma, and Benjamin Russell Hamilton. **Tracking Low-Precision Clocks With Time-Varying Drifts Using Kalman Filtering**. *IEEE/ACM Transactions on Networking* 20:1 (2012), 257–270. ISSN: 1063-6692. DOI: 10.1109/TNET.2011.2158656 (see page 16).

[KTO14]   Toshiya Kobayashi, Akihisa Tomita, and Atsushi Okamoto. **Evaluation of the phase randomness of a light source in quantum-key-distribution systems with an attenuated laser**. *Physical Review A* 90:3 (2014), 325. ISSN: 1050-2947. DOI: 10.1103/PhysRevA.90.032320 (see page 27).

[Kon+18]   Xiangyu Kong, Tao Xin, Shi-Jie Wei, Bixue Wang, Yunzhao Wang, Keren Li, and Gui-Lu Long. **Demonstration of multiparty quantum clock synchronization**. *Quantum Information Processing* 17:11 (2018). ISSN: 1570-0755. DOI: 10.1007/s11128-018-2057-9 (see page 6).

[KP02]   Marko Krčo and Prabasaj Paul. **Quantum clock synchronization: Multiparty protocol**. *Physical Review A* 66:2 (2002). ISSN: 1050-2947. DOI: 10.1103/PhysRevA.66.024305 (see page 6).

[LL22]   Randy Lafler and R. Nicholas Lanning. **Quantum time transfer for freespace quantum networking** (Nov. 2022). URL: http://arxiv.org/pdf/2211.00737v1 (see page 92).

[Lee+19]   Jianwei Lee, Lijiong Shen, Alessandro Cerè, James Troupe, Antia Lamas-Linares, and Christian Kurtsiefer. **Symmetrical clock synchronization with time-correlated photon pairs**. *Applied Physics Letters* 114:10 (2019), 101102. ISSN: 0950-0340. DOI: 10.1063/1.5086493 (see pages 6, 7, 70, 90, 91, 94).

[Lee+22] Jianwei Lee, Lijiong Shen, Adrian Nugraha Utama, and Christian Kurtsiefer. **Absolute clock synchronization with a single time-correlated photon pair source over a 10 km optical fibre**. *Optics Express* 30:11 (2022), 18530. ISSN: 1094-4087. DOI: 10.1364/OE. 455542 (see pages 6, 7, 73, 74, 90–92, 94, 105).

[Li+19]   Bin Li, Changyan Sun, Yun Ling, Heng Zhou, and Kun Qiu. **Step-Pulse Modulation of Gain-Switched Semiconductor Pulsed Laser**. *Applied Sciences* 9:3 (2019), 602. DOI: 10.3390/app9030602 (see pages 101, 102).

[Li+22]   Jin Li, Zhong-Hao Zhou, Shuai Wan, Yan-Lei Zhang, Zhen Shen, Ming Li, Chang-Ling Zou, Guang-Can Guo, and Chun-Hua Dong. **All-Optical Synchronization of Remote Optomechanical Systems**. *Phys. Rev. Lett.* 129 (6 Aug. 2022), 063605. DOI: 10.1103/ PhysRevLett.129.063605. URL: https://link.aps.org/doi/10.1103/PhysRevLett.129.063605 (see page 95).

[Li+18]   Xiaolei Li, Lei Deng, Xiaoman Chen, Haiping Song, Yahao Liu, Mengfan Cheng, Songnian Fu, Ming Tang, Minming Zhang, and Deming Liu. **Arbitrary Bias Point Control Technique for Optical IQ Modulator Based on Dither-Correlation Detection**. *Journal of Lightwave Technology* 36:18 (2018), 3824–3836. ISSN: 0733-8724. DOI: 10.1109/ JLT.2018.2851568 (see page 99).

[Lia+17] Sheng-Kai Liao, Wen-Qi Cai, Wei-Yue Liu, Liang Zhang, Yang Li, Ji-Gang Ren, Juan Yin, Qi Shen, Yuan Cao, Zheng-Ping Li, Feng-Zhi Li, Xia-Wei Chen, Li-Hua Sun, Jian-Jun Jia, Jin-Cai Wu, Xiao-Jun Jiang, Jian-Feng Wang, Yong-Mei Huang, Qiang Wang, Yi-Lin Zhou, Lei Deng, Tao Xi, Lu Ma, Tai Hu, Qiang Zhang, Yu-Ao Chen, Nai-Le Liu, Xiang-Bin Wang, Zhen-Cai Zhu, Chao-Yang Lu, Rong Shu, Cheng-Zhi Peng, Jian-Yu Wang, and Jian-Wei Pan. **Satellite-to-ground quantum key distribution**. *Nature* 549:7670 (2017), 43–47. DOI: 10.1038/nature23655 (see pages 5–7, 9, 25, 26, 90, 94).

[Lic21]   Jena Lichtstadt. **Kartenportal der Stadt Jena, base map: GDI-Th dl-de/by-2-0**. Accessed on November 12, 2021. Stadtverwaltung Jena, Postfach 100 338, 07703 Jena, Germany, 2021. URL: https://geoinformation.jena.de/en (see pages 81, 82).

[Liu+21] Yuting Liu, Runai Quan, Xiao Xiang, Huibo Hong, Mingtao Cao, Tao Liu, Ruifang Dong, and Shougang Zhang. **Quantum clock synchronization over 20-km multiple segmented fibers with frequency-correlated photon pairs and HOM interference**. *Applied Physics Letters* 119:14 (2021), 144003. ISSN: 0950-0340. DOI: 10.1063/5.0061478 (see pages 6, 7, 90–92, 94, 95).

[LCQ12]   Hoi-Kwong Lo, Marcos Curty, and Bing Qi. **Measurement-device-independent quantum key distribution**. *Physical review letters* 108:13 (2012), 130503. DOI: 10.1103/ PhysRevLett.108.130503 (see page 13).

[LMC05]   Hoi-Kwong Lo, Xiongfeng Ma, and Kai Chen. **Decoy state quantum key distribution**. *Physical review letters* 94:23 (2005), 230504. DOI: 10.1103/PhysRevLett.94.230504 (see pages 27, 62, 64).

[LP07]   Hoi-Kwong Lo and John Preskill. **Security of Quantum Key Distribution Using Weak Coherent States with Nonrandom Phases**. *Quantum Info. Comput.* 7:5 (July 2007), 431–458. ISSN: 1533-7146 (see page 27).

[Lom03]   Michael A. Lombardi. **Time and Frequency** (2003). Ed. by Robert A. Meyers, 783–801. DOI: https://doi.org/10.1016/B0-12-227410-5/00780-8. URL: https://www.sciencedirect.com/science/article/pii/B0122274105007808 (see page 22).

[Ma+05]   Xiongfeng Ma, Bing Qi, Yi Zhao, and Hoi-Kwong Lo. **Practical decoy state for quantum key distribution**. *Physical Review A* 72:1 (2005). ISSN: 1050-2947. DOI: 10.1103/PhysRevA.72.012326 (see pages 27, 62, 64, 69).

[MLK06]   Ivan Marcikic, Antía Lamas-Linares, and Christian Kurtsiefer. **Free-space quantum key distribution with entangled photons**. *Applied Physics Letters* 89:10 (2006), 101122. ISSN: 0950-0340. DOI: 10.1063/1.2348775 (see page 5).

[Mar+22]   Marco Avesani, Luca Calderaro, Giulio Foletto, Costantino Agnesi, Francesco Picciariello, Francesco B. L. Santagiustina, Alessia Scriminich, Andrea Stanco, Francesco Vedovato, Mujtaba Zahidy, Giuseppe Vallone, and Paolo Villoresi. **QKD field-trial in Padua: a resource-effective implementation with the iPOGNAC encoder**. In: *Quantum Computing, Communication, and Simulation II*. Ed. by Philip R. Hemmer and Alan L. Migdall. Vol. 12015. SPIE, 2022, 120150A. DOI: 10.1117/12.2607215 (see pages 6–8, 90, 91).

[MJW10]   Mark A. Richards, James A. Scheer, and William A. Holm, eds. **Principles of Modern Radar: Basic principles**. Radar, Sonar and Navigation. Institution of Engineering and Technology, 2010. URL: https://digital-library.theiet.org/content/books/ra/sbra021e (see page 96).

[Mar+16]   L. J. Martínez, T. Pelini, V. Waselowski, J. R. Maze, B. Gil, G. Cassabois, and V. Jacques. **Efficient single photon emission from a high-purity hexagonal boron nitride crystal**. *Physical Review B* 94:12 (2016). ISSN: 2469-9950. DOI: 10.1103/PhysRevB.94.121405 (see page 44).

[Mil11]   David L. Mills. **Computer network time synchronization: The Network Time Protocol on Earth and in space**. 2nd ed. Boca Raton FL: CRC Press, 2011. ISBN: 9781439814635 (see pages 5, 11, 65).

[MS90]   Renato E. Mirollo and Steven H. Strogatz. **Synchronization of Pulse-Coupled Biological Oscillators**. *SIAM Journal on Applied Mathematics* 50:6 (1990), 1645–1662. DOI: 10.1137/0150098 (see page 5).

[NH18]   Lakshay Narula and Todd E. Humphreys. **Requirements for Secure Clock Synchronization**. *IEEE Journal of Selected Topics in Signal Processing* 12:4 (2018), 749–762. ISSN: 1932-4553. DOI: 10.1109/JSTSP.2018.2835772 (see pages 5, 95).

[NB14]   T. E. Northup and R. Blatt. **Quantum information transfer using photons**. *Nature Photonics* 8:5 (2014), 356–363. ISSN: 1749-4885. DOI: 10.1038/nphoton.2014.53 (see page 5).

[Oi+17]   Daniel K. L. Oi, Alex Ling, Giuseppe Vallone, Paolo Villoresi, Steve Greenland, Emma Kerr, Malcolm Macdonald, Harald Weinfurter, Hans Kuiper, Edoardo Charbon, and Rupert Ursin. **CubeSat quantum communications mission**. *EPJ Quantum Technology* 4:1 (2017). DOI: 10.1140/epjqt/s40507-017-0060-1 (see page 5).

[PDT22a]   Melis Pahal, Kadir Durak, and Utku Tefek. **Cryptographic security concerns on timestamp sharing via a public channel in quantum-key-distribution systems**. *Phys. Rev. A* 106 (1 July 2022), 012611. DOI: 10.1103/PhysRevA.106.012611. URL: https://link.aps.org/doi/10.1103/PhysRevA.106.012611 (see page 5).

[PDT22b]   Melis Pahal, Kadir Durak, and Utku Tefek. **Cryptographic security concerns on timestamp sharing via a public channel in quantum-key-distribution systems**. *Physical Review A* 106:1 (2022), 012611. ISSN: 1050-2947. DOI: 10.1103/PhysRevA.106.012611. URL: https://link.aps.org/doi/10.1103/PhysRevA.106.012611 (see page 66).

[Pan+98]   Jian-Wei Pan, Dik Bouwmeester, Harald Weinfurter, and Anton Zeilinger. **Experimental Entanglement Swapping: Entangling Photons That Never Interacted**. *Physical Review Letters* 80:18 (1998), 3891–3894. ISSN: 0031-9007. DOI: 10.1103/PhysRevLett.80.3891. URL: https://link.aps.org/doi/10.1103/PhysRevLett.80.3891 (see page 5).

[Pha+94]   A. G. Phadke, B. Pickett, M. Adamiak, M. Begovic, G. Benmouyal, R. O. Burnett, T. W. Cease, J. Goossens, D. J. Hansen, M. Kezunovic, L. L. Mankoff, P. G. McLaren, G. Michel, R. J. Murphy, J. Nordstrom, M. S. Sachdev, H. S. Smith, J. S. Thorp, M. Trotignon, T. C. Wang, and M. A. Xavier. **Synchronized sampling and phasor measurements for relaying and control**. *IEEE Transactions on Power Delivery* 9:1 (1994), 442–452. DOI: 10.1109/61.277716 (see page 5).

[Qua+20]   Runai Quan, Ruifang Dong, Xiao Xiang, Baihong Li, Tao Liu, and Shougang Zhang. **High-precision nonlocal temporal correlation identification of entangled photon pairs for quantum clock synchronization**. *The Review of scientific instruments* 91:12 (2020), 123109. DOI: 10.1063/5.0031166 (see pages 6, 7, 90, 91, 94).

[Qua+19]   Runai Quan, Ruifang Dong, Yiwei Zhai, Feiyan Hou, Xiao Xiang, Hui Zhou, Chaolin Lv, Zhen Wang, Lixing You, Tao Liu, and Shougang Zhang. **Simulation and realization of a second-order quantum-interference-based quantum clock synchronization at the femtosecond level**. *Optics letters* 44:3 (2019), 614–617. DOI: 10.1364/OL.44.000614 (see pages 6, 7, 90–92, 94, 95).

[Qua+22]   Runai Quan, Huibo Hong, Wenxiang Xue, Honglei Quan, Wenyu Zhao, Xiao Xiang, Yuting Liu, Mingtao Cao, Tao Liu, Shougang Zhang, and Ruifang Dong. **Implementation of field two-way quantum synchronization of distant clocks across a 7 km deployed fiber link**. *Optics express* 30:7 (2022), 10269–10279. DOI: 10.1364/OE.451172 (see pages 6, 7, 13, 70, 73, 74, 90–92, 94, 105).

[Qua+16] Runai Quan, Yiwei Zhai, Mengmeng Wang, Feiyan Hou, Shaofeng Wang, Xiao Xiang, Tao Liu, Shougang Zhang, and Ruifang Dong. **Demonstration of quantum synchronization based on second-order quantum coherence of entangled photons**. *Scientific reports* 6 (2016), 30453. DOI: 10.1038/srep30453 (see pages 6, 7, 25, 90–92, 94, 95).

[QUA22] ID QUANTIQUE. **ID281 - Superconducting Nanowire Series**. Tech. rep. Accessed on December 16, 2022. ID QUANTIQUE SA, Rue Eugène-Marziano 25, 1227 Acacias/Geneva, Switzerland, 2022. URL: https://marketing.idquantique.com/acton/attachment/11868/f-023b/1/-/-/-/-/ID281_Brochure.pdf (see pages 22, 75).

[Qua22] Single Quantum. **Superconducting Nanowire Single Photon Detection System**. Tech. rep. Accessed on December 16, 2022. Single Quantum, Rotterdamseweg 394, 2629 HH, Delft, The Netherlands, 2022. URL: https://singlequantum.com/wp-content/uploads/2022/08/Single-Quantum-Brochure-v2-digital.pdf-2.pdf (see pages 22, 36, 42, 75).

[Rap+20] Joshua Rapp, Julian Tachella, Yoann Altmann, Stephen McLaughlin, and Vivek K Goyal. **Advances in Single-Photon Lidar for Autonomous Vehicles: Working Principles, Challenges, and Recent Advances**. *IEEE Signal Processing Magazine* 37:4 (2020), 62–71. DOI: 10.1109/MSP.2020.2983772 (see page 96).

[Ray09] Pierre Raybaut. **Spyder IDE**. Accessed on January 22, 2023. Oct. 2009. URL: https://www.spyder-ide.org/ (see page 53).

[Ren+17] Ji-Gang Ren, Ping Xu, Hai-Lin Yong, Liang Zhang, Sheng-Kai Liao, Juan Yin, Wei-Yue Liu, Wen-Qi Cai, Meng Yang, Li Li, Kui-Xing Yang, Xuan Han, Yong-Qiang Yao, Ji Li, Hai-Yan Wu, Song Wan, Lei Liu, Ding-Quan Liu, Yao-Wu Kuang, Zhi-Ping He, Peng Shang, Cheng Guo, Ru-Hua Zheng, Kai Tian, Zhen-Cai Zhu, Nai-Le Liu, Chao-Yang Lu, Rong Shu, Yu-Ao Chen, Cheng-Zhi Peng, Jian-Yu Wang, and Jian-Wei Pan. **Ground-to-satellite quantum teleportation**. *Nature* 549:7670 (2017), 70–73. DOI: 10.1038/nature23675 (see page 5).

[Riv22] Riverbank Computing. **PyQt**. https://riverbankcomputing.com/software/pyqt/intro. Accessed on December 20, 2022. 2022 (see pages 61, 62).

[RDW21] Pascal Rochat, Fabien Droz, and Qinghua Wang. **Atomic Clocks and Timing Systems in Global Navigation Satellite Systems**. Tech. rep. Accessed on November 20, 2022. Vauseyon 29, Neuchâtel 2000, Switzerland: SpectraTime and T4Science, July 2021. URL: https://www.orolia.com/wp-content/uploads/2021/07/GNSS_Atomic_Clocks-1.pdf (see page 23).

[Sas+11] M. Sasaki, M. Fujiwara, H. Ishizuka, W. Klaus, K. Wakui, M. Takeoka, S. Miki, T. Yamashita, Z. Wang, A. Tanaka, K. Yoshino, Y. Nambu, S. Takahashi, A. Tajima, A. Tomita, T. Domeki, T. Hasegawa, Y. Sakai, H. Kobayashi, T. Asai, K. Shimizu, T. Tokura, T. Tsurumaru, M. Matsui, T. Honjo, K. Tamaki, H. Takesue, Y. Tokura, J. F. Dynes, A. R. Dixon, A. W. Sharpe, Z. L. Yuan, A. J. Shields, S. Uchikoga, M. Legré, S. Robyr, P. Trinkler, L. Monat, J.-B. Page, G. Ribordy, A. Poppe, A. Allacher, O. Maurhart, T. Länger, M. Peev, and A. Zeilinger. **Field test of quantum key distribution in the Tokyo QKD Network**.

Opt. Express 19:11 (May 2011), 10387–10409. DOI: 10.1364/OE.19.010387. URL: http://www.osapublishing.org/oe/abstract.cfm?URI=oe-19-11-10387 (see pages 5, 25, 26).

[SSR18]   J. Savory, J. Sherman, and S. Romisch. **White Rabbit-Based Time Distribution at NIST**. In: *2018 IEEE International Frequency Control Symposium (IFCS)*. IEEE, May 2018, 1–5. ISBN: 978-1-5386-3214-7. DOI: 10.1109/FCS.2018.8597556 (see pages 5, 74, 90, 91, 94).

[Sca+22]   Davide Scalcon, Costantino Agnesi, Marco Avesani, Luca Calderaro, Giulio Foletto, Andrea Stanco, Giuseppe Vallone, and Paolo Villoresi. **Cross-Encoded Quantum Key Distribution Exploiting Time-Bin and Polarization States with Qubit-Based Synchronization**. *Advanced Quantum Technologies* (2022), 2200051 (see page 6).

[STS01]   Richard Schneider, Peter Thuermel, and Michael Stockmann. **Distance measurement of moving objects by frequency modulated laser radar**. *Optical Engineering* 40:1 (2001), 33–37. DOI: 10.1117/1.1332772. URL: https://doi.org/10.1117/1.1332772 (see page 96).

[Sch+15]   S. Schulz, I. Grguraš, C. Behrens, H. Bromberger, J. T. Costello, M. K. Czwalinna, M. Felber, M. C. Hoffmann, M. Ilchen, H. Y. Liu, T. Mazza, M. Meyer, S. Pfeiffer, P. Prędki, S. Schefer, C. Schmidt, U. Wegner, H. Schlarb, and A. L. Cavalieri. **Femtosecond all-optical synchronization of an X-ray free-electron laser**. *Nature communications* 6:1 (2015), 5938. DOI: 10.1038/ncomms6938 (see page 95).

[Sch+21]   Jonas Schwaab, Ronny Meier, Gianluca Mussetti, Sonia Seneviratne, Christine Bürgi, and Edouard L. Davin. **The role of urban trees in reducing land surface temperatures in European cities**. *Nature communications* 12:1 (2021), 6763. DOI: 10.1038/s41467-021-26768-w (see page 82).

[Sep+20]   Brigitta Septriani, Oliver de Vries, Fabian Steinlechner, and Markus Gräfe. **Parametric study of the phase diffusion process in a gain-switched semiconductor laser for randomness assessment in quantum random number generator**. *AIP Advances* 10:5 (2020), 055022. DOI: 10.1063/5.0011418 (see page 27).

[Shi+20]   Yicheng Shi, Soe Moe Thar, Hou Shun Poh, James A. Grieve, Christian Kurtsiefer, and Alexander Ling. **Stable polarization entanglement based quantum key distribution over a deployed metropolitan fiber**. *Applied Physics Letters* 117:12 (2020), 124002. ISSN: 0950-0340. DOI: 10.1063/5.0021755 (see page 5).

[Ste+17]   Fabian Steinlechner, Sebastian Ecker, Matthias Fink, Bo Liu, Jessica Bavaresco, Marcus Huber, Thomas Scheidl, and Rupert Ursin. **Distribution of high-dimensional entanglement via an intra-city free-space link**. *Nature communications* 8 (2017), 15971. DOI: 10.1038/ncomms15971 (see pages 5, 7, 54, 60, 72, 90, 91).

[T H+08]   T. Honjo, S. W. Nam, H. Takesue, Q. Zhang, H. Kamada, Y. Nishida, O. Tadanaga, M. Asobe, B. Baek, R. Hadfield, S. Miki, M. Fujiwara, M. Sasaki, Z. Wang, K. Inoue, and Y. Yamamoto. **Long-distance entanglement-based quantum key distribution over optical fiber**. *Optics Express* 16:23 (2008), 19118–19126. ISSN: 1094-4087. DOI: 10.1364/OE.16.019118 (see page 98).

[Tac+19] Julián Tachella, Yoann Altmann, Nicolas Mellado, Aongus McCarthy, Rachael Tobin, Gerald S. Buller, Jean-Yves Tourneret, and Stephen McLaughlin. **Real-time 3D reconstruction from single-photon lidar data using plug-and-play point cloud denoisers**. *Nature communications* 10:1 (2019), 4984. DOI: 10.1038/s41467-019-12943-7 (see page 96).

[TS10] Hiroki Takesue and Kaoru Shimizu. **Effects of multiple pairs on visibility measurements of entangled photons generated by spontaneous parametric processes**. *Optics Communications* 283:2 (2010), 276–287. ISSN: 00304018. DOI: 10.1016/j.optcom.2009.10.008 (see page 98).

[Tao+13] Tao Wang, Li-Yang Shao, John Canning, and Kevin Cook. **Temperature and strain characterization of regenerated gratings**. *Optics Letters* 38:3 (2013), 247–249. ISSN: 0146-9592. DOI: 10.1364/OL.38.000247 (see page 85).

[Tho+09] Thomas Scheidl, Rupert Ursin, Alessandro Fedrizzi, Sven Ramelow, Xiao-Song Ma, Thomas Herbst, Robert Prevedel, Lothar Ratschbacher, Johannes Kofler, Thomas Jennewein, and Anton Zeilinger. **Feasibility of 300 km quantum key distribution with entangled states**. *New Journal of Physics* 11:8 (2009), 085002. DOI: 10.1088/1367-2630/11/8/085002 (see page 98).

[TA19] Francisco Tirado-Andrés and Alvaro Araujo. **Performance of clock sources and their influence on time synchronization in wireless sensor networks**. *International Journal of Distributed Sensor Networks* 15:9 (2019), 155014771987937. ISSN: 1550-1477. DOI: 10.1177/1550147719879372 (see pages 8, 11, 15, 21).

[Tob+21] Rachael Tobin, Abderrahim Halimi, Aongus McCarthy, Philip J. Soan, and Gerald S. Buller. **Robust real-time 3D imaging of moving scenes through atmospheric obscurant using single-photon LiDAR**. *Scientific reports* 11:1 (2021), 11236. DOI: 10.1038/s41598-021-90587-8 (see page 96).

[Tol+15] P. Toliver, J. M. Dailey, A. Agarwal, and N. A. Peters. **Continuously active interferometer stabilization and control for time-bin entanglement distribution**. *Optics express* 23:4 (2015), 4135–4143. DOI: 10.1364/OE.23.004135 (see page 99).

[Tom+10] Akihisa Tomita, Ken-ichiro Yoshino, Yoshihiro Nambu, Akio Tajima, Akihiro Tanaka, Seigo Takahashi, Wakako Maeda, Shigehito Miki, Zhen Wang, Mikio Fujiwara, and Masahide Sasaki. **High speed quantum key distribution system**. *Optical Fiber Technology* 16:1 (2010), 55–62. ISSN: 10685200. DOI: 10.1016/j.yofte.2009.10.003 (see page 5).

[TJM82] Toshimitsu Musha, Jun-ichi Kamimura, and Masataka Nakazawa. **Optical phase fluctuations thermally induced in a single-mode optical fiber**. *Appl. Opt.* 21:4 (1982), 694–698. DOI: 10.1364/AO.21.000694 (see page 99).

[Tro+22] James Troupe, Stav Haldar, Ivan Agullo, and Paul Kwiat. **Quantum Clock Synchronization for Future NASA Deep Space Quantum Links and Fundamental Science**. *arXiv:2209.15122* (2022) (see page 10).

[Tsu+18] Yoshiaki Tsujimoto, Motoki Tanaka, Nobuo Iwasaki, Rikizo Ikuta, Shigehito Miki, Taro Yamashita, Hirotaka Terai, Takashi Yamamoto, Masato Koashi, and Nobuyuki Imoto. **High-fidelity entanglement swapping and generation of three-qubit GHZ state using asynchronous telecom photon pair sources**. *Scientific reports* 8:1 (2018), 1446. DOI: 10.1038/s41598-018-19738-8 (see page 5).

[Urs+07] R. Ursin, F. Tiefenbacher, T. Schmitt-Manderbach, H. Weier, T. Scheidl, M. Lindenthal, B. Blauensteiner, T. Jennewein, J. Perdigues, P. Trojek, B. Ömer, M. Fürst, M. Meyenburg, J. Rarity, Z. Sodnik, C. Barbieri, H. Weinfurter, and A. Zeilinger. **Entanglement-based quantum communication over 144 km**. *Nature Physics* 3:7 (2007), 481–486. ISSN: 1745-2473. DOI: 10.1038/nphys629 (see pages 5, 7, 90, 91).

[VAD04] Vadim Makarov, Alexei Brylevski, and Dag R. Hjelme. **Real-time phase tracking in single-photon interferometers**. *Appl. Opt.* 43:22 (2004), 4385–4392. DOI: 10.1364/AO.43.004385 (see page 99).

[VSS04] Alejandra Valencia, Giuliano Scarcelli, and Yanhua Shih. **Distant clock synchronization using entangled photon pairs**. *Applied Physics Letters* 85:13 (2004), 2655–2657. ISSN: 0950-0340. DOI: 10.1063/1.1797561 (see pages 6–8, 25, 90, 91, 94).

[Val+16] Raju Valivarthi, Marcel.li Grimau Puigibert, Qiang Zhou, Gabriel H. Aguilar, Varun B. Verma, Francesco Marsili, Matthew D. Shaw, Sae Woo Nam, Daniel Oblak, and Wolfgang Tittel. **Quantum teleportation across a metropolitan fibre network**. *Nature Photonics* 10:10 (2016), 676–680. ISSN: 1749-4885. DOI: 10.1038/nphoton.2016.180 (see page 5).

[van+99] J.-J. van de Beek, P. O. Borjesson, M.-L. Boucheret, D. Landstrom, J. M. Arenas, P. Odling, C. Ostberg, M. Wahlqvist, and S. K. Wilson. **A time and frequency synchronization scheme for multiuser OFDM**. *IEEE Journal on Selected Areas in Communications* 17:11 (1999), 1900–1914. ISSN: 07338716. DOI: 10.1109/49.806820 (see page 5).

[van+95] J.-J. van de Beek, M. Sandell, M. Isaksson, and P. Ola Borjesson. **Low-complex frame synchronization in OFDM systems**. In: *Proceedings of ICUPC '95 - 4th IEEE International Conference on Universal Personal Communications*. IEEE, Nov. 1995, 982–986. ISBN: 0-7803-2955-4. DOI: 10.1109/ICUPC.1995.497156 (see page 5).

[VBP04] Darryl Veitch, Satish Babu, and Attila Pasztor. **Robust Synchronization of Software Clocks Across the Internet**. *IMC '04: Proceedings of the 4th ACM SIGCOMM conference on Internet measurement* (Oct. 2004), 219–232 (see page 16).

[Vig08] J.R. Vig. **Quartz Crystal Resonators and Oscillators for Frequency Control and Timing Applications: A Tutorial (Rev. 8.5.3.9)**. Tech. rep. Accessed on November 18, 2022. US Army Communications-Electronics Research, Development and Engineering Center Fort Monmouth, NJ, USA, Nov. 2008 (see pages 20, 21, 23).

[Wah+20] Michael Wahl, Tino Röhlicke, Sebastian Kulisch, Sumeet Rohilla, Benedikt Krämer, and Andreas C. Hocke. **Photon arrival time tagging with many channels, sub-nanosecond deadtime, very high throughput, and fiber optic remote synchronization**. *The Review of scientific instruments* 91:1 (2020), 013108. DOI: 10.1063/1.5121412 (see page 5).

[Wal18] Walter Schottky. **On spontaneous current fluctuations in various electrical conductors**. *Journal of Micro/Nanolithography, MEMS, and MOEMS* 17:4 (2018), 041001. DOI: 10.1117/1.JMM.17.4.041001 (see page 20).

[Wan+21a] Chao-Ze Wang, Yang Li, Wen-Qi Cai, Wei-Yue Liu, Sheng-Kai Liao, and Cheng-Zhi Peng. **Synchronization using quantum photons for satellite-to-ground quantum key distribution**. *Optics express* 29:19 (2021), 29595–29603. DOI: 10.1364/OE.433631 (see pages 6–9, 25, 48, 58, 70, 90, 94).

[Wan+21b] Chaoze Wang, Yang Li, Wenqi Cai, Meng Yang, Weiyue Liu, Shengkai Liao, and Chengzhi Peng. **Robust aperiodic synchronous scheme for satellite-to-ground quantum key distribution**. *Appl. Opt.* 60:16 (June 2021), 4787–4792. DOI: 10.1364/AO.425085. URL: http://www.osapublishing.org/ao/abstract.cfm?URI=ao-60-16-4787 (see pages 5, 25, 26, 90, 99).

[Wan+20] Dong Wang, Xiaotian Song, Liangjiang Zhou, and Yibo Zhao. **Real-Time Phase Tracking Scheme With Mismatched-Basis Data for Phase-Coding Quantum Key Distribution**. *IEEE Photonics Journal* 12:3 (2020), 1–7. DOI: 10.1109/JPHOT.2020.2986343 (see page 99).

[Wan+14] Shuang Wang, Wei Chen, Zhen-Qiang Yin, Hong-Wei Li, De-Yong He, Yu-Hu Li, Zheng Zhou, Xiao-Tian Song, Fang-Yi Li, Dong Wang, Hua Chen, Yun-Guang Han, Jing-Zheng Huang, Jun-Fu Guo, Peng-Lei Hao, Mo Li, Chun-Mei Zhang, Dong Liu, Wen-Ye Liang, Chun-Hua Miao, Ping Wu, Guang-Can Guo, and Zheng-Fu Han. **Field and long-term demonstration of a wide area quantum key distribution network**. *Opt. Express* 22:18 (Sept. 2014), 21739–21756. DOI: 10.1364/OE.22.021739. URL: http://www.osapublishing.org/oe/abstract.cfm?URI=oe-22-18-21739 (see pages 5, 25, 26).

[Wan+22] Yazhou Wang, Zhengran Li, Fei Yu, Meng Wang, Ying Han, Lili Hu, and Jonathan Knight. **Temperature-Dependent Group Delay of Photonic-Bandgap Hollow-Core Fiber Tuned by Surface-Mode Coupling**. *Optics Express* 30:1 (2022), 222. ISSN: 1094-4087. DOI: 10.1364/OE.443075 (see page 85).

[Wen+20] Sören Wengerowsky, Siddarth Koduru Joshi, Fabian Steinlechner, Julien R. Zichi, Bo Liu, Thomas Scheidl, Sergiy M. Dobrovolskiy, René van der Molen, Johannes W. N. Los, Val Zwiller, Marijn A. M. Versteegh, Alberto Mura, Davide Calonico, Massimo Inguscio, Anton Zeilinger, André Xuereb, and Rupert Ursin. **Passively stable distribution of polarisation entanglement over 192 km of deployed optical fibre**. *npj Quantum Information* 6:1 (2020), 012307. DOI: 10.1038/s41534-019-0238-8 (see page 5).

[WD08]   William Riley and David Howe. **Handbook of Frequency Stability Analysis**. Special Publication (NIST SP), National Institute of Standards and Technology, Gaithersburg, MD, 2008. URL: https://tsapps.nist.gov/publication/get_pdf.cfm?pub_id=50505 (see pages 15, 18, 19, 73, 74).

[Wil+04]   William Stone, Maris Juberts, Nicholas Dagalakis, Jack Stone Jr., and Jason Gorman. **Performance Analysis of Next-Generation LADAR for Manufacturing, Construction, and Mobility** (2004). DOI: 10.6028/NIST.IR.7117. URL: https://tsapps.nist.gov/publication/get_pdf.cfm?pub_id=822493 (see page 96).

[Wil+21]   James Williams, Martin Suchara, Tian Zhong, Hong Qiao, Rajkumar Kettimuthu, and Riku Fukumori. **Implementation of quantum key distribution and quantum clock synchronization via time bin encoding**. In: *Quantum Computing, Communication, and Simulation*. Ed. by Philip R. Hemmer and Alan L. Migdall. SPIE, 2021, 5. ISBN: 9781510642331. DOI: 10.1117/12.2581862. URL: https://www.spiedigitallibrary.org/conference-proceedings-of-spie/11699/2581862/Implementation-of-quantum-key-distribution-and-quantum-clock-synchronization-via/10.1117/12.2581862.full (see pages 6, 7, 90, 91, 94, 105).

[Wu+19]   Shuhe Wu, Wenfeng Huang, Peiyu Yang, Shuqi Liu, and Liqing Chen. **Arbitrary phase-locking in Mach–Zehnder interferometer**. *Optics Communications* 442 (2019), 148–151. ISSN: 00304018. DOI: 10.1016/j.optcom.2019.03.031 (see page 100).

[Xia+22]   Xiao Xiang, Bingke Shi, Runai Quan, Yuting Liu, Zhiguang Xia, Huibo Hong, Tao Liu, Jincai Wu, Jia Qiang, Jianjun Jia, Shougang Zhang, and Ruifang Dong. **Quantum two-way time transfer over a hybrid free-space and fiber link** (Dec. 2022). DOI: 10.48550/ARXIV.2212.01741 (see pages 13, 74, 92).

[Xie+21]   Mengyu Xie, Haoran Zhang, Zaisheng Lin, and Gui-Lu Long. **Implementation of a twin-beam state-based clock synchronization system with dispersion-free HOM feedback**. *Optics express* 29:18 (2021), 28607–28618. DOI: 10.1364/OE.434386 (see pages 6, 90, 92, 94, 95).

[Yin+20]   Juan Yin, Yu-Huai Li, Sheng-Kai Liao, Meng Yang, Yuan Cao, Liang Zhang, Ji-Gang Ren, Wen-Qi Cai, Wei-Yue Liu, Shuang-Lin Li, Rong Shu, Yong-Mei Huang, Lei Deng, Li Li, Qiang Zhang, Nai-Le Liu, Yu-Ao Chen, Chao-Yang Lu, Xiang-Bin Wang, Feihu Xu, Jian-Yu Wang, Cheng-Zhi Peng, Artur K. Ekert, and Jian-Wei Pan. **Entanglement-based secure quantum cryptography over 1,120 kilometres**. *Nature* 582:7813 (2020), 501–505. DOI: 10.1038/s41586-020-2401-y (see pages 5, 25, 26).

[Yoo+18]   Han Woong Yoo, Norbert Druml, David Brunner, Christian Schwarzl, Thomas Thurner, Marcus Hennecke, and Georg Schitter. **MEMS-based lidar for autonomous driving**. *e & i Elektrotechnik und Informationstechnik* 135:6 (2018), 408–415. ISSN: 1613-7620. DOI: 10.1007/s00502-018-0635-2 (see page 96).

[Zha+20]   Jie Zhao, Chaoxuan Ma, Michael Rüsing, and Shayan Mookherjea. **High Quality Entangled Photon Pair Generation in Periodically Poled Thin-Film Lithium Niobate Waveguides**. *Physical review letters* 124:16 (2020), 163603. DOI: 10.1103/PhysRevLett.124. 163603 (see page 97).

[Zho+15]   Tian Zhong, Hongchao Zhou, Robert D. Horansky, Catherine Lee, Varun B. Verma, Adriana E. Lita, Alessandro Restelli, Joshua C. Bienfang, Richard P. Mirin, Thomas Gerrits, Sae Woo Nam, Francesco Marsili, Matthew D. Shaw, Zheshen Zhang, Ligong Wang, Dirk Englund, Gregory W. Wornell, Jeffrey H. Shapiro, and Franco N. C. Wong. **Photon-efficient quantum key distribution using time–energy entanglement with high-dimensional encoding**. *New Journal of Physics* 17:2 (2015), 022002. DOI: 10.1088/1367-2630/17/2/022002 (see page 43).

[ZT05]   Cristina Zucca and Patrizia Tavella. **The clock model and its relationship with the Allan and related variances**. *IEEE transactions on ultrasonics, ferroelectrics, and frequency control* 52:2 (2005), 289–296. DOI: 10.1109/tuffc.2005.1406554 (see page 19).

Complete list of publications

Relevant articles in refereed conference proceedings

[1] Christopher Spiess, Luis Javier González Martin Del Campo, Nicolas Eduardo Tangar-ife Villamizar, and Fabian Steinlechner. **Stabilization of fiber-based interferometer with single photons**. In: *CLEO 2023*. Optica Publishing Group, 2023, FM1A.7. DOI: 10.1364/CLEO_FS.2023.FM1A.7. URL: https://opg.optica.org/abstract.cfm?URI=CLEO_FS-2023-FM1A.7.

[2] Christopher Spiess and Fabian Steinlechner. **Clock synchronization methods with single photon sources**. In: *Quantum 2.0 Conference and Exhibition*. Optica Publishing Group, 2022, QTu3B.2. DOI: 10.1364/QUANTUM.2022.QTu3B.2. URL: https://opg.optica.org/abstract.cfm?URI=QUANTUM-2022-QTu3B.2.

[3] Christopher Spiess, Sebastian Töpfer, Daniel Rieländer, and Fabian Steinlechner. **One-way clock synchronization with single photons**. In: *Conference on Lasers and Electro-Optics*. Optica Publishing Group, 2022, AW5P.4. DOI: 10.1364/CLEO_AT.2022.AW5P.4. URL: https://opg.optica.org/abstract.cfm?URI=CLEO_AT-2022-AW5P.4.

[4] Christopher Spiess, Sebastian Töpfer, Andrej Krzic Sakshi Sharma, Thomas Grafe-nauer, Roland Lieger, Bernhard Ömer, Stefan Petscharnig, Michael Warum, Christoph Pacher, Gregor Sauer, Matthias Goy, Rene Berlich, Teresa Kopf, Thomas Peschel, Christoph Damm, Aoife Brady, Daniel Rieländer, and Fabian Steinlechner. **Qunet: Mobile Free-Space Quantum Communication System**. In: *QCrypt*. QCrypt, 2021, Poster Session 2. URL: https://2021.qcrypt.net/posters/QCrypt2021Poster211Spiess.pdf.

[5] Christopher Spiess, Sebastian Töpfer, Sakshi Sharma, Andrej Krzic, Gregor Sauer, Daniel Rieländer, and Fabian Steinlechner. **Synchronization of quantum communication systems based on correlated photons**. In: *Conference on Lasers and Electro-Optics*. Optica Publishing Group, 2021, ATu1S.3. DOI: 10.1364/CLEO_AT.2021.ATu1S.3. URL: https://opg.optica.org/abstract.cfm?URI=CLEO_AT-2021-ATu1S.3.

Relevant articles in refereed journals

[6] Christopher Spiess and Fabian Steinlechner. **Clock synchronization with pulsed single photon sources**. *Quantum Science and Technology* 9:1 (Dec. 2023), 015019. DOI: 10.1088/2058-9565/ad0ce0. URL: https://dx.doi.org/10.1088/2058-9565/ad0ce0.

[7] Christopher Spiess, Sebastian Töpfer, Sakshi Sharma, Andrej Kr ži č, Meritxell Cabrejo-Ponce, Uday Chandrashekara, Nico Lennart Döll, Daniel Rieländer, and Fabian Steinlechner. **Clock Synchronization with Correlated Photons**. *Phys. Rev. Appl.* 19 (5 May 2023), 054082. DOI: 10.1103/PhysRevApplied.19.054082. URL: https://link.aps.org/doi/10.1103/PhysRevApplied.19.054082.

Scientific talks

[8] Christopher Spiess. **Poster: Robust Time Transfer with Single Photons on Hybrid Quantum Communication Scenarios in Fiber and Free-Space**. In: *Conference on Lasers and Electro-Optics*. Optica Publishing Group, June 2023.

[9] Christopher Spiess. **Talk: Clock synchronization methods with single photon sources**. In: *Quantum 2.0 Conference and Exhibition*. Optica Publishing Group, June 2022, QTu3B.2.

[10] Christopher Spiess. **Talk: Clock synchronization with single photon sources**. In: Fraunhofer Quantum Doc Forum, July 2022.

[11] Christopher Spiess. **Talk: Highly integrated faint pulse source for polarization encoded quantum communication**. In: ScyLight Workshop on Optical and Quantum Communication, June 2022.

[12] Christopher Spiess. **Talk: One-way clock synchronization with single photons**. In: *Conference on Lasers and Electro-Optics*. Optica Publishing Group, May 2022, AW5P.4.

[13] Christopher Spiess. **Talk: Stabilization of fiber-based interferometer with single photons**. In: *CLEO 2023*. Optica Publishing Group, May 2023, FM1A.7.

[14] Christopher Spiess. **Talk: Synchronization of quantum communication systems based on correlated photons**. In: *Conference on Lasers and Electro-Optics*. Optica Publishing Group, 2021, ATu1S.3.

Further articles in refereed conference proceedings or journals

[15] Meritxell Cabrejo, André Luis Marques Muniz, Philippe Ancsin, Christopher Spiess, and Fabian Steinlechner. **Fiber-based Sagnac interferometer for active polarization entangled photon-pair source**. In: *Quantum Computing, Communication, and Simulation II*. Ed. by Philip R. Hemmer and Alan L. Migdall. Vol. 12015. International Society for Optics and Photonics. SPIE, 2022, 120150C. DOI: 10.1117/12.2609030. URL: https://doi.org/10.1117/12.2609030.

[16] Meritxell Cabrejo-Ponce, Christopher Spiess, André Luiz Marques Muniz, Philippe Ancsin, and Fabian Steinlechner. **GHz-pulsed source of entangled photons for reconfigurable quantum networks**. *Quantum Science and Technology* 7:4 (Aug. 2022), 045022. DOI: 10.1088/2058-9565/ac86f0. URL: https://dx.doi.org/10.1088/2058-9565/ac86f0.

[17] Xue Dong, Christopher Spiess, Victor G. Bucklew, and William H. Renninger. **Chirped-pulsed Kerr solitons in the Lugiato-Lefever equation with spectral filtering**. *Phys. Rev. Research* 3 (3 Sept. 2021), 033252. DOI: 10.1103/PhysRevResearch.3.033252. URL: https://link.aps.org/doi/10.1103/PhysRevResearch.3.033252.

[18] Xue Dong, Qian Yang, Christopher Spiess, Victor G. Bucklew, and William H. Renninger. **Stretched-Pulse Soliton Kerr Resonators**. *Phys. Rev. Lett.* 125 (3 July 2020), 033902. DOI: 10.1103/PhysRevLett.125.033902. URL: https://link.aps.org/doi/10.1103/PhysRevLett.125.033902.

[19] Andrej Kržič, Nico Döll, Uday Chandrashekara, Christopher Spiess, and Fabian Steinlechner. **Adjustable spatial filter for optimal free-space quantum communication round the clock**. *Opt. Express* 31:20 (Sept. 2023), 32362–32372. DOI: 10.1364/OE.489022. URL: https://opg.optica.org/oe/abstract.cfm?URI=oe-31-20-32362.

[20] Andrej Kržič, Sakshi Sharma, Christopher Spiess, Uday Chandrashekara, Sebastian Töpfer, Gregor Sauer, González-Martín del Campo, Luis Javier, Teresa Kopf, Stefan Petscharnig, Thomas Grafenauer, Roland Lieger, Bernhard Ömer, Christoph Pacher, René Berlich, Thomas Peschel, Christoph Damm, Stefan Risse, Matthias Goy, Daniel Rieländer, Andreas Tünnermann, and Fabian Steinlechner. **Towards metropolitan free-space quantum networks**. *npj Quantum Information* 9:1 (2023), 95. DOI: 10.1038/s41534-023-00754-0.

[21] William Renninger, Xue Dong, Christopher Spiess, Victor Bucklew, and Zhiqiang Wang. **Ultrashort pulse generation from stretched-pulse and chirped-pulse fiber Kerr resonators**. In: *Ultrafast Nonlinear Imaging and Spectroscopy IX*. Ed. by Zhiwen Liu, Demetri Psaltis, and Kebin Shi. Vol. 11825. International Society for

Optics and Photonics. SPIE, 2021, 118250S. DOI: 10.1117/12.2595519. URL: https://doi.org/10.1117/12.2595519.

[22] William Renninger, Christopher Spiess, Xue Dong, Qian Yang, and Victor G. Bucklew. **Femtosecond pulse generation from fiber Kerr resonators**. In: *Ultrafast Nonlinear Imaging and Spectroscopy VIII*. Ed. by Zhiwen Liu, Demetri Psaltis, and Kebin Shi. Vol. 11497. International Society for Optics and Photonics. SPIE, 2020, 114970D. DOI: 10.1117/12.2567446. URL: https://doi.org/10.1117/12.2567446.

[23] Christopher Spiess, Qian Yang, Victor G. Bucklew, and William H. Renninger. **Highly-Chirped Solitons in Driven Resonators**. In: *2019 Conference on Lasers and Electro-Optics (CLEO)*. 2019, 1–2. DOI: 10.1364/CLEO_SI.2019.SF1L.4.

[24] Christopher Spiess, Qian Yang, Xue Dong, Victor G. Bucklew, and William H. Renninger. **Chirped dissipative solitons in driven optical resonators**. *Optica* 8:6 (June 2021), 861–869. DOI: 10.1364/OPTICA.419771. URL: https://opg.optica.org/optica/abstract.cfm?URI=optica-8-6-861.

[25] Qian Yang, Christopher Spiess, Victor G. Bucklew, and William H. Renninger. **Stretched-Pulse Solitons in Driven Fiber Resonators**. In: *Conference on Lasers and Electro-Optics*. Optica Publishing Group, 2019, SF1L.3. DOI: 10.1364/CLEO_SI.2019.SF1L.3. URL: https://opg.optica.org/abstract.cfm?URI=CLEO_SI-2019-SF1L.3.

Ehrenwörtliche Erklärung

Ich erkläre hiermit ehrenwörtlich, dass ich die vorliegende Arbeit selbständig, ohne unzulässige Hilfe Dritter und ohne Benutzung anderer als der angegebenen Hilfsmittel und Literatur angefertigt habe. Die aus anderen Quellen direkt oder indirekt übernommenen Daten und Konzepte sind unter Angabe der Quelle gekennzeichnet. Bei der Auswahl und Auswertung folgenden Materials haben mir die nachstehend aufgeführten Personen in der jeweils beschriebenen Weise entgeltlich/unentgeltlich geholfen:

1. Andrej Kržič und Nico Lennart Döll für den Aufbau und die Ausrichtung der 1,7 km langen optischen Freistrahlverbindung und die Einrichtung der Messungen der atmosphärischen Turbulenz.

2. Uday Chandrashekara and Sakshi Sharma für das zur Verfügungstellen der korrelierten Photonenpaarquelle.

3. Sebastian Töpfer im Zuge der Freistrahl-Linkexperimente für die Bereitstellung einer grafischen Benutzeroberfläche, die Erzeugung von Datenpaketen für die Timestamps und deren Übertragung über eine Antenne.

4. Andrej Kržič, Meritxell Cabrejo Ponce, Karin Burger, Fabian Steinlechner, Carlos Andres Sevilla Gutierrez, Gregor Sauer, René Sondenheimer und Andreas Tünnermann für das interne Peer-Review und Feedback über die Promotionsarbeit.

5. ChatGPT mit der sprachlichen Verbesserung von ein paar wenigen Textbausteinen.

6. Martin S. Krejca von dem Hasso-Plattner Institute für die Entwicklung und Zurverfügungstellung dieses wunderschönen Latex-Templates.

Weitere Personen waren an der inhaltlich-materiellen Erstellung der vorliegenden Arbeit nicht beteiligt. Insbesondere habe ich hierfür nicht die entgeltliche Hilfe von Vermittlungsbzw. Beratungsdiensten (Promotionsberater oder andere Personen) in Anspruch genommen. Niemand hat von mir unmittelbar oder mittelbar geldwerte Leistungen für Arbeiten erhalten, die im Zusammenhang mit dem Inhalt der vorgelegten Dissertation stehen. Die Arbeit wurde bisher weder im In- noch im Ausland in gleicher oder ähnlicher Form einer anderen Prüfungsbehörde vorgelegt. Die geltende Promotionsordnung der Physikalisch-Astronomischen Fakultät ist mir bekannt. Ich versichere ehrenwörtlich, dass ich nach bestem Wissen die reine Wahrheit gesagt und nichts verschwiegen habe.

Jena, 18. Oktober 2023

Ort, Datum   Unterschrift des Verfassers

Declaration of authorship

I solemnly declare that I have independently prepared and completed the presented work without undue assistance from third parties or the use of references not cited in literature. Data and ideas which were included directly or indirectly from other sources are cited by referencing the original source. The following individuals have supported me (paid/unpaid) with the selection and analysis of the presented work in the stated way,

1. Andrej Kržič and Nico Lennart Döll for the setup and alignment of the 1.7 km free-space link and setting up the measurements of the atmospheric turbulence.

2. Uday Chandrashekara and Sakshi Sharma for providing the correlated photon pair source.

3. Sebastian Töpfer for providing a graphical user interface for the measurements, the data package generation for time tags and its transfer over the free-space link.

4. Andrej Kržič, Meritxell Cabrejo-Ponce, Karin Burger, Fabian Steinlechner, Carlos Andres Sevilla Gutierrez, Gregor Sauer, René Sondenheimer and Andreas Tünnermann for the internal peer-review and feedback to improve the thesis.

5. ChatGPT by improving the language of very few text blocks.

6. Martin S. Krejca from the Hasso-Plattner Institute for providing this beautiful Latex thesis template.

No further individuals were involved in the preparation of the presented thesis with respect to content and materials. In particular, I did not receive paid assistance or consulting services from PhD consultant or others. Nobody has received direct or indirect monetary benefits for work associated with the content of this submitted thesis. This work has to date not been submitted domestically or abroad in the current or in a similar version to any other examination board. I am aware of the applicable regulations for Doctoral Studies of the Faculty of Physics and Astronomy. I declare on my honor that I have told the truth to the best of my knowledge and have not concealed anything.

Jena, 18. October 2023

Place, Date   Signature